Modelling the atmospheric mineral dust cycle using a dynamic global vegetation model

Sarah R. Shannon

A dissertation submitted to the University of Bristol in accordance with the requirements for award of degree of Doctor of Philosophy in the Faculty of Geographical Sciences

September 2009

Word count 45,344

Abstract

Mineral dust interacts with the climate by modifying the Earth's radiation budget and by transporting nutrients to the terrestrial and marine ecosystems. To estimate how the atmospheric dust loading will change in the future it is important to understand the processes that control the quantity of dust in the atmosphere. Current dust cycle models are unable to predict changes in the extent of arid and semi-arid regions caused by the transient response of vegetation cover to the climate. As a consequence, it is not possible to predict the expansion and contraction of these regions on seasonal and inter-annual time scales.

A new dust cycle model is developed which uses the Lund-Potsdam-Jena dynamic global vegetation model to calculate time evolving dust sources. Surface emissions are calculated by simulating the processes of saltation and sandblasting. Dust is transported in the atmosphere by advection, convection and diffusion and removed from the atmosphere by dry deposition and sub-cloud scavenging. To improve the performance of the model, threshold values for vegetation cover, soil moisture, snow depth and threshold friction velocity, used to determine surface emissions are tuned. The effectiveness of three sub-cloud scavenging schemes are also tested. The tuning experiments are evaluated against multiple measurement datasets.

The ability of the new model to predict seasonality in the dust cycle is evaluated. The model is successful at predicting the seasonality in dust emissions from North Africa, South Africa, Patagonia, North America, and Asia but not in Australia where LPJ is unable to predict the vegetation dynamics correctly. In all regions maximum emissions occur when low precipitation combines with a high frequency of wind speed events greater than $2ms^{-1}$. In Patagonia, surface emissions are strongly anti-correlated with precipitation because wind speeds exceed $2ms^{-1}$ continuously throughout the year. Vegetation cover constrains emissions in North America, Central Asia, Eastern China and South Africa.

The new model has been used to investigate whether changes in vegetation cover in the Sahel can explain the four-fold increase in dust concentrations measured at Barbados during the 1980s relative to the 1960s. Results showed there was an expansion of the Sahara in 1984 relative to 1966 resulting in a doubling of emissions from the Sahel. This alone is not enough to account for the high dust concentrations in 1984. This finding adds strength to the hypothesis that human induced soil degradation in North Africa may be responsible for the increase in high dust concentrations at Barbados during the 1980s

relative to the 1960s. To predict how dust source areas will change in the future it is important to disentangle processes which cause natural variability from anthropogenic effects.

Acknowledgments

I would like to thank my supervisors Dan Lunt and Sandy Harrison for their continued support over the course of the PhD. Thank you to Dan for the all meetings which helped with the scientific and technical aspects of the PhD as well as providing encouragement and motivation. Thank you to Sandy Harrison for her contribution to original idea for the project and her involvement with the GREENCYCLES-RTN which provided the funding for this work. I also wish to thank the people I met in the GREENCYCLES network who made the GREENCYLES meetings and the ERCA summer school very memorable. I would like to also extend thanks to my fellow postgraduate students in Browns for the tea breaks and social events over the last four years which made Browns a great environment to work in.

Finally, thanks to James Wilkinson for all his support, especially over the last year. Thank you for all your help, using the compute cluster and for listening to me talking about dust.

Authors' Declaration

I declare that the work in this dissertation was carried out in accordance with the requirements of the University's Regulations and Code of Practice for Research Degree Programmes and that it has not been submitted for any other academic award. Except where indicated by specific reference in the text, the work is the candidate's own work. Work done in collaboration with, or with the assistance of, others, is indicated as such. Any views expressed in the dissertation are those of the author.

SIGNED: ..... DATE:…….....

1 Introduction

Changes in the extent of arid and semi-arid regions will have a significant impact of the quantity of mineral dust in the atmosphere. The expansion and contraction of these regions is largely controlled by changes in vegetation cover. Because of this, it is important to understand how vegetation cover at the boundaries of these regions will respond to the climate. Understanding this process will help to explain trends in dust concentrations in the past decades and provide insight into how desert regions will change in the future under elevated CO_2.

This introduction describes the dust cycle and the various ways in which mineral dust interacts with the Earth's system. This is followed by a summary of observational studies which show that there is seasonal and inter-annual variability in the dust cycle. Recent developments in dust cycle modelling are discussed and the need for a new dust cycle model is highlighted. Finally, the thesis plan and the specific aims of this work are presented.

1.1 The dust cycle

The movement of dust in the atmosphere has three phases; dust emission, transport and removal. Dust emission occurs when dry sparsely vegetated soil is exposed to the surface on which an abundance of particles are available for entrainment. These particles are formed by glacial grinding, frost weathering, aeolian abrasion by saltating particles, chemical weathering of rocks and abrasion in rivers and lakes (Pye 1987).

Particles with diameter in the range of 60-2000μm are mobilised by saltation (Marticorena and Bergametti 1995). Saltation occurs when wind speeds are strong enough to overcome the forces of gravity and inter-particle cohesion. The particles are lifted just above the surface but fall back to the surface because of the force of gravity.

Measurements from wind tunnel experiments show that the relationship between the saltating dust flux is proportional to the cube of the wind speed (u^3) (Bagnold 1941; Shao and Raupach 1993) or proportional to u^4 (Gillette and Passi 1988) above a threshold value.

Data obtained from wind tunnel experiments shows that either relationship may hold true (Gillette 1977).

The critical wind speed required to move a particle at rest is called the threshold friction velocity (u_t). The threshold friction velocity is a function of various properties of the surface and of the particle size. Experimental studies have shown that u_t increases as the particles size increases because more energy is required to overcome the force of gravity to mobilise a heavy particle. The same experiment also shows that u_t increases for very small particles because these are bound together by strong inter-particle cohesion forces (Bagnold 1941; Iversen et al. 1976; Iversen and White 1982). Figure 1-1 shows how u_t increases for very small and very large particles when u_t is calculated using the empirical relationship derived by Iversen and White (1982). This empirical relationship has been derived by measuring u_t for different particle diameters in a wind tunnel. The model developed in this thesis uses this relationship to calculate the u_t and is based on a previous model developed by Tegen et al., (2002).

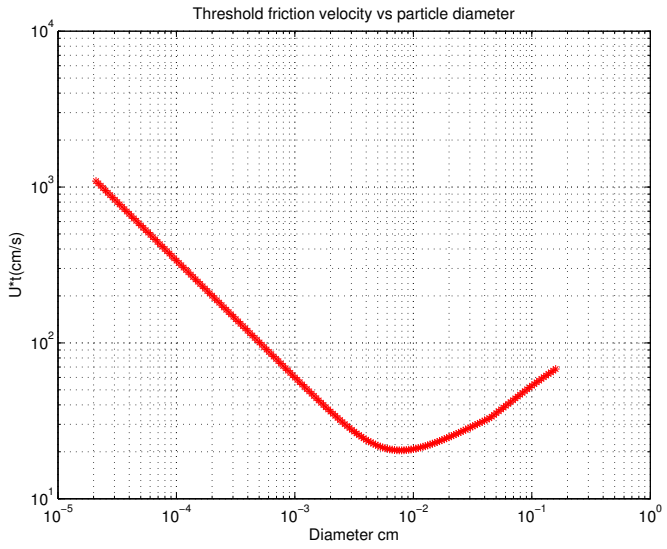

Figure 1-1 Threshold friction velocity as a function of particle size determined from semi-empirical relationship described by (Iversen and White 1982).

Another surface property that influences the u_t is the presence of non erodible materials such as vegetation cover and rocks on the surface. These obstacles reduce wind speed momentum which means a higher u_t is required to move a particle. The decrease in wind

speed caused by the presence of non erodible obstacles on the surface is calculated using the roughness length. The model developed in this work uses fixed roughness length of 0.01cm which is typical of a level desert (Seinfeld 1998). Roughness length can also be derived from remote sensing measurements (Prigent et al. 2005).

The u_t is also affected by soil moisture. Soil moisture increases the cohesion forces between the soil grains which increases the u_t and makes the soil more difficult to erode (Fecan et al. 1999).

The area available for dust emission is influenced by the presence of vegetation cover which protects the surface from erosion. Vegetation cover also reduces the erodibility of the soil because the root system binds the soil together. At high latitudes the presence of snow cover may reduce the area exposed to erosion.

Once saltation has commenced, a fraction of the saltating dust flux is converted into a vertical flux. Wind tunnel experiments have shown that the vertical flux is related to the horizontal flux by a constant value α (Shao and Raupach 1993). α is called the sandblasting mass efficiency. This is measure of how efficiently saltating particles are able to bombard the surface to release large quantities of fine grain material. Theoretically these values depend on the kinetic energy of the saltating particles and on the resistance of the surface to release fine material. However, dust cycle models often use experimentally derived values for α for different soil types (Marticorena et al. 1997).

Dust is lifted vertically into the atmosphere on regional scales by small scale convective disturbances known as dust devils or by intense large sand storms known as haboobs. Dust devils are rotating updrafts that develop over heated surfaces. Dust devils have diameters in the range of tens of meters and can persist for minutes (Goudie 2006). Haboobs are large dust storms that are generated when a cold front associated with thunderstorm activity moves along the surface. The cold air contains high wind speeds and a large vertical shear which entrains dust into the atmosphere. Haboobs can reach heights of approximately 1000m and last for several hours (Goudie 2006).

The inter-continental transport of dust is caused when dust laden air reaches high altitudes where it is then transported by the prevailing winds. Dust reaches high altitudes when a deep thermally mixed layer is formed by heating during the day or alternatively when a

cold front is present. In the Sahara the presence of a deep thermally mixed layer lifts dust to altitudes of 3-5km (Prospero 1981). It is then transported westwards across the Atlantic by easterly waves (Jones et al., 2003,2004). Measurements show that Saharan dust reaches the Caribbean (Prospero and Nees 1986). In Asia the lifting of dust to high altitudes is associated with the passage of cold fronts emerging from Siberia.

Dust is removed from the atmosphere by wet and dry deposition. Dry deposition is the removal of particles by gravity and is the dominant removal mechanism for large particles close to the source regions. Dry deposition is a two step process comprising of gravitational settling and turbulent mixing. Gravitational settling is the movement of a particle under gravity to the quasi sub laminar layer. This is a layer of static air just above the surface. As a particle falls it experiences an aerodynamic resistance in the opposite direction to the particle motion. An additional resistance is experienced as the particle crosses the quasi sub laminar layer to the surface.

Wet deposition is the removal of dust by precipitation such as rainfall, fog or snow. There are two types of wet deposition; below cloud scavenging and in-cloud scavenging. Below cloud scavenging occurs when a falling droplet collides with dust to remove it. In-cloud scavenging occurs when water vapour condenses on a dust particle. The particle then grows to a critical size and falls out of the atmosphere as precipitation.

The lifetime of the dust in the atmosphere is particle size dependent. Pye (1987) showed that the particle size distribution decreases with the distance from the source regions. Desert dust is dominated by particles with diameter from 0.1 to 10μm with a mean diameter of approximately 2μm which can reside in the atmosphere for several weeks (Jickells et al. 2005).

1.2 Dust-climate interactions

Mineral dust interacts with the climate by modifying the Earth's radiation budget and by transporting nutrients to the terrestrial and marine ecosystems. This section describes the various ways in which dust interacts with the Earth's system.

1.2.1 Direct radiative forcing

Mineral dust interacts with the Earth's radiation budget by scattering or absorbing incoming short wave solar radiation. Dust also has an impact on long wave radiation by absorbing radiation emitted from the surface. The change in net irradiance between the incoming and outgoing solar radiation is called direct radiative forcing. Direct radiative forcing is expressed in Wm^{-2} where a negative forcing indicates a cooling of the atmosphere and a positive forcing indicates a warming.

The way in which shortwave radiation interacts with an aerosol depends on the size of the particle (D_p) relative to the wavelength of the incident radiation (λ). Rayleigh scattering occurs if $\pi D_p/ \lambda << 1$. In the visible range, Rayleigh scattering affects small particles with diameter <=1μm (Seinfeld 1998). The pattern of the scattered light is symmetrical in the forward and backward direction.

Mie scattering occurs when $\pi D_p/ \lambda \approx 1$. The pattern of the scattered light is asymmetrical in the forward and backward direction. Mie theory provides a theoretical solution for the scattering of light assuming the particle has a spherical shape. The magnitude and direction of the scattering or absorption of radiation is calculated using a number of optical properties associated with particle.

The most important of these optical properties are the refractive index, the single scattering albedo and the asymmetry parameter. The refractive index provides a measure of how much radiation is scattered or absorbed by a particle. The single scattering albedo quantifies the scattering efficiency to the total light extinction by scattering and absorption. The asymmetry parameter describes the angle of the scattered radiation relative to the incident radiation.

Mineral aerosol can contain a wide variety of mixtures that may include many constituents, including quartz, iron oxides, various clays (mainly kaolinite, illite, and montmorillonite), calcite, gypsum, hematite. The relative abundance of each constituent will depend on the origin of the dust and whether it has changed during transport by interacting with other atmospheric constituents. These minerals vary in their particle sizes, shapes, density,

solubility, and chemical reactivity, hence their optical properties. As a consequence this will impact the way they attenuate light.

Durant et al., (2009) showed that uncertainties in the particle size distribution, composition, shape and the way in which dust particles are aggregated together, contributes to the uncertainty in the radiative forcing. For example it was shown that the difference between using laboratory and remote sensing observations for the single scattering albedo reverses the sign of the direct forcing by dust.

The magnitude of the radiative forcing can be estimated from measurements. Garcia et al., (2009) estimated from measurements of shortwave radiation at the surface that the shortwave radiative forcing was 1.55 Wm^{-2} in the Saharan region and -0.95 Wm^{-2} in Asia. The radiative forcing was calculated by taking the difference between the shortwave radiation at the surface with and without aerosols present. The radiation in an aerosol free atmosphere was calculated using a radiative transfer model. Mineral dust events were indentified using Total Ozone Mapping Spectrometer (TOMS) aerosol index and the aerosol loading was obtained from optical depth measurements from the Moderate Resolution Imaging Spectroradiometer (MODIS) sensor.

Aircraft measurements have shown that the shortwave radiative forcing by Saharan dust over the coast of West Africa is as large as -130Wm^{-2} (Haywood et al. 2003). This was calculated by taking the difference between the upward irradiance with and without aerosols. The upward irradiance with aerosol present was measured using an instrument that measures broadband radiation, fitted to the underside of an aircraft and facing downwards. The upwards irradiance without aerosols was calculated using a radiative transfer model.

Dust can absorb long wave radiation by absorbing radiation emitted from the surface. This has a heating effect on the atmosphere. The magnitude of the heating is dependent on the optical properties and vertical profile of the dust. Model estimates of the net direct radiative (long wave + short wave) forcing by mineral dust have been reported to be in the range of -0.56 to +1.0Wm^{-2} (Forster 2007). This estimate has been based on a number of modelling studies which assume an anthropogenic contribution of 0-20%. The estimate has been assigned an uncertainty of ± 0.2Wm^{-2} reflecting uncertainty in dust emissions and the contribution from anthropogenic sources.

1.2.2 Indirect radiative forcing and cloud formation

Dust indirectly affects the Earth's radiation balance by modifying cloud formation. Dust particles act as cloud condensation nuclei. These are sites upon which water vapour condenses to produce cloud droplets. If there is an increase in the number of cloud condensation nuclei but the amount of water vapour remains fixed, then cloud droplets will grow to smaller sizes. Smaller cloud droplets will enhance cloud reflectivity by scattering more incoming radiation. This has a cooling effect on the climate and is called the Twomey effect (Twomey 1974).

In addition to enhancing cloud reflectivity, the effect of smaller droplets in a cloud is that less particles grow to a critical size for precipitation, thus suppressing rainfall. Because of their smaller size, the droplets are less likely to collide with each other when they do precipitate. It has been proposed that this can form a positive desertification feedback loop when the following sequence occurs: dust aerosol increases, the effective radius of cloud droplet decreases, precipitation decreases and arid climate is strengthened (Han et al. 2008).

There is evidence that Saharan dust commonly acts as cloud condensation nuclei over the North Atlantic (Twohy et al., 2009). In that study they collected and analysed the residual nuclei of small cloud droplets over the eastern Atlantic and showed that Saharan dust was present.

Dust is believed to have effects on high level cloud formation by acting as nuclei for triggering ice formation. The presence of dust enables water droplets freeze at higher temperatures than normal. Pure water can become super cooled to temperatures near -40 °C. However, it has been shown that the presence of Saharan dust in clouds over Florida is causing water to freeze at temperatures between -5 °C and -8 °C (Toon 2003). When the ice crystals fall they grow by colliding with water droplets at lower altitudes which induces rainfall. Overall there may be two mechanisms at work such that dust reduces precipitation in low-level clouds and enhances precipitation in high-altitude clouds.

A study by Rosenfeld et al., (2001) investigated the effects of Saharan dust on cloud formation. They analysed remote sensing retrievals of cloud effective droplet radius in

clouds formed in dust laden and dust free conditions. It was found that clouds formed in dust laden conditions has smaller radii, had little coalescence (when small droplets collide to form larger droplets), and did not precipitate. In order for these clouds to precipitate they had to grow vertically to heights greater than the -12^{o}C isotherm level. This was confirmed by aircraft measurements taken at the same time. Drizzle and warm rain was measured in the dust free clouds, while there was little or no precipitation in the dust laden clouds.

Mahowald and Kiehl (2003) showed that there was a positive correlation (0.2-0.5) between mineral dust concentrations at Barbados and remote sensing derived low cloud amount over the coast of North Africa over a period of 16 years. Barbados dust measurements were used as a proxy for dust loading over the North Atlantic (Mahowald et al., 2003). It was suggested that the correlation between low cloud amount and dust loading over the North Atlantic was because dust acted as cloud condensation nuclei which increased the lifetime of the cloud by reducing precipitation.

1.2.3 Biogeochemical cycles

There is evidence to suggest that dust provides nutrients such as nitrogen and phosphorus to the marine ecosystem (Herut et al. 1999). In the open ocean, dust deposition from the atmosphere plays an important role in supplying iron to the ocean (Jickells et al. 2005). It has been hypothesised that during glacial times, iron-rich dust from Patagonia deposited into the Southern Ocean caused an increase in plankton productivity which increased the drawdown of CO_2 from the atmosphere to the ocean, resulting in a cooler climate (Martin 1990). The Southern Ocean is a high-nutrient, low-chlorophyll (HNLC) region which is limited in iron. Open ocean experiments have shown that iron deposited into this region does increase carbon fixation in the surface waters (Boyd et al. 2000; Tsuda et al. 2003; Coale et al. 2004). In addition to this, laboratory studies have verified that phytoplankton productivity increase when iron is added to sea water [Martin and Fitzwater 1988]. The iron fertilisation hypothesis remains controversial, however, because experiments have not confirmed whether iron-fertilisation results in a net drawdown of CO_2 (Buesseler et al. 2004).

It has been suggested that iron needs to be acidified prior to its deposition to the ocean to make it biologically available (Meskhidze et al. 2005; Meskhidze et al. 2007). This is

because iron in dust is usually in mineral form which has low solubility in sea water. Meskhidze et al. (2005) tracked the movement of two dust plumes from the Gobi Desert to the Pacific Ocean. One plume caused an enhancement in plankton productivity in the Pacific, but the other did not. The plume that did increase plankton productivity had been acidified by sulphur dioxide caused by pollution in China. They concluded that this converted the iron into a more soluble form.

Swap et al., (1992) showed that Saharan dust provides nutrients to the Amazon Basin. This is particularly import for this region as nutrients are leached out of the soil by heavy rainfall. It has estimated that of the 240Mt of dust that is transported annually from Africa, 50Mt reaches the Amazon every year providing essential micronutrients (Kaufman et al. 2005). This links the ecosystem of the Amazon rain forest to the ecosystem of the Sahara/Sahel region over large distances by the mechanism of dust transport.

There is evidence that dust provides nutrients to the Cape Floristic region of south-western South Africa (Soderberg and Compton 2007). The region is described as a 'biodiversity hot spot' and contains an abundance of Fynbos (shrubland) vegetation even though the bedrock is nutrient poor. They showed that dust deposition from the interior of the continent and from anthropogenic sources provided the nutrients necessary for the ecosystem to flourish. Dust originating from the Sahara has also been found to contribute to soil development in North East Gran Canaria (Menendez et al. 2007)

1.2.4 Dust and tropical storm formation

A correlation has been found between tropical cyclone activity in the North Atlantic and the dust transported from West Africa (Evan et al. 2006). They found using TOMS aerosol index, that dust loading over the North Atlantic was anti-correlated with tropical storm occurrences. Dust from North Africa is transported across the Atlantic in the Saharan air layer. This is a stable layer of hot dry air that moves over the marine boundary layer and allows dust to be transported for long distances. It was suggested that when the warm dry dusty air is introduced into a storm it disrupts the convective formation of the tropical cyclone vortex.

Wu et al., (2006) analysed the effect of the Saharan air layer on the formation of Hurricane Isabel in 2003 using a mesoscale atmospheric circulation model and remote

sensing temperature and humidity profiles from the Atmospheric Infrared Sounder (on board the Aqua satellite). It was found that the presence of the Saharan air layer may have delayed the formation of the hurricane Isabel.

1.2.5 Carbon dioxide fertilisation

Changes in vegetation cover caused by increased levels of atmospheric CO_2 may have an impact on future dust source areas. The increase in plant growth caused by exposure to elevated levels of CO_2 is called CO_2 fertilisation. Plants respond in several ways to increased levels of CO_2. Laboratory studies have shown that when a plant is exposed to elevated levels of CO_2, the stomata become smaller (Morison, 1985). This is because the plant can take up all the CO_2 it requires while loosing less water. This increases the water use efficiency in the plant which enhances it potential to survive under arid conditions.

Desert ecosystems are believed to be very responsive to elevated levels of CO_2. Smith et al., (2002) studied the response of a desert ecosystem to elevated CO_2. They exposed a sample of the Mojave Desert to 550ppm of CO_2 using a free-air CO_2 enrichment facility (FACE). They observed increased plant productivity. In a year with high rainfall, the plant productivity of a dominant perennial shrub doubled. In addition to this, they found an increase in the productivity of invasive species of grass in response to elevated CO_2. This has implications for dust source areas in a future world with elevated CO_2.

The impact CO_2 fertilisation on dust source areas has been studied using the BIOME4 model (Mahowald and Luo 2003; Mahowald 2006; Mahowald 2007). These studies predict that dust emissions will increase in the future if the CO_2 fertilisation effect is included. This is because the increase in water use efficiency enhances the ability of vegetation cover to survive under arid conditions. When CO_2 fertilisation is excluded a decrease in dust emissions are predicted as vegetation is unable to adapt to the increased aridity.

1.3 Temporal variability in the dust cycle

Atmospheric dust loadings are highly variable in time. On daily time scales visibility data shows that dust storms are more frequent during the day than at night (N'tchayi Mbourou 1997). This is caused by the heating of the surface during the day which causes convective disturbances, resulting in higher wind speeds. A study by Schepanski et al., (2009) showed

that that 65% of dust source activation occurs between 0600-0900 UTC. This was found by analysing fifteen-minute Meteosat Second Generation (MSG) retrievals of dust over the Sahara and the Sahel.

On millennial time scales times scales, dust records from the EPICA ice core shows that over the last 800,000 years there has been a 2-25 fold increase in dust deposition rates during glacial periods compared to inter-glacial periods (Lambert et al. 2008).

This thesis is concerned with seasonal and inter-annual variability in atmospheric dust for the modern climate. The next section describes the seasonal and inter-annual variability in the dust cycle from observational studies for the major dust producing regions.

1.3.1 Seasonal variability

North Africa

A seasonal cycle in North African dust loading has been observed from space using Advanced Very High Resolution Radiometry (AVHRR) data (Evan et al. 2006), MODIS data (Kaufman et al. 2005) and TOMS aerosol Index (Prospero et al. 2002). The observations show that atmospheric dust loading over North Africa has a strong seasonal cycle which has a maximum in the summer (JJA) and a minimum in the winter (DJF). These studies show that there is a change in the transport pathway between JJA and DJF due to a shift in the inter-tropical convergence zone (ITCZ).

The ITCZ is the point near the equator at which the dry north-easterly trade winds from the Northern Hemisphere converge with the humid south-easterly trade winds from the Southern Hemisphere. The position of the ITCZ varies throughout the year. In JJA the ITCZ shifts northwards and dust is transported towards the Caribbean while in DJF ITCZ shifts northwards and dust is transported towards South America. The increase in North African dust transported to the Caribbean during JJA has been observed from measurements of dust concentrations at Barbados. The measurements show that dust concentrations are 10 times higher in JJA than in DJF (Prospero and Nees 1986).

Arabia

Measurements show that maximum dust activity in the Arabian Peninsula occurs in JJA (Kambezidis and Kaskaouti 2008). They analysed aerosol optical depth from the

AERONET network at a site in Saudi Arabia that was dominated by desert aerosol. The highest aerosol optical depths were measured in JJA.

Asia

Observations of dust storms in Asia show that maximum activity occurs in spring, caused by an increase in wind speeds linked to cold fronts emerging from Siberia (Littmann 1991; Goudie and Middleton 1992; Wang et al. 2004). Remote sensing observations indicate that vegetation cover may play a role in controlling the seasonal cycle in dust emissions from Asia (Zou and Zhai 2004). In that study it was found that a decrease in NDVI over Northern China and in Inner Mongolia corresponded with an increase in dust storm events. The spring peak in dust storms was attributed to a combination of factors. Firstly, the NDVI in spring was low, indicating that vegetation cover was sparse at this time of year. This was combined with an increase in synoptic systems emerging from Siberia which caused an increase in the frequency of strong winds. Finally, the increase in temperature between winter and spring melted the frozen soil and snow cover. It was suggested that together these factors contributed to the observed increase in dust storms in spring. The impact of vegetation cover on the seasonality in dust emissions will be investigated in further detail in chapter 4.

North America

Analysis of visibility measurements and total suspended particulate (TSP) concentrations at metrological stations in Tennessee in the northern US show that the peak in dust activity occurs in the spring (Orgill and Sehmel 1976). The spring maximum was related to an increase in wind speeds $>7ms^{-1}$ which was associated with the spring cyclonic and convective storm activity. Stout (2001) analysed particulate concentrations at sites in the Southern High Plains of North America and found that the maximum in spring was not only related to wind speeds, but that other factors such as soil moisture and the seasonal growth of cotton also played a role in determining the seasonality. In the southern US (Mexico and California) remote sensing measurements from TOMS aerosol index show that the seasonal cycle begins in spring (April–May) and peaks in June-July and ends in August-September (Prospero et al. 2002).

Australia

TOMS aerosol index data shows that dust loading over Australia reaches a maximum between December-February (the Austral summer) and a minimum in May (Prospero et al. 2002). McTainsh and Pitblado (1987) analysed dust storm frequencies from meteorological

stations in Australia and showed that in the northern region (New South Wales and Queensland) the peak activity occurs in the spring and early summer while in the southern region (Victoria and New south Wales) the peak occurs in the summer. This seasonality was related to the difference in rainfall regimes in the north and the south of Australia. In both areas the most frequent dust storms occurred during the months with the highest wind speeds.

South Africa

Remote sensing observations show that dust activity in South Africa is centred over two regions; the Etosha Pan in northern Namibia which is a salt pan and the Makgadikgadi depression and Pans in Botswana which is a sandy alkaline clay pan (Prospero et al. 2002). During June-July these pans dry out and dust deflation occurs. An increase in dust activity begins from June-July and reaches a maximum between August and October.

South America

There is conflicting information about the seasonal cycle of dust activity in South Africa. Remote sensing data from the TOMS detector shows there is dust activity over Patagonia which has a maximum in the Southern Hemisphere winter (Prospero et al. 2002). In contrast, data from the MODIS sensor shows that Patagonia is not an active dust source (Kaufman et. al. 2002). Measurements of the dust deposition flux at sites in the Patagonian desert show that in general the maximum deposition flux occurs in NDJ when wind speeds are highest and precipitation is low (Gaiero et al. 2003).

These observational studies summarised in this section have highlighted the fact the seasonality in the dust cycle is regionally dependent and may involve a combination a number of climatic factors. In chapter 4 the new dust model developed in this work is used to investigate which factors control the seasonality in the dust cycle in individual dust regions.

1.3.2 Decadal variability

There are very few observations of dust in the atmosphere that span decades. One of the longest continuous measurements of dust concentrations have been made at Barbados since 1965 (Prospero and Nees 1986). This dataset has been useful to study the inter-annual variability in North African dust emissions. The measurements at Barbados show that there

was a four fold increase in dust concentrations during the 1980s relative to the 1960s. This variability has been correlated with rainfall deficits in sub-Saharan Africa in the previous year (Prospero and Nees 1986; Prospero and Lamb 2003).

Remote sensing data has provided a useful tool for observing inter-annual variability in the atmospheric dust loading. North Africa is the worlds largest dust source; therefore, many studies have focused in this region.

Dust loading over North Africa and the North Atlantic has been observed from space using TOMS and Meteosat images (Chiapello and Moulin 2002). They showed by analysing 18 years of dust optical thickness observations that a large amount of inter-annual variability occurred in winter (December–March). There were years (e.g. 1986) where winter dust was almost absent and years (e.g. 1989) where winter dust was almost as high as in summer.

Satellite observations have related the variability in North African dust to the North Atlantic Oscillation (NAO) (Moulin et al. 1997; Chiapello and Moulin 2002; Chiapello et al. 2005; Evan et al. 2006). The NAO is a large-scale fluctuation in atmospheric pressure between the sub-tropical high pressure system located near the Azores in the Atlantic Ocean and the sub-polar low pressure system near Iceland (Hurrell 1995). The permanent high-pressure system over the Azores and the permanent low-pressure system over Iceland control the direction and strength of westerly winds across the North Atlantic. The relative strengths of these pressure systems vary from year to year. The variation is known as the NAO and is measured by taking the pressure difference between these two locations. If there is a large difference in the pressure between the two locations the NAO index is said to be high. This causes an increase in westerly winds over the Atlantic which results in cooler and wetter conditions over Europe and drier that normal conditions over North Africa. This leads to enhanced dust export due to the lack of precipitation. In contrast, if the pressure difference is small, the NAO index is small and westerly winds over the North Atlantic are suppressed. This leads to cold dry conditions over Europe and an increase in precipitation over North Africa. More precipitation results in more dust removal by wet deposition and less dust emissions due to increased soil moisture.

Measurements of visibility used as a proxy for dust storm activity have been made at meteorological stations since the 1900s (Mahowald et al. 2007). This type of data,

although, semi-qualitative in nature, has been useful to observe long term changes in dust storms frequencies. Dust storm frequencies in Asia have declined since the 1950s (Zhao 2004; Wang et al. 2006; Guo and Xie 2008; Kim 2008). Several reasons have been put forward to explain this downward trend. Zou and Zhai (2004) studied dust storm activity over Northern China and proposed that changes in vegetation cover was responsible for the downward trend in dust storm activity. Other studies has have related the decrease in dust storm frequency to a decrease in local wind speeds (Wang et al. 2006), a decrease in tropical cyclone activity (Qian et al. 2002) or climatic indices such as the North Atlantic Oscillation, the Pacific Decadal Oscillation or El Nino (Hara et al. 2006).

1.4 Advancements in dust cycle modelling

Modelling the dust cycle is a relatively new science which began in the early 1990s. Since then several advancements have been made in dust cycle modelling. However, a large discrepancy still exists in estimates of the annual mean emissions predicted by different models. Ranges from 805 to 2600 $Tgyr^{1}$ have been reported in the literature (Ginoux et al. 2001; Tegen et al. 2002; Zender et al. 2003a; Grini et al. 2005; Cakmur et al. 2006). The variation in the model estimates may arise from the differences in the way models parameterise the different physical processes in the dust cycle. Also the datasets used to drive the models and describe the properties of the land surface are different between models. Models are run over different time periods so uncertainty in the estimates of the annual mean emissions is caused by inter-annual variability in surface emissions.

This section discusses the way in which several key processes have been treated in dust cycle models. These processes are; the treatment of vegetation cover, wind speed parameterisation, preferential dust source regions and dust transport and removal processes.

A dust model inter-comparison table has been compiled. Table 1.5-1 shows a selection of some of the models developed to simulate the modern dust cycle listed in chronological order, with a brief description of how each model treats some of the key process in the dust cycle. The majority of the models are off-line. This means that they are forced by external metrological fields and the dust has no radiative feedback on the system. The exception to this are the models of Tegen and Miller (1998), Woodward (2001), Cakmur et al. (2006) and Yue et al. (2009) which are on-line. The estimated annual mean surface emissions

predicted by the models are included in Table 5.1-1. Each model considers a different particle size range and some of the dust loadings are calibrated to match observations.

1.4.1 Treatment of wind speed dependency in dust models

Dust models have treated the wind speed dependency in different ways. Joussaume (1990) simply assumed that the dust flux was linearly proportional to the wind speed. The parameterisation did not include a threshold wind speed for dust emissions. Subsequent models (Tegen and Fung 1994; Tegen and Miller 1998; Mahowald et al. 1999) assumed that the dust flux was related to the cube of the wind speed above a threshold value. The threshold values were determined from experimental studies.

It can be seen from that the most recent models parameterise the relationship between the dust flux and the wind speeds using the scheme developed by Marticorena and Bergametti (1995). This scheme relates the dust flux to the cube of the wind speed above a threshold value where the threshold wind speed is calculated as a function of surface roughness and the particle size.

Dust models treat surface roughness in different ways. Cakmur et al., (2006) used data from the European Remote Sensing (ESR) microwave scatterometer to identify regions with low surface roughness. Other models use a fixed value for the roughness length. Lunt and Values (2002) used a fixed roughness length of 1.68cm. This value was used because it gave a good match with the roughness length of the HadAM3 model which produced the wind speeds used to drive their dust model. Zender et al. (2003a) used a globally fixed surface roughness value derived from wind tunnel experiments.

Some models have included the effect of soil moisture on the threshold wind speed by using empirically derived relationships to account for the fact that an increase in soil moisture increases the threshold wind speeds (Ginoux et al. 2001; Ginoux et al. 2004; Tanaka and Chiba 2006)

Several models have parameterised the effect of sub-grid scale gustiness on the dust flux. These are small scale convective disturbances which cause short bursts of high wind speed in which the u_t may be exceeded. Because there is a cubic relationship between the dust

flux and the wind speeds, short periods of high wind speed may have a large impact on the total dust emissions.

Models have treated gustiness in different ways. Grini et a. (2005) applied a probability density function to the wind speed and found that excluding gustiness in the model produced much lower emissions. Cakmur et al., (2006) parameterised sub-grid scale gustiness by constructing a probability distribution of wind speeds within each grid box that depends upon the speed explicitly calculated by a GCM and the magnitude of fluctuations about this speed. It was found that that including gustiness significantly improved the estimate of the dust loading compared to observations. Lunt and Valdes (2002) included two types of gustiness, convective gust and eddies gusts. The convective gusts were calculated using an empirical relationship derived from measurements of gustiness and convective precipitation (Redelsperger et al. 2000). Gustiness due to eddies caused by heating of the surface were calculated as a function of the surface temperature.

1.4.2 Treatment of transport and removal processes in dust models

Table 1.5-1 lists the chemical transport models used by dust cycle models to transport dust in the atmosphere. It can be seen that the horizontal and vertical resolution of the chemical transport models has improved for later models allowing a better representation of the horizontal and vertical transport.

Each of the dust cycle models listed in have parameterised the process of dust removal by dry deposition which consists of gravitational settling and turbulent mixing. Dust removal by sub-cloud scavenging is included in all the models because it is relatively simple to parameterise, while only two have included in-cloud scavenging (Zender et al. 2003a; Tanaka and Chiba 2006). A fixed scavenging coefficient has been used in the majority of models (Tegen and Fung 1994; Tegen and Miller 1998; Mahowald et al. 1999; Lunt and Valdes 2002; Mahowald et al. 2002; Tegen et al. 2002; Cakmur et al. 2006).

1.4.3 Treatment of preferential dust source regions

Preferential dust source regions are areas that have accumulated alluvium sediment for example dried out palaeo lakes and river beds. They are believed to act as dust emitting 'hot spots'. The Bodele depression north east of Lake Chad is one such example of a dust

emitting 'hot spot' (Prospero et al. 2002). Because these regions occur in topographic depressions some dust models have used digital elevation maps to identify preferential dust source regions. Ginoux et al., (2001) and Zender at al., (2003a) have represented preferential dust source regions by relating the difference in height of two grid points in relation to the local mean surface elevation.

Alternatively, Tegen et al., (2002) used a high resolution water routing and storage model HYDRA (Coe 1998) to calculate areas in which palaeolake beds would have existed in the past. HYDRA uses a land surface topography map to calculate the extent of lakes as a function of precipitation, run off and surface evaporation. The HYDRA model is run using unlimited precipitation and the difference between simulated lakes and lakes present today indicates places where lakes would have existed in the past under a wetter climate.

Remote sensing reflectivity data has also been used to detect preferential dust source regions. Reflectivity data from the MODIS sensor has been used to determine regions of high erodibility (Grini et al. 2005).

1.4.4 Treatment of vegetation cover in dust models

One of the earliest dust cycle models developed did not explicitly represent vegetation cover (Joussaume 1990). It was simply assumed that dust emissions occurred when the soil moisture content was low. At that time it was believed that vegetation cover did not constrain dust emissions.

Subsequent models (Genthon 1992; Tegen and Fung 1994; Tegen and Fung 1995; Andersen and Genthon 1996; Andersen et al. 1998; Tegen and Miller 1998) used the Matthews vegetation map (Matthews 1983) to identify desert or sparsely vegetated regions. This was a static global map of vegetation types compiled from existing maps of vegetation and remote sensing data on a 0.5 x 0.5 degree spatial resolution. Using this map it was possible to prescribe biomes such as desert, grassland and scrublands as dust sources.

There were two limitations to this approach. The first was that it did not account of the fact that the fractional coverage of bare soil may vary for different biomes. The second was it did not account for seasonal and inter-annual growth in vegetation cover which could

potentially cause an expansion and contraction of dust source regions. Therefore, this type of model could not be used to simulate the seasonal or inter-annual variability in the dust cycle caused by changes in vegetation cover. Furthermore, these models could not be used to simulate the dust cycle in the past or in the future.

(Mahowald et al. 1999) first included model derived vegetation cover in a dust cycle model. The authors used BIOME3, the Equilibrium Biogeography-Biogeochemistry model (Haxeltine and Prentice, 1996) to simulate the distribution of vegetation types on the surface. This model predicted the distribution of vegetation cover in its equilibrium state for a given climate and atmospheric CO_2 concentration. Dust source regions were related to the maximum leaf area index (LAI) predicted by BIOME3, when the LAI was below a defined threshold value.

This was a significant development because it meant that the model could be used to simulate the dust cycle in the past or the future. Indeed in that study, the model was used to investigate the cause of increased in dust deposition rates during the Last Glacial Maximum which have been observed in ice core records. A similar approach was taken by Lunt and Valdes (2002) and Mahowald et al., (2002) who used BIOME4, the successor of BIOME3, to calculate dust source areas using the annual mean LAI. The limitation of these models was that they simulated vegetation cover in its equilibrium state with the climate and did not include vegetation phenology.

At the same time a new type of dust cycle model was being developed which did include vegetation phenology. Tegen et al, (2002) included vegetation phenology by combining remote sensing NDVI measurements (Braswell et al. 1997) with the BIOME4 model. The BIOME4 model was used to identify potential biomes that emit dust. Remote sensing NDVI was converted into FPAR using an empirical relationship (Knorr and Heimann 1995) and the FPAR was used as a proxy for the density of vegetation cover. It was assumed that in grass dominated biomes the dust source varied linearly with the monthly FPAR below a threshold value. Shrub dominated biomes were assumed to emit dust all year around if the FPAR was below a threshold value. This approach made it possible to predict the seasonal changes in the dust source areas due to changes in vegetation cover. It was found that including seasonal changes in vegetation cover produced better estimates of dust emission from Asia.

One of the limitations of the Tegen et al, (2002) model was its dependency on remote sensing NDVI. This limited the period for which the model could be run to the period when the NDVI data was available. Another limitation of the model was that it used BIOME4 soil moisture to suppress dust emissions which is inconsistent with the vegetation cover derived from NDVI data.

Broadly speaking two categories of dust cycle models have been developed to date; models which use remote sensing data to describe vegetation cover on the land surface and models which use the Equilibrium Biogeography-Biogeochemistry models (BIOME3 or BIOME4) to simulate the distribution of vegetation cover. The latter category can be used as predictive tools to estimate how the dust loading will change in the future under different climatic conditions.

The predictive models currently available are unable to simulate the expansion and contract of dust source areas caused by the transient response of vegetation cover to changes in the climate. As a consequence, it is not possible to test whether decadal scale changes in the dust loading are caused by natural variability or by human activity.

1.5 Aims

The research summarised in section 1.2 clearly shows that mineral dust plays an important role in the Earth's system. The longest continuous measurements of dust concentrations have been made at Barbados (Prospero and Nees 1986). Concentrations were low in the mid to late 1960s but increased sharply in the early 1970s and have remained high ever since. Indeed a four fold increase was observed between the 1960s and the 1980s. The increase in dust concentrations during the 1970s has been associated with the onset of drought in sub Saharan Africa.

Studies have shown that dust concentrations at Barbados are anti-correlated with precipitation in the Sahel during the previous year (Prospero and Nees 1986; Prospero and Lamb 2003; Evan et al. 2006). The study by Evan et al., (2006) suggested a three way connection between rainfall, vegetation and dust in the Sahel as follows; decreased precipitation in the Sahel reduces vegetation cover which increases the dust source areas and hence dust emissions.

This theory is supported by measurements of NDVI from the AVHRR which show that vegetation cover in the Sahel changes in response to precipitation (Tucker et al. 1991). This results in a north-south movement of the Sahara-Sahelian boundary line. During 1980-1984 the Sahara-Sahelian boundary moved southwards by 240km. This corresponded to a 15% increase in the area of the Sahara in 1984 compared to 1980.

This raises the question; is an expansion of the Sahara caused by changes in vegetation cover in the Sahel, responsible for the high dust concentrations at Barbados during the 1980s or is some other process at work?

Only one modelling study has been reported in the literature which aimed at understanding the high dust concentrations during the 1980s at Barbados relative to the 1960s (Mahowald et al. 2002). Vegetation cover was simulated using the BIOME4 model in increments of five years from 1950 to 2000. By doing this, they assumed that vegetation cover did not respond to changes in the climate any quicker than 5 years. This assumption is inaccurate because measurements show that the response of vegetation cover in the Sahel to rainfall is much faster than this (Nicholson et al. 1990; Herrmann et al. 2005). These studies found that NDVI over the Sahel is correlated with rainfall of the concurrent month plus the two previous months. The model by Mahowald et al. (2002) was unable to predict the high dust concentrations at Barbados during the 1984 relative to 1966. They concluded that there must have been an increase in the North African dust source. This was either caused by a shift in vegetation cover or an increase in land use, which degraded the soil enhancing emissions from the region.

It is not possible, using currently available dust cycle models, to test whether a vegetation shift in the Sahel is responsible for the high dust concentrations measured at Barbados during the 1980s relative to the 1960s.

Dust models which use remote sensing data to describe the vegetation cover are unsuitable for this type of study because of the lack of remote sensing data prior to the 1980s. Models which use BIOME4 are also limited because these models are unable to capture the transient response of vegetation cover to changes in the precipitation, temperature, solar radiation and CO_2. This means that these models are unable to simulate the expansion or contraction of dust source regions caused by the dynamic response of vegetation cover to the climate.

For this reason, the primary aim of this thesis is to develop a new dust cycle model that uses a dynamic global vegetation model (DGMV) to predict the distribution of vegetation cover. A DGVM simulates the dynamic response in vegetation cover by simulating time dependent ecological processes such as photosynthesis and transpiration, vegetation disturbance by fire, competition for resources, establishment and mortality.

An additional advantage of using a DVGM within the framework of a dust cycle model is that the water balance will be consistent with vegetation cover. The fact that the water balance is calculated dynamically means that simulated soil moisture and snow cover can be used in the dust model to suppress dust emissions.

A of choice of DGVMs are available; the IBIS model (Foley et al. 1996), HYBRID (Friend et al. 1997), VECODE (Brovkin et al. 1997), SDGVM (Woodward 1998), TRIFFID (Cox 2001), ORCHIDEE (Krinner et al. 2005). It is decided to use the Lund-Potsdam-Jena (LPJ) DGVM (Sitch et al. 2003) in this study for a two reasons. The first reason is that LPJ is a stand alone DGVM unlike other DGVMs which are used as land surface schemes within GCMs (Cox 2001; Krinner et al. 2005). The second reason is that development work is currently carried out on LPJ at the department of Geographical science at Bristol University. The new dust model is referred to frequently in this thesis, so from this point onwards; it referred to as the 'LPJ-dust' model.

Using a DGVM within the framework of a dust cycle model provides a unique opportunity to test whether the expansion and contraction of dust source regions in response to vegetation changes has a significant impact on the dust loading on decadal time scales. Studying the vegetation changes in the Sahara-Sahel is only one potential application of the LPJ-dust model. The model can be used to study inter-annual viability in other regions where vegetation cover is believed to constrain dust emissions.

In Asia observations show that that there has been a decreasing trend in spring time dust storms since the mid-1950s to mid-1990s and an increasing trend from 1997-2002 (Lu et al. 2003). A study by Zou and Zhai (2004) showed that the frequency of springtime dust storms in Northern China and Central and Eastern Mongolia was anti-correlated with NDVI measurements. Other studies have related the variability to changes in wind speeds (Qian et al. 2002; Hara et al. 2006; Wang 2006). Assuming there is no anthropogenic

disturbance of the vegetation cover, the LPJ-dust model can be used to investigate which processes are responsible for the trends in springtime dust storm activity in Asia.

Another potential application of the LPJ-dust model is that it can be used to investigate the cause of seasonality in the dust cycle. The observational studies summarised in section 1.3.1 show that there is strong seasonality in the dust cycle. No modelling studies have been reported in the literature which investigates the cause of this seasonality. Therefore, one of the aims of this thesis is to use the LPJ-dust model to investigate which processes control the seasonal variability in the dust cycle.

As with any dust cycle model there will be aspects of the model where there is uncertainty. It was seen in that estimates of the annual mean surface emissions vary by a factor of 3. Uncertainty can arise from the input meteorological data used to drive the model, by the values chosen for parameters and by the parameterisations used to represent physical processes. It will be seen in the model description contained in Chapter 2, that several threshold parameters are required to determine surface emissions. It is possible to reduce the uncertainty in these threshold values by tuning the model to find an optimal fit between the model and measurements. Indeed an objective tuning of a dust cycle model has not been carried out to date. For this reason a dust model tuning is carried out in this thesis.

The specific objectives of this thesis are as follows:

1. To develop a dust cycle model that uses the LPJ DGVM to calculate dust source areas as they change in response to vegetation dynamics.

A description of the dust cycle model is contained in chapter 2. This includes details of how dust source areas are calculated from LPJ. A description of the dust emission scheme, the chemical transport model and the way in which dust is removed from the atmosphere is also described. A baseline dust simulation is carried out and the regional surface emissions predicted by the model are compared to emissions from six other modelling studies.

1. To improve the performance of the LPJ-dust model by carrying out a tuning exercise.

To improve the performance of the dust model the threshold parameters used to determine surface emissions and different sub cloud scavenging schemes are tested. The model tuning is described in chapter 3. The performance of the model is evaluated against multiple measurement datasets.

3. To evaluate how well the model reproduces the seasonal variability in dust concentrations and to carry out sensitivity studies to test which processes control the seasonality in the dust cycle.

Chapter 4 investigates how well the tuned model reproduces seasonal changes in dust concentrations. The seasonality in the total column dust loading predicted by the LPJ-dust model is compared to TOMS aerosol index. Seasonal changes in surface concentrations are compared to measurements from University of Miami aerosol network. Regions where the model performs well and poorly are identified and discussed. A series of sensitivity experiments are carried out to test which processes are responsible for the seasonality in surface emissions and the atmospheric dust loading.

4. *To test if decadal scale changes in vegetation cover can explain observed trends in the dust cycle.*

In Chapter 5 a study is carried out to investigate if vegetation changes in the Sahel can explain the high dust concentrations measured at Barbados during the 1980s relative to the 1960s (Mahowald et al. 2002). Sensitivity studies are carried out to test if changes in vegetation cover have contributed to the decline in dust storms in Northern China (Zou and Zhai 2004). To gauge how well the LPJ-dust model predicts inter-annual variability in surface concentrations from 1980-2000 a comparison is made with another modelling study in which remote sensing data is used to describe vegetation cover on the land surface (Mahowald et al. 2003).

Finally, the degree to which these objectives have been met are discussed in chapter 6.
This chapter also highlights areas for future research.

Reference	***Transport Model/ Dimensions***	***Particle radius µm***	***Annual Emission Mt/yr***	***Sources***	***Emission Scheme***	***Removal***	***Preferential source regions***
Joussaume (1990)	LMD AGCM	1	-	Sources have soil moisture less than 2mm in February and August calculated from GCM.	Flux ~ u No calculation of u_t	Dry deposition Size dependant in- cloud scavenging	No
Tegen & Fung (1994)	GISS 4^o x 5^o	0.1 -50	3000[a]	Matthews vegetation map (1983)	Flux ~ u^3 u_t fixed at 6.5ms^{-1}	Dry deposition Size independent sub-cloud scavenging	No
Tegen & Miller (1998) On-line	GISS AGCM 4^ox5^ox9	0.1– 8	940[b]	Matthews vegetation map (1983)	Flux ~ u^3 u_t 4-10 ms^{-1}	Dry deposition Size independent sub-cloud scavenging	No- but human disturbed sources are represented using Middelton map (1992) and Matthews map (1983)
Mahowald et al., (1999)	TM3 4^ox5^ox19	2.5	3000[b]	BIOME3 Leaf Area Index	Flux ~ u^3 u_t fixed at 5ms^{-1}	Dry deposition Size independent sub-cloud scavenging	No
Ginoux et al., (2001)	GEOS DAS GOCART 2^o x 2.5^o x 20-26	0.1-6	1604 - 1960[a]	Source regions are defined as topographic lows using a digital elevation map combined with bare soil from AVHRR	Flux ~ u^3 u_t a function of particle size and soil moisture using Belly (1964)	Dry deposition mixing, rainout and wash out	No
Woodward (2001) On-line	HadAM3 2.5^ox3.75^ox 19	0.03-30	Not specified	Vegetation type from the IGBP land use dataset	Marticorena & Bergametti 1995	Dry deposition Size dependent sub-cloud scavenging	No

Tegen et al., (2002)	TM3 3.75°x5°x 19	0.1 – 220	805 ± 82[b]	Vegetation types identified using BIOME4 model Seasonality from NDVI data	Marticorena & Bergametti 1995	Dry deposition Size independent sub-cloud scavenging	Yes Enhanced erodibility from Palaeolake beds identified using HYDRA model (Coe 1998)
Lunt & Valdes (2002)	TOMCAT 2.5° x2.5° x32	0.032 – 1	2100[b]	BIOME4 Leaf area Index	Marticorena & Bergametti 1995 Gustiness parameterisation included	Dry deposition Size independent sub-cloud scavenging	No
Mahowald et al., (2002)	MATCH 1.8.°x1.8°x 28	0.05 – 5	Time series modelled	BIOME3 Leaf Area Index Average of 5 years in increments from 1950-1980	Marticorena & Bergametti 1995	Dry deposition Size independent sub-cloud scavenging	Yes Enhanced erodibility from topographic lows using a digital elevation map
Werner et al., (2002)	TM3 4°x5°x 19	0.1-219	1060 ± 194[b]	Vegetation types identified using BIOME4 model Seasonality from BIOME4 FPAR	Marticorena & Bergametti 1995	Dry deposition Size independent sub-cloud scavenging	No
Zender et al., (2003)	MATCH 0.5°x0.5°x 25	0.1 – 10	1490 ± 160[b]	Satellite derived vegetation dataset of LAI	Marticorena & Bergametti 1995	Dry deposition Size dependant in-cloud and sub-cloud scavenging	Yes Enhanced erodibility from topographic lows using a digital elevation map
(Ginoux et al. 2004) IAV	GEOS DAS GOCART 2° x 2.5° x 20-40	0.1-6	1950-2400	Source regions are defined as topographic lows using a digital elevation map combined with bare soil from AVHRR	Marticorena & Bergametti 1995. u_t modified by soil moisture using Belly (1964)	Dry deposition mixing, rainout and wash out	No

(Grini et al. 2005)	CTM2 8^ox10^ox9	4.82	1500[a]	MODIS reflectivity identifies erodible surface	Marticorena & Bergametti 1995 Probability density function for sub-grid scale wind variability	Dry deposition Size-independent washout	Yes Enhanced erodibility from topographic lows using a digital elevation map
(Cakmur et al. 2006) On-line	GISS ModelE AGCM 4^ox5^ox10 (10 in troposphere)	1 - 8	1500 - 2600[a]	ERS microwave scatterometer data to identify areas with low surface roughness	Flux ~ u^3 u_t a function of particle size and soil moisture Probability density function for sub-grid scale wind variability	Dry deposition Size independent sub-cloud scavenging	Yes, 4 different ways to prescribe preferential dust source region tested- remote sensing, HYDRA & topographical lows.
(Tanaka and Chiba 2006)	MASINGAR 1.8^o x 1.8^o x 30 Online model but forced with external met fields	0.2-20	2100[a]	LAI data for GCM *(*Wilson and Henderson-Sellers, 1985*)*	Marticorena & Bergametti 1995 u_t increase due to soil moisture Fecan et al., 1999	Dry deposition In-cloud and below cloud scavenging	No
(Yue et al. 2009) On-line	GMOD in IAP9L-GCM 4^o x 5^o x 9	0.1-10	1935 ± 51[b]	Vegetation type predicted by the GCM.	Flux ~ u^3 u_t a function of particle size and relative humidity in the of the surface air	Dry deposition and below size dependant cloud scavenging	No

Table 1.5-1 Models for simulating the modern dust cycle. [a]emissions are calibrated to match observations. [b]emissions have not been calibrated to match observations. Where dry deposition is listed it corresponds to gravitational settling and turbulent mixing.

2 Dust model description

The new dust cycle model consists of three existing models. The first is the LPJ dynamic global vegetation model (Sitch et al. 2003). LPJ is used to predict the distribution of vegetation cover as it changes with varying climate and CO_2. Sparsely vegetated or bare ground regions are identified as potential dust sources. In addition to this, LPJ provides snow cover and soil moisture data which are used to suppress dust emissions.

The second model consists of a dust emission scheme. This model calculates dust emissions from the surface by saltation and sandblasting using the parameterisations developed by Marticorena and Bergametti (1995) and is based on a previous dust model (Tegen et al. 2002).

The third component of the dust model is the chemical transport model TOMCAT (Stockwell and Chipperfield 1999). This is used to transport the dust particles by advection, convection and diffusion. Dust is removed from the atmosphere by sub cloud scavenging and dry deposition. The sub cloud scavenging and dry deposition parameterisations are taken from the work of Lunt (2001) who also used TOMCAT to transport dust within the framework of a dust cycle model.

The three models are described in further detail in the following sections. Section 2.1 gives a background description of the LPJ model and the variables used to calculate dust source areas. Section 2.2 compares LPJ vegetation cover to remote sensing data to investigate whether LPJ can predict spatial and temporal changes in vegetation cover accurately. Section 2.3 describes how LPJ vegetation cover, soil moisture and snow depth are used to derive dust source areas. This is followed by a description of the model which calculates dust emissions in section 2.4. A description of how dust is transported and removed from the atmosphere is contained in section 2.5. Section 2.6 describes the steps taken to reduce the simulation time of the transport experiments. Finally the results of a baseline dust simulation are presented and discussed in section 2.7.

2.1 The Lund-Potsdam-Jena dynamic global vegetation model

The FORTRAN version of the LPJ source code used in this work was obtained from the Potsdam Institute for Climate Impact Research. LPJ simulates vegetation dynamics by

modelling the atmosphere-vegetation carbon and water fluxes, plant physiology, phenology, establishment and mortality. LPJ calculates daily gross primary production (GPP) by modelling the processes of photosynthesis and transpiration using a coupled photosynthesis and water balance scheme developed in the BIOME3 model (Haxeltine and Prentice 1996). A fraction of the GPP produced is used for the plant respiration. The remaining fraction which called the net primary production (NPP) is allocated to the leaf, sapwood and fine root carbon pools, satisfying a series of structural constraints.

Vegetation is grouped into ten plant functional types (PFTs) which are categorised according to their plant physiological (C3, C4 photosynthesis), phenological (deciduous, evergreen) and physiognomic (tree, grass) attributes. Plant mortality by fire, heat stress, competition for light and whether there is insufficient carbon to grow is modelled on an annual basis. Every year a proportion of the total vegetation cover decomposes and falls to the surface as litter and new vegetation is established. A set of bioclimatic limits are used to determine if a PFT can survive within a particular temperature range. Information on the bioclimatic limits has been collated from laboratory studies of plant behaviour under extremes of temperature.

LPJ is forced using annual mean CO_2 and monthly mean precipitation (mm), cloud cover (%) and temperature (^oC). The monthly climate data used to drive the model comes from the Climate Research Unit (CRU 2.1). The historical CO_2 data from 1901 to 1995 is obtained from the Carbon Cycle Model Linkage project on a 0.5 x 0.5 degree spatial resolution. The CRU 2.1 data is obtained for the years 1900 to 2002 at a spatial resolution of 0.5 x 0.5 degrees from the University of East Anglia, UK. The CRU data extends to the year 2006 but LPJ is only run until the year 2002. The reason for this is because the ERA-40 reanalysis data that is used to drive the dust emissions, transport and removal is only available until the year 2002.

Information on soil texture is taken from the Zobler soil map at a 0.5 x 0.5 degree spatial resolution. This is used to calculate the daily percolation of water from the upper soil layer to the lower soil layer. The LPJ simulation begins with no vegetation cover and is allowed to spin up for 1000 years so that the vegetation cover and carbon pools reach equilibrium. This is done by forcing the model with the first 30 years of the CRU climate repetitively for 1000 years. After this, the model is forced by 102 years of the CRU climate. The LPJ outputs used to calculate the dust source areas are:

1. Annual foliage projective cover (FPC):

The FPC is the overall fractional coverage of PFT in a grid cell. The FPC has a value of 1 if the grid cell is completely covered in vegetation or 0 if there is no vegetation cover present. The FPC is calculated by scaling up the FPC for each PFT using the following relationship.

$$FPC = CA.P.FPC_{ind} \qquad \text{Equation 2-1}$$

Where CA is the crown area and P is the population density of the PFT. The crown is calculated using an empirical relationship between crown area and stem diameter (Zeide, 1993). The FPC_{ind} is calculated using the following relationship (Monsi and Saeki, 1953)

$$FPC_{ind} = 1 - \exp(-0.5LAI_{ind}) \qquad \text{Equation 2-2}$$

Where LAI_{ind} is the leaf area index of the PFT which is related to the amount of carbon in the leaf.

2. Annual growing degree days base 5^oC

GDD_5 is calculated by taking the average of the daily maximum and minimum temperatures and subtracting this from the base temperature which is 5 °C

$$GDD_5 = \frac{T_{\max} - T_{\min}}{2} - 5^o C \qquad \text{Equation 2-3}$$

3. Annual tree height

The annual tree height is calculated using the empirical relationship between vegetation height and stem diameter (Huang et. al., 1992)

$$H = k_{allom2} D^{allom3} \qquad \text{Equation 2-4}$$

Where allom2 =40 and allom3=0.5 are constants and D is the diameter of the stem.

4. Monthly soil moisture in the upper 0.5m of the soil layer

The soil moisture in LPJ is calculated using a semi-empirical approach which was developed in the BIOME3 model (Haxeltine and Prentice 1996). The soil is divided into two layers of 0.5m each. The water held in each layer is calculated daily by taking into

account the precipitation, snowmelt, percolation, evapotranspiration and runoff. The percolation rate is dependent on the soil texture. When the soil layer is at field capacity the excess water is considered to be runoff. The soil water content of the upper layer on any given day is related to the amount of water into the soil layer plus the water out of the soil layer during the previous day.

$$sm = (melt + precip - perc - runoff - \beta_1 AET) / AWC_1 \quad \text{Equation 2-5}$$

Where *melt* is the snowmelt (mm), *precip* is the precipitation (mm), *runoff* is the runoff (mm) and β_1 is the rate of transpired water from the upper layer to the lower layer. AET is the calculated evapotranspiration rate for each plant functional type. AWC_1 is the available water holding capacity.

5. Monthly snow depth

LPJ calculates monthly snow depth using daily precipitation data which is derived from monthly precipitation that has been interpolated onto a daily time step. When the daily temperature is less than -2^{o}C, new snow is formed. The magnitude of the snow formed is proportional to the daily precipitation. An adjustment is made to the snow depth to account for the melting of snow. Snow melt occurs when the daily temperature is greater than -2^{o}C. The amount of melting is related to the temperature by snow melt coefficient taken from the BIOME3 model (Haxeltine and Prentice 1996).

6. Monthly Fraction of photosynthetically active radiation (FPAR)

The monthly FPAR predicted by LPJ gives an indication of the state and productivity of the vegetation cover. This quantity is defined as the fraction of incoming solar radiation absorbed by vegetation cover which is used to drive photosynthesis. It is calculated using the following relationship,

$$FPAR = FPC_{ind} D_{phen} \quad \text{Equation 2-6}$$

Where D_{phen} is the daily leaf-on fraction which is calculated from the GDD_5. If D_{phen} is 1 if the vegetation has leaf cover and 0 if it has no leaf cover.

2.2 Validating LPJ outputs used to calculate dust source areas

Studies have already been carried out to validate various outputs from the LPJ model. LPJ soil moisture has been validated against soil moisture observations for sites in regions with

Boreal, temperate and Mediterranean climates (Sitch et al. 2003). The soil moisture has been found to be in good agreement with measurements for different ecosystems with the exception of some sites in Russia where there is Boreal forest vegetation. This region is not a dust source so this will not have an impact on dust emissions.

The distribution of PFTs predicted by LPJ has also been validated against remote sensing observations from the AVHRR (Sitch et al. 2003). LPJ is broadly able to predict the latitudinal variation in PFT that is seen in the remote sensing data. LPJ correctly predicts the Boreal PFTs at high latitudes with a transition to temperate PFTs at lower latitudes and tropical PFTs at the Equator. Furthermore, LPJ does a reasonably good job at predicting distribution of C3 and C4 grasslands but has been found to overestimate the abundance of woody PFT in the African Sahel.

Validation work has been carried out to test how well LPJ predicts the density of vegetation cover. Schroder and Lucht (2003) compared LPJ FPAR to satellite based observations of FPAR from the AVHRR. They found that LPJ overestimated productivity in the Boreal and temperature forests as well as in tropical forest in Africa and South America.

A study by Seaquist et al. (2009) tested the ability of LPJ to predict the inter-annual viability in vegetation cover over the Sahel. They compared the annual maximum leaf area index from LPJ to annual maximum NDVI from the AVHRR. It was found LPJ was able to predict the inter-annual variability in vegetation cover aggregated over the Sahel for the years 1982-2002. Regionally, LPJ predicted the inter-annual variability well in Northern Senegal, Southern Mauritania Central Mali, Western Niger, Sudan and in Eretria. They found strong disagreement in North Niger, with smaller areas of disagreement in South West Mali and Ethiopia which could not be explained by changes in agriculture practices or in the population density. It is significant that LPJ is able to predict the inter-annual variability in vegetation cover in most of the Sahel because the expansion and contraction of this region affects the size of the Sahara. In chapter 5 it is investigated whether an expansion of the Sahara can account for the four fold increase in dust concentrations measured at Barbados during the 1980s relative to the 1960s (Prospero and Nees 1986).

For his study, we are interested in whether LPJ can predict the vegetation distribution and temporal variability in vegetation dynamics in semi-arid regions as this will have an impact

on dust emissions. The timing of the minimum vegetation cover and the length of the time when the vegetation cover is below a threshold limit will determine the timing and length of the dust emitting season. A validation of this type has not been reported in the literature; therefore, it is necessary to carry this out. To test how well the LPJ model predicts the temporal variability in vegetation dynamics, the simulated monthly FPAR is compared to FPAR derived from remote sensing data.

2.2.1 Evaluation of simulated and observed FPAR

Monitoring the distribution and evolution of vegetation cover from space commonly involved using the Normalized Difference Vegetation Index (NDVI) (James 1995). This measurement is based on the fact that plants absorb radiation in the red wavelength and reflects in the near infra-red. The NDVI is a measure of the difference in reflectance between the red wavelength (0.58-0.68μm) and the near infra-red wavelength (0.72-1.10μm). NDVI observations are sensitive to several factors such as changes in soil colour, atmospheric perturbations and to the geometry of illumination.

As an alternative to NDVI, FPAR data from the Sea-viewing Wide Field-of-view Sensor (SeaWiFS) is used to validate LPJ. The SeaWiFS sensor takes measurements in the blue spectral band which is sensitive to aerosol loading. This measurement technique results in improved data quality when compared to NDVI data. This is because perturbations by aerosols can be corrected for.

The quality of the SeaWiFS data has been evaluated by Gobron et al. (2006). It was shown that the SeaWiFS FPAR responded to particular events such as the 2003 heat wave and the 2002 fires in Oregon. In the same paper, the SeaWiFS data was validated against surface estimates of FPAR at specific sites by measuring the radiation above and below the canopy in the photosynthetically active wavelength range. There was good agreement between the surface estimate of FPAR and the SeaWiFS FPAR with the exception of data at high latitudes where the SeaWiFS data was shown to be unreliable. This is due to errors in measurements made at low solar zenith angles. In addition, snow cover and nearly continuous cloud cover also contribute to the uncertainty in the data at high latitudes. The most northerly point at which the SeaWiFS FPAR data has been validated against surface observations of FPAR is 48^{o}N. When comparing the LPJ FPAR to the SeaWiFS FPAR, the data north of 48^{o}N may not be accurate. The monthly composite FPAR from SeaWiFS is

downloaded from the website: http://fapar.jrc.it/Home.php for the period 1998 to 2002 and used in the following section.

Figure 2-1 shows a comparison between the LPJ simulated monthly mean FPAR and measured FPAR averaged over the years 1998 to 2002. The figure shows that there is a systematic overestimate in the simulated FPAR compared to the SeaWiFS FPAR. This is particularly apparent in regions with a high density of vegetation such as the Boreal forest in Canada and Eurasia and the tropical forest regions. A similar finding was reported by Schroder and Lucht (2003) who compared LPJ FPAR to FPAR derived from the AVHRR. This discrepancy will have no impact on dust emissions because these regions will never have sparse enough vegetation cover to act as dust sources. Both the model and the observations show low productivity in the main arid and semi arid regions and at high latitudes.

The location of sparsely vegetated regions in North Africa, the Arabian Peninsula and Asia, Australia, North and South America are prominent in both the modelled data and the observations. LPJ over predicts the density of vegetation cover in Australia compared to the SeaWiFS data. This is the first indication that LPJ may not simulate the vegetation dynamics correctly in Australia. It will be shown in section 2.2.2 that LPJ is also unable to predict the seasonality in vegetation cover in Australia. This has implications for estimating dust emissions from Australia.

It is worth noting that an exact match between the remote sensing and modelled FPAR is not possible because the remote sensing data contains cultivated land, while the LPJ data represents vegetation in its natural state. This aside, the model does a reasonably good job at predicting low FPAR values in the major desert and semi-arid regions.

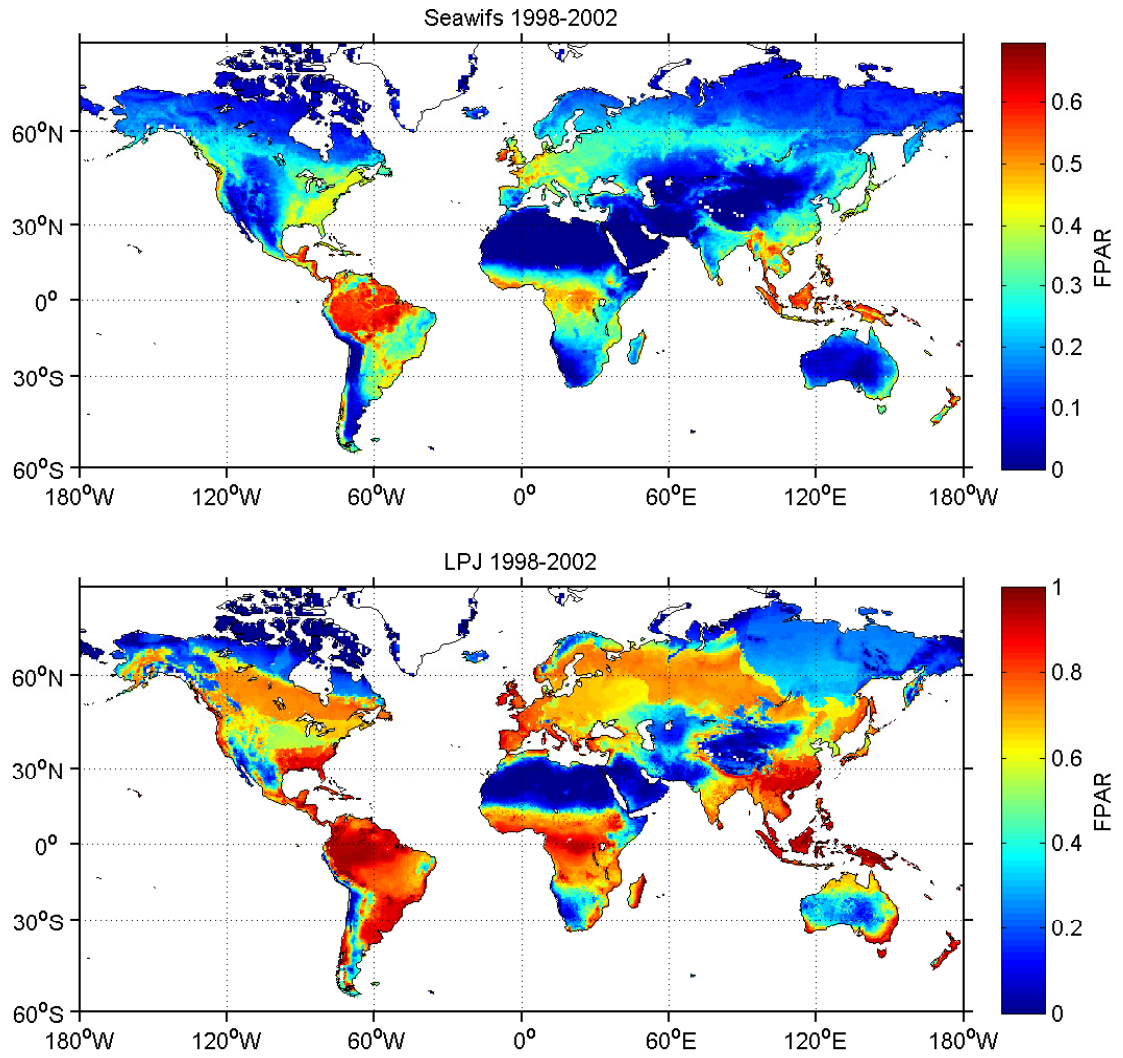

Figure 2-1 Comparison between the simulated annual mean FPAR from LPJ with annual mean FPAR from the SeaWiFS sensor. The LPJ simulation has been driven by CRU 2.1 climate data.

2.2.2 Evaluation of simulated and observed seasonality in FPAR

This section examines how well LPJ predicts seasonal changes in vegetation cover compared to the remote sensing data. As mentioned in the previous section LPJ systematically overestimates FPAR compared to the SeaWiFS data. To compare the two datasets the SeaWiFS FPAR is scaled so that the annual mean FPAR over the years 1998-2000 over all grid boxes equals the annual mean FPAR from LPJ over the same years over all grid boxes. The SeaWiFS data is scaled by multiplying the data by a factor of 2.3669.

Figure 2-2 shows the number of months when the FPAR is below 0.5 for the LPJ data and SeaWiFS data. This gives an indication of the length of time a particular region is a potential dust source. The threshold value of 0.5 is somewhat arbitrary and chosen on the basis that dust emissions will not occur when a grid box is more than half covered with vegetation. The FPAR threshold will be tuned later in Chapter 3.

The model and the observations show that the key desert regions emit dust all year round. At the boundary of some of theses regions dust is emitted for part of the year. There is reasonable agreement between the model and the SeaWiFS data in South America, South Africa, Northern India and Australia. There is notable difference in North America and in Central Asia (north of the Caspian Sea). The discrepancy is likely to be caused by a difference in the vegetation type predicted by LPJ and the actual vegetation type. This is further complicated by the fact that the vegetation cover may be modified by land use.

Figure 2-3 shows the month when the vegetation is at a minimum for both LPJ and SeaWiFS data. In Asia the vegetation cover has a minimum in January which agrees with the SeaWiFS data. This can be explained by cold winter temperatures which cause the die back of C3 grasses in this region. The dominant plant function types predicted by LPJ are shown in Figure 2-4.

In the Sahel region, LPJ correctly predicts the timing of the minimum FPAR in April-May. The climate of the Sahel is characterised as having a long dry season lasting from October to May followed by a wet winter season from June to September. The minimum vegetation cover coincides approximately with the end of the hot dry season where the vegetation has been exposed to an extended period without rainfall.

In Northern India Figure 2-3 shows that the timing of the minimum vegetation cover occurs in May in the observations, but slightly early in April in the LPJ data. This comes at the end of the dry season (March to May) when temperatures are at the highest.

There are notable differences between the timing of the minimum vegetation cover in Australia, North America and in South Africa. In Australia the minimum vegetation cover in the SeaWiFS data is observed from November to January, which coincides with the Southern Hemisphere summer. The onset of the minimum occurs slightly earlier in the LPJ

data between August-September. This time difference may have implications for predicting seasonal emissions in dust from Australia.

The reason for the difference in timing may be because LPJ represents vegetation cover in Australia in an over simplistic way. Figure 2-5 shows vegetation types from the Mathews vegetation map (Matthews 1983). This is a map of vegetation types compiled from existing maps of vegetation and remote sensing data. The Matthews vegetation map shows that Australia contains desert, xeromorphic shrubland and tall/medium/short grass with shrub cover. In contrast LPJ simply predicts C3 grasses. Indeed LPJ does not simulate shrub PFTs.

In the interior of South Africa, LPJ predicts minimum vegetation cover between June and August. This is also seen in the SeaWiFS in Figure 2-3. This coincides with the driest months in this region. LPJ is unable to predict the timing of the minimum vegetation in the northern South Africa and on the costal regions. The Matthews vegetation map shows the presence of xeromorphic shrubland, however, LPJ predicts C3 grasses and desert.

In South America LPJ is successful at predicting the timing of the minimum vegetation cover Patagonia in June-July-August. These are the months when temperatures are lowest in Patagonia. Differences are seen between the SeaWiFS data and the LPJ data further north in the Peruvian desert. LPJ predicts the minimum vegetation cover in June-July-August while the SeaWiFS data predicts minimum vegetation slightly later in September-October.

2.2.3 Evaluation of simulated and observed inter-annual variability in FPAR

This section explores if LPJ can simulate the expansion and contraction of sparsely vegetated regions on inter-annual time scales. A comparison is made with SeaWiFS data again. The standard deviation FPAR <0.5 over the years 1998 to 2002 can be seen in Figure 2-6. Values of zero correspond with regions that do not vary from year to year or are not a dust source.

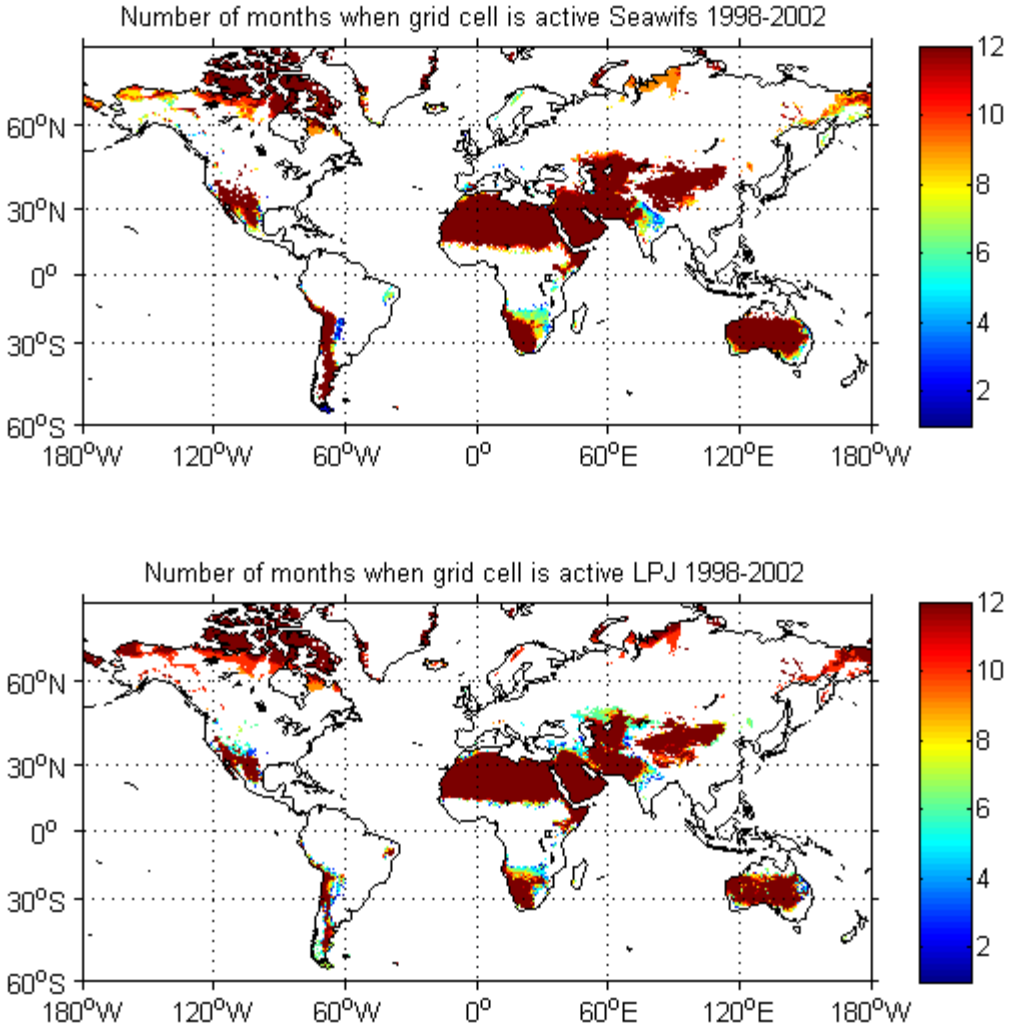

Figure 2-2 The number of months when the FPAR is less then 0.5. The SeaWiFS data has been scaled by multiplying by a factor of 2.3669. Grid boxes where LPJ predicts trees are excluded in both plots.

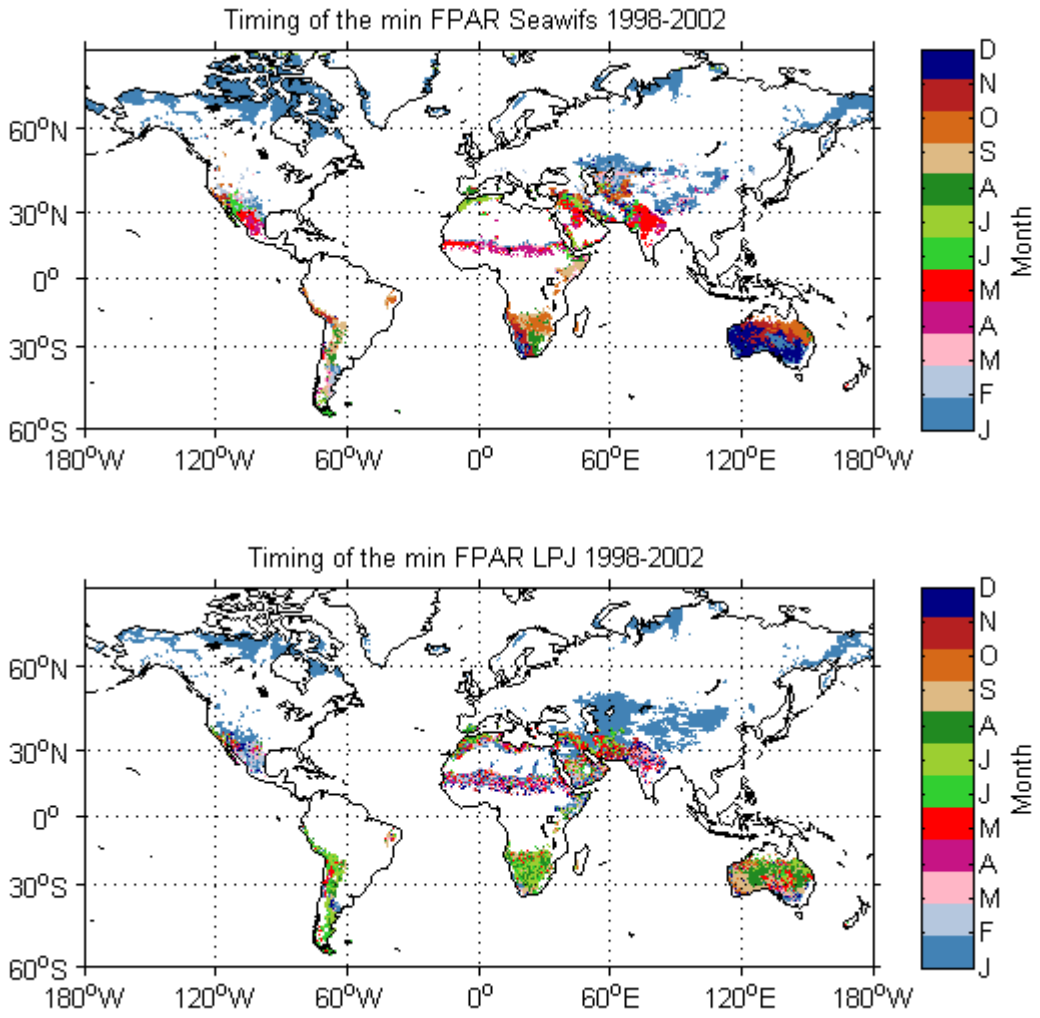

Figure 2-3 The timing of the minimum vegetation cover from the LPJ FPAR data and the SeaWiFS FPAR. Grid boxes where LPJ predicts trees are excluded in both plots.

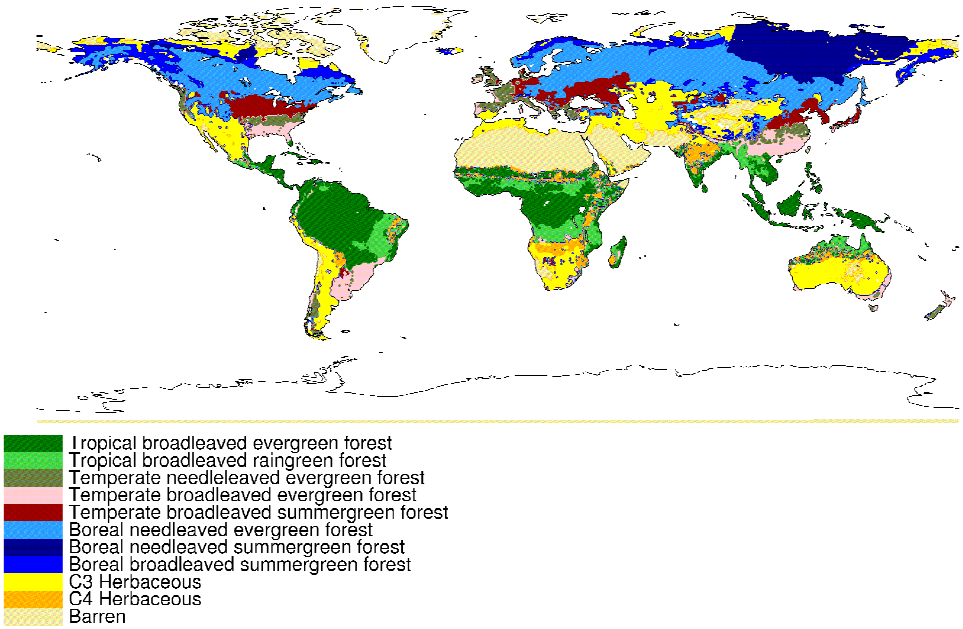

Figure 2-4 The dominant plant function type simulated by LPJ. The simulation has been driven with CRU 2.1 climate data. The FPC is averaged for the years 1998 to 2002

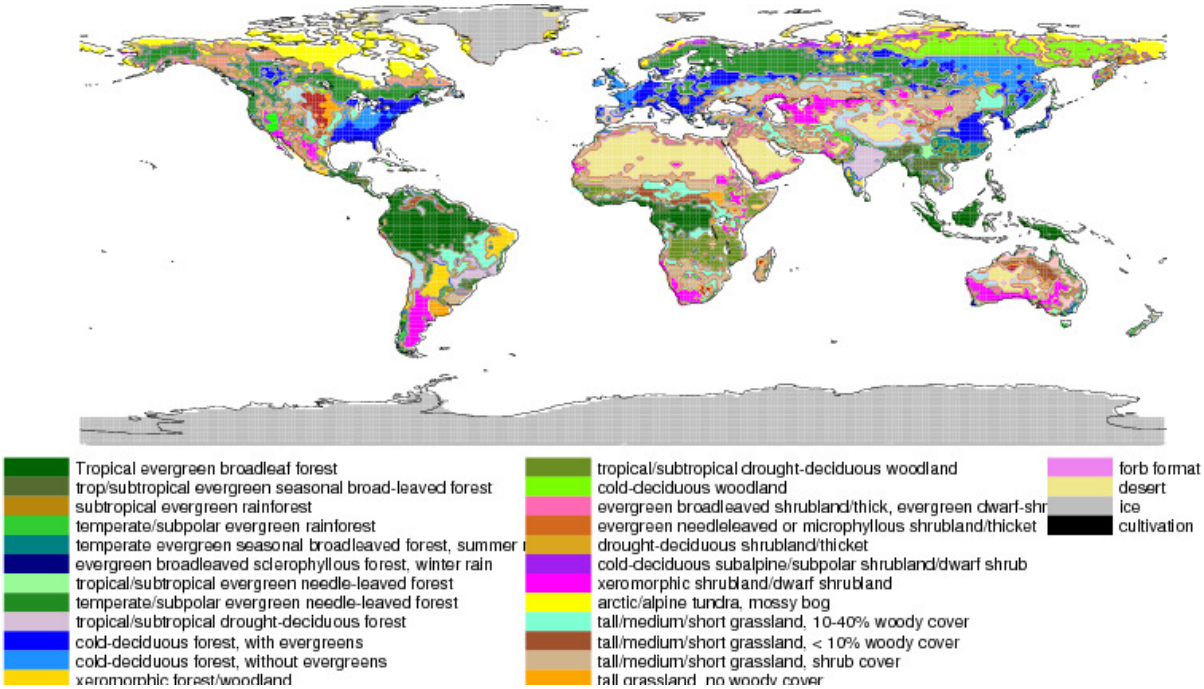

Figure 2-5 Vegetation type from the Matthews vegetation map (Matthews 1983)

Inter-annual variability is seen at the boundaries of the arid and semi-arid regions in both the LPJ data and the SeaWiFS data. The maximum standard deviation in FPAR is similar in both datasets (0.25). LPJ predicts more extensive inter-annual variability in Asia, North America, South America, South Africa and in Australia than the SeaWiFS data. This is likely to be caused by an over simplification of the vegetation type predicted by LPJ. LPJ simulates C3 grasses in these regions (Figure 2-4) while the Matthews vegetation map shows that these regions contain xeromorphic shrubland and a mixture of tall/medium/short grass with shrub cover (Figure 2-5).

In the Sahel, the inter-annual variability in LPJ FPAR has been validated by Seaquist et al. (2009). Good agreement was found between the years 1982-2002 with remote sensing NDVI as was mentioned in section 2.2.

2.3 Using LPJ to calculate dust source areas

This section describes how LPJ outputs are used to calculate dust source areas. The first step is to convert LPJ PFTs into biomes. A biome map is constructed every year from the annual mean GDD_5, tree height and FPC (Joos et al. 2004). If the GDD_5 is less than 500^{o}C day then tundra vegetation is present. When the GDD_5 is greater than 500^{o}C day dry grass, dry shrubland and dry woodland biomes are present. Tree biomes occur when the tree height is greater than 10 m. Short trees with a height of less than 4 m area assumed to be shrubs. This assumption is made because LPJ does not simulate shrub plant functional types. A map of the biomes can be seen in Figure 2-7.

It could be argued that converting PFT into biomes is an unnecessary intermediate step and that the dust source areas could be simply be calculated directly using FPC or FPAR. This was explored but it was found that using FPC or FPAR lead to a very large source area in the Canadian Arctic. This is caused because LPJ predicts barren land combined with low soil moisture and low snow cover which is the criteria for a dust source. In reality this is a permafrost region. Using the scheme developed by Joos et al., (2004) allows polar desert, which has low GDD_5 and is not a dust source, to be distinguished from a hot desert which has high GDD_5 and is a dust source.

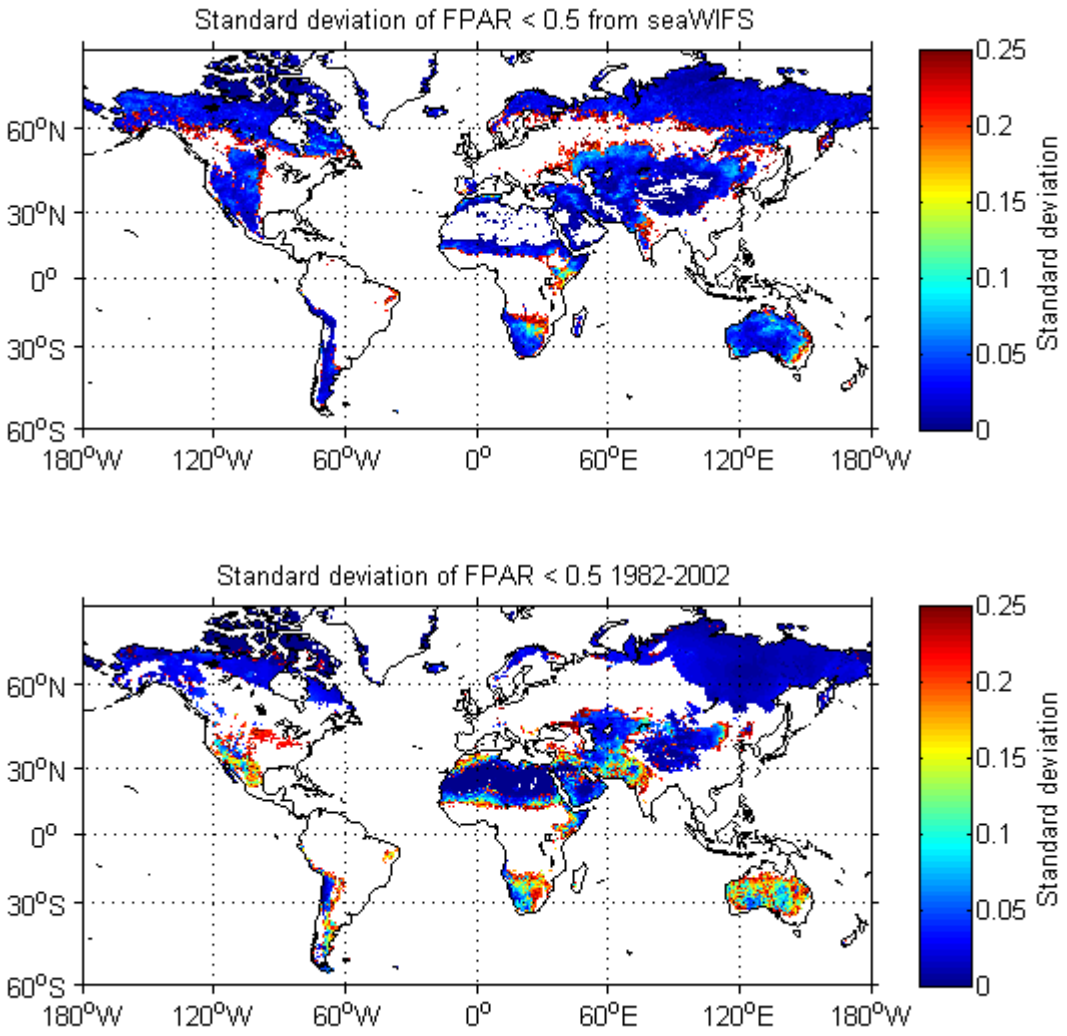

Figure 2-6 Comparison between the inter-annual variability in FPAR < 0.5 from SeaWiFS and LPJ data

For grass-dominated biomes (tundra grass and dry grass) the area exposed for dust emission varies seasonally. A_{veg} is linearly proportional to the FPAR below a threshold value $FPAR_{lim}$.

$$\left\{ A_{veg} = 1 - \frac{fpar}{fpar_{\lim}} \right\} \quad \text{for fpar} < \text{fpar}_{\lim} \text{ otherwise } A_{veg}=0 \qquad \text{Equation 2-7}$$

Shrub dominated biomes are treated differently to grass dominated biomes. Shrubs are assumed to protect the surface all years round even when no leaves are present. The annual maximum FPAR ($FPAR_{max}$) is used as an index for the density of shrubs. For shrub dominated biomes, the area is calculated as

$$A_{veg} = 1 - fpar_{\max}$$ Equation 2-8

This means the dust source area remains constant throughout the year but decreases to zero when the ($FPAR_{max}$) =1.

At high latitudes, dust emission is suppressed by snow cover. In the winter, high latitude regions are completely covered in snow. This melts as the summer time commences, exposing the surface to erosion. Snow cover, therefore, has a seasonal impact on dust emissions. The seasonal change is snow depth can be seen in Figure 2-8. The area exposed for dust emission is related to the LPJ snow depth value below a threshold value (sd_{lim}).

$$A_{snow} = 1 - \frac{sd}{sd_{\lim}}$$ Equation 2-9

Dust emissions are only permitted when the soil moisture is below a threshold value. The total area available for dust emission is related to area of dry ground that is not covered by vegetation or snow. The erodible areal fraction A_{bare} is expressed by the following factorial form

$$A_{bare} = (A_{veg})(A_{snow}).I_{\theta}$$ Equation 2-10

Where A_{veg} is the contribution of exposed ground from vegetation cover, A_{snow} is contribution from snow cover and I_θ is the soil moisture. When the soil moisture is above a threshold limit (sm_{lim}) then I_θ has a value of 0 and there is no dust emission. On the other hand, if the soil moisture is below sm_{lim} then I_θ has a value of 1 and dust emission will occur. This is the same approach taken by Tegen et al., (2002) to switch dust emissions on or off. Figure 2-9 shows a plot of the simulated annual mean soil moisture. The $FPAR_{lim}$, sm_{lim} and the sd_{lim} are tuneable parameters. In Chapter 3 a tuning exercise is carried out to determine the best values for these threshold limits.

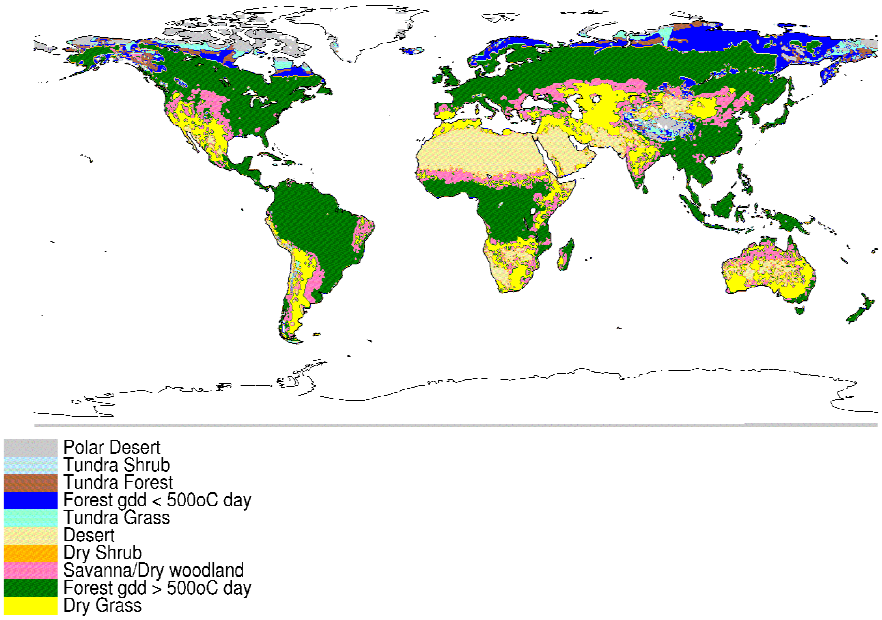

Figure 2-7 A biome map constructed from LPJ output using foliage projective cover, growing degree and tree height using the scheme described in Joos et al., (2004)

2.4 The dust flux calculation

This section describes the dust emission model which is used in this work. The scheme comes from the work of Tegen et al., (2002) and the code was provided by Ina Tegen. The calculation of the dust is based on the work of (Marticorena and Bergametti 1995). The horizontal flux G_j is generated by saltating particles. This is calculated as

$$G_j = \frac{\rho_a}{g} u^{*3} (1 + \frac{u_t^*}{u^*})(1 - \frac{u_t^{*2}}{u_2^*}).s_j \qquad \text{Equation 2-11}$$

where ρ_a is the density of air (kgm^{-3}), g is the gravitational constant (ms^{-1}), $u*$ is the surface wind velocity (ms^{-1}) and u^*_t is the threshold friction velocity (ms^{-1}). s_j is the relative surface area covered by each size fraction j.

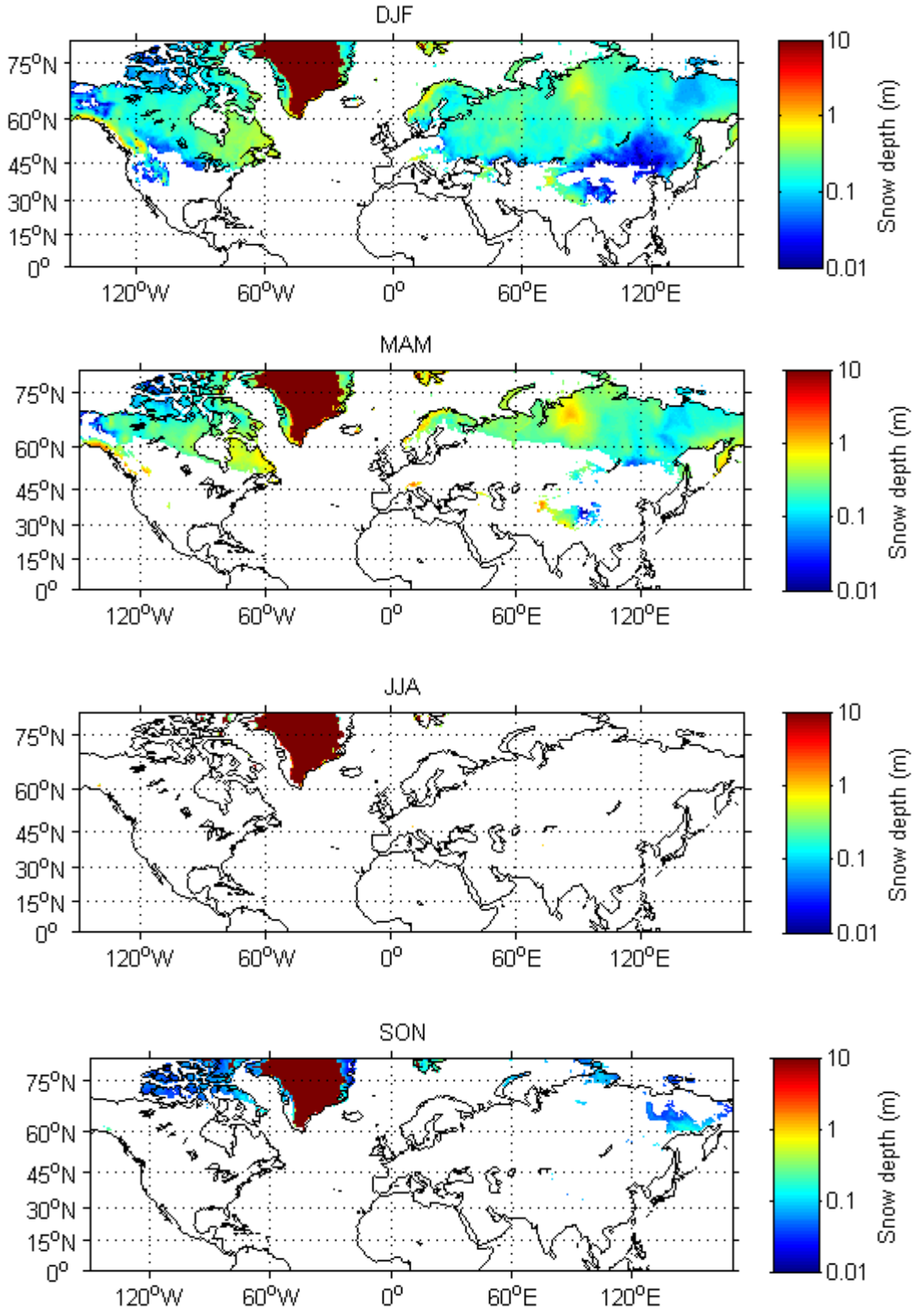

Figure 2-8 Seasonal variability in simulated snow depth data from LPJ for the year 1987

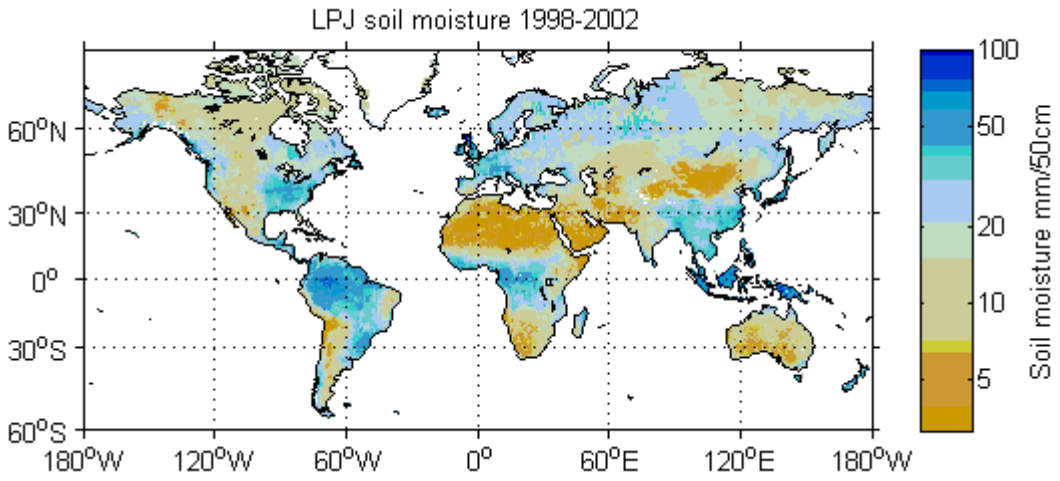

Figure 2-9 Monthly mean soil moisture simulated by LPJ for the top 0.5 m soil layer.

u^*_t is calculated as a function of particle diameter using a semi-empirical relationship described by Iversen and White (1982). The relationship between u^*_t and the particle diameter is shown in Figure 1-1. u^*_t is modified to account for the presence of non-erodible elements such as vegetation cover or rocks which reduces the wind speed momentum. u^*_t is modified by dividing by the drag partition ratio f_{eff} which is a function of the surface roughness (Marticorena and Bergametti 1995)

$$f_{eff} = 1 - \left[\frac{\ln\left(\frac{z_0}{z_{0s}}\right)}{\ln\left(0.35\left(\frac{10}{z_{0s}}\right)^{0.8}\right)} \right] \qquad \text{Equation 2-12}$$

where roughness length of a surface with no obstacles z_{0s}=0.001cm. The roughness length of the z_0=0.01cm is used which is typical value for level desert (Seinfeld 1998).

In the Tegen et al., (2002) model the u^*_t for each particle size is reduced by a factor of 0.66. This value was found to give the best results with dust storm frequency data and dust deposition rates in Florida. This scaling factor will be tuned in chapter 3.

The dust flux is calculated on a six hourly time step using ERA-40 10 m wind speeds at a 1^o x 1^o resolution. The wind speeds are interpolated to a 0.5 x 0.5 degree resolution by assuming that four adjoining half degree pixels have the same wind speed as a 1^o degree

pixel. The 10m wind speeds are modified to give the friction velocity as a function of surface roughness, such that

$$u^* = \frac{u}{k}\ln(\frac{z}{z_0}) \qquad \text{Equation 2-13}$$

where k is the Von Karman constant=0.4 (dimensionless), z is the height (m), z_0 is the roughness length (m) and u (ms^{-1}) is the ERA-40 10 m wind speeds.

The vertical flux is related to the horizontal flux by the sandblasting mass efficiency α. The α values used in the model are taken from Marticorena et al., (1997) who summarise the experimental values for different soil types. These are listed in Table 2-1

Table 2-1. α values are large for soils containing silt and small for soils containing sand. The α value for soil with a high clay content is reduced to account for the strong inter-particle cohesion forces which make the soil less erodible.

The vertical flux F is estimated from the horizontal flux by the following

$$F = A_{bare}\alpha G \qquad \text{Equation 2-14}$$

where G is the vertical flux from Equation 2-11. A_{bare} is the area of bare ground available for dust emission which has been calculated from LPJ data in Equation 2-10.

2.4.1 Soil texture and particle size distribution

The treatment of the particle size distribution in the Tegen et al., (2002) model is based on the work of Marticorena and Bergametti (1995). The size of particles entrained into the atmosphere is dependent on the soil texture at the surface. The soil texture information is taken from the Soil Food and Agriculture Organization United Nations Educational, Scientific and Cultural Organization soil map of the world (Zobler 1986). This is a map of soil texture in the top 30cm of the soil on a 0.5 x 0.5 degree grid. The standard soil textural triangle is used to derive the relative abundance of the 4 main soil types; clay, silt, medium/fine sand and coarse sand for each soil texture. The percentage mass of each fraction is listed in

Table 2-1. It can be seen that the fine grain soil texture contains a high proportion of silt and clay. In contrast, the coarse soil texture predominately contains coarse sand and medium sand. The particle mass distribution for each soil texture type is calculated using the following equation

$$\frac{dM(D_p)}{d\ln(D_p)} = \sum_{j=1}^{n} \frac{M_j}{(2\pi)^{\frac{1}{2}} \ln\sigma_j} \exp\left(\frac{(\ln D_p - \ln MMD_j)}{-2\ln^2 \sigma_j} \right) \quad \text{Equation 2-15}$$

D_p is the particle size, M_j is the percentage mass of coarse sand, medium/fine sand, silt or clay listed in Table 2-1. MMD_j is the mass median diameter. The mass median diameter is 710μm for coarse sand, 160μm for medium/fine sand and 15μm for silt. σ_j is the geometric standard deviation which has a value of 2 for all the soil types.

The six hourly surface emissions are calculated for the 8 particle size bins on a 0.5 x 0.5 degree spatial resolution. The limits of the size classes are 0.1μm, 0.3μm, 0.9μm, 2.6μm, 8μm, 24μm, 72μm and 220μm. The emissions are re-gridded onto a T42 spatial resolution grid for input into the chemical transport model which is described next.

Soil texture classes	α cm^{-1}	Coarse	Medium/ Fine Sand	Silt	Clay
Coarse	$2.1x10^{-6}$	0.43	0.4	0.17	-
Medium	$4.0x10^{-6}$	-	0.37	0.33	0.3
Fine	$1.0x10^{-7}$	-	-	0.33	0.67
Coarse-Medium	$2.7x10^{-6}$	0.1	0.5	0.2	0.20
Coarse-Fine	$2.8x10^{-6}$	-	0.5	0.12	0.38
Medium-Fine	$1.0x10^{-7}$	-	0.27	0.27	0.48
Coarse-Medium-Fine	$2.5x10^{-6}$	0.23	0.23	0.19	0.35
Organic	-	0.25	0.25	0.25	0.25

Table 2-1 Soil parameters used to calculate the particle size distribution. Column 1 contains the sandblasting mass efficiency values for the different soil textures. Columns 2, 3, and 4 contain the relative mass of the main soil types for each of the Zobler soil textures which are used to calculate the particle size distribution.

2.5 Dust transport and removal

The chemical transport model TOMCAT is used to transport dust in the atmosphere. TOMCAT is an off-line three-dimensional chemical transport model (Stockwell and Chipperfield 1999). TOMCAT was initially developed to model stratospheric chemistry but has been extended to model chemistry in the troposphere. TOMCAT is driven by 3-D wind speeds, specific humidity and temperature which can be derived from either meteorological re-analysis data or GCM output. TOMCAT simulates the transport of gaseous or aerosol species via advection, convection and vertical diffusion. For this application it is assumed that dust does not interact with other species in the atmosphere. Therefore, TOMCAT is run with the chemistry modules switched off.

The horizontal and vertical resolution of TOMCAT depends on the spatial resolution of the input meteorological data. The ERA-40 reanalysis data used to drive TOMCAT has a T42 spatial resolution. This corresponds to 64 latitude points and 128 longitude points. There are 31 vertical pressure levels extending from the surface to the stratosphere. The model has a dynamical time step that can be specified. For the dust simulations the model time step is one hour.

The advection scheme used in TOMCAT is the conservation of second order moments developed by Prather (1986). This scheme models the transport of tracer between grid boxes in the x, y and z directions by numerically solving the advection equation

$$\partial \frac{\partial(r\rho)}{\partial t} + \nabla.(ur\rho) = 0 \qquad \text{Equation 2-16}$$

where r is the mass mixing ratio of tracer ($kgkg^{-1}$), ρ is the local density of air (kgm^{-3}), and u is the wind velocity (ms^{-1}) which has components in the x, y and z direction taken from metrological data.

The Prather advection scheme is a modifaction of an upstream advection scheme. An upstream scheme calculates the tracer flux into a grid box, as the tracer concentration in the 'up-wind' grid box multiplied by the wind velocity at the interface of the two grid boxes, multipled by the model time step. The Prather advection scheme is a modification of the slope scheme Russell and Lerner (1981). The slope scheme calculates the linear distribution of the tracer concentration at every grid box, every model time step. The

Prather scheme extends this by calculating a curve to represent the tracer distribution in a grid box, every model time step.

This makes the Prather advection scheme more computentially expensive than the slopes scheme. Prather (1986) found that it took 1.5 times longer to run the Prather advection scheme than the sclope scheme. However, it has been shown that the Prather scheme performs better than other advection schemes. Ge and Lei (1998) compared the Prather advection schemes to an anti-diffusion Smolarkiewicz scheme in a region transport model. It was shown that numerical diffusion in the Prather scheme was one order of magnitude less than the anti-diffusion Smolarkiewicz scheme, thus providing better results.

Convection is parameterised in TOMCAT using a scheme by developed by Teidkte (1998). This scheme has been modified in TOMCAT. Details of the modifications are described in Stockwell and Chipperfield (1999). The scheme includes cumulus updrafts in the vertical direction and the exchange of air from inside the cloud to outside the cloud and vice versa. The convective scheme calculates the mass of tracer that is uplifted within a cloud column. The scheme requires 3 dimensional temperature and humidity data which is obtained from ERA-40 reanalysis data.

Vertical diffusion is parameterised in TOMCAT using a scheme developed by Louis (1979). This scheme is described in further detail in Stockwell and Chipperfield (1999). The vertical diffusion scheme does not account for large-eddy transports that can occur throughout the planetary boundary layer (PBL) and or for entrainment at the top of the PBL. This means that mixing both within the PBL itself and between the PBL and the lowermost free troposphere will be underestimated in TOMCAT (Stockwell and Chipperfield 1999).

2.5.1 Dry deposition

Particles are removed from the dust model by wet and dry deposition. Dry deposition is the transport of particles from the atmosphere to the surface in the absence of precipitation. It is parameterised in the model by representing two physical processes. The first process is the gravitational settling of a particle from the atmosphere to the quasi laminar sub layer. This is a thin layer of air at the surface which is stationary. The second process is the

transport of the particle across the quasi laminar sub layer where it finally adheres to the surface. The dry deposition parameterisation is taken from Lunt (2001) which is based on equations for dry deposition described in Seinfeld (1998).

The rate at which a particle is removed by dry deposition per unit area per unit time F_z is proportional to the concentration of dust at a particular height C_z and to the deposition velocity v_s by the following relationship.

$$F_z = v_d C_z \qquad \text{Equation 2-17}$$

The dry deposition process is often conceptualised in terms of an electric circuit containing resistance in series. r_a is the aerodynamic resistance and r_b is the quasi laminar sub layer resistance. The total v_d is then

$$v_d = v_s + \frac{1}{r_a + r_b + r_a r_b v_s} \qquad \text{Equation 2-18}$$

The first expression of the equation corresponds to the gravitational settling velocity (v_s). The second expression corresponds to the deposition velocity across the quasi laminar sub layer. An explanation of how r_b is calculated is contained in section 2.5.1.2.

2.5.1.1 Gravitational Settling

During a particle's descent to the surface, it experiences an aerodynamic resistance in the opposite direction to its path. The magnitude of the aerodynamic resistance is proportional the particle size. The opposing forces of gravity and aerodynamic resistance can be equated using Newton's second law of motion. This is a first order partial differential equation that can be solved for v_s to give

$$v_s = \frac{\rho_p D_p^2 g C_c}{18\mu} \qquad \text{Equation 2-19}$$

Where ρ_p is the density of the particle (kgm^{-3}), D_p is the particle diameter (m), g is gravitational constant (ms^{-2}), μ is the viscosity of air ($kgm^{-1}s^{-1}$) and C_c is the slip correction factor. This relationship is known as Stokes Law.

When the particle diameter approaches the same magnitude as the mean free path of the medium then the medium no longer acts a continuum and Stokes law overestimates the value of v_s. A correction is made for this using the slip correction factor C_c. The slip correction factor is given by

$$C_c = 1 + \frac{2\lambda}{D_p}(1.257 + 0.4e^{\frac{-0.55D_p}{\lambda}}) \qquad \text{Equation 2-20}$$

Where λ is the mean free path of the particle.

Dust is transported downwards by gravitational settling through each model vertical level with the exception of the lowest level. A simplification is made in which particles are prohibited from falling through multiple vertical levels within one time step (1hour). At high altitudes the distance between vertical levels is large so this assumption should not have any significant impact. In addition to this, large particles do not reach high altitudes.

2.5.1.2 Transport across the sub laminar layer

To reach the surface, dust particles must cross the quasi sub laminar layer. Dust is transported across this layer by three processes; Brownian motion, internal impaction and interception with the surface. Brownian motion is the random movement of particles, some of which will hit the surface. Inertial impaction is when the particles hit the surface because of their momentum. The total resistance experienced by a particle will depend on the combination of these processes. For very small particles Brownian motion is the predominant means of transport across the layer.

The resistance of the quasi sub laminar layer in Equation 2-18 is defined as

$$r_b = \frac{1}{u_*(Sc^{\frac{-2}{3}} + 10^{\frac{-3}{St}})} \qquad \text{Equation 2-21}$$

Where Sc is the Schmidt number which accounts for Brownian motion of very small particles. The Schmid number Sc is calculated as Sc=υ/D, υ is the kinematic viscosity of

air and D is the molecular diffusivity. St is the Stokes number which accounts for inertial impaction for larger size particles. u_* is the surface wind speed which comes from ERA-40 reanalysis data. This approach is identical to the work of Lunt (2001) and Lunt and Valdes (2002). A diagram of the dry deposition processes can be seen in Figure 2-10

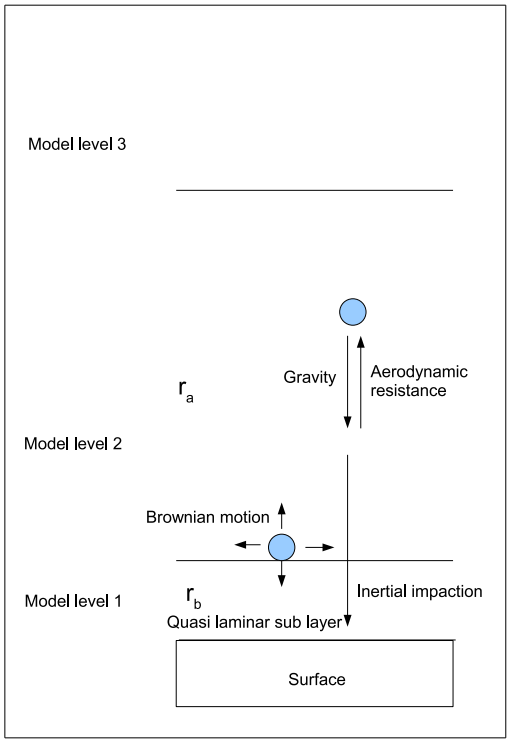

Figure 2-10 A schematic of the processes of gravitational settling and transport across the sub laminar layer which takes place at every model time step.

2.5.2 Wet Deposition

Dust is removed from the atmosphere by the process of sub-cloud scavenging. This takes place every hour in the model. The amount of mass removed is proportional to the precipitation rate by a factor called the scavenging coefficient such that,

$$C_t = C_0 e^{\Lambda t} \qquad \text{Equation 2-22}$$

C_0 is the initial tracer mass and t is the model time step and Λ is the scavenging coefficient which has units of s^{-1} (Seinfeld 1998).

Dust is removed by two types of precipitation in the model

1. Large scale precipitation
2. Convective precipitation

To calculate the amount of dust removed by sub-cloud scavenging, the vertical precipitation rate p_z is required. 3d precipitation fields are generally not archived by ECMWF or GCMs; however, surface precipitation data is available. The vertical precipitation profile is derived from the surface precipitation by assuming a vertical cloud structure for convective and stratisform cloud. Fractional low and medium cloud cover data is used to do this. This approach is taken from Lunt (2001) who also used TOMCAT to transport dust in a dust cycle model. The units of the fractional cloud cover vary from 0-1 where 1 represents complete cloud cover.

Convective cloud is assumed to have a base at 90% of the surface pressure and extends all the way to the tropopause. The precipitation is zero at the top of the cloud and varies linearly to the base of the cloud where it has the same value as the surface precipitation. Beneath the cloud base the precipitation rate is the same as the surface.

Stratisform clouds have a different profile. The cloud is divided into an upper and a lower part. The cloud base is at 90% of surface pressure, cloud middle is at 80% and cloud top is at 50%. The precipitation varies linearly from the base of the cloud to a point x in the middle of the cloud. The value of x depends on the medium and low cloud amounts, and is given by

$$x = p_0 \frac{A_{med}}{A_{med} + A_{low}} \qquad \text{Equation 2-23}$$

A_{med} and A_{low} is the fractional coverage of the low and medium cloud cover and p_0 is the surface precipitation rate. The precipitation varies linearly again from the point x to the top of the cloud where it has a value of zero. A diagram of the precipitation profile can be seen in Figure 2-11.

The scavenging coefficient used in the model is taken from the work of Brandt et al., (2002). In this parameterisation the scavenging coefficient is independent of the particle size and is proportional to the precipitation rate such that

$$\Lambda = AP^{B}$$

Equation 2-24

where A=8.4 x 10^{-5} and B=0.79 for both convective and large scale precipitation. The units of precipitation are in $mmhr^{-1}$. In chapter 3 the effect of using a size dependent scavenging coefficient is tested.

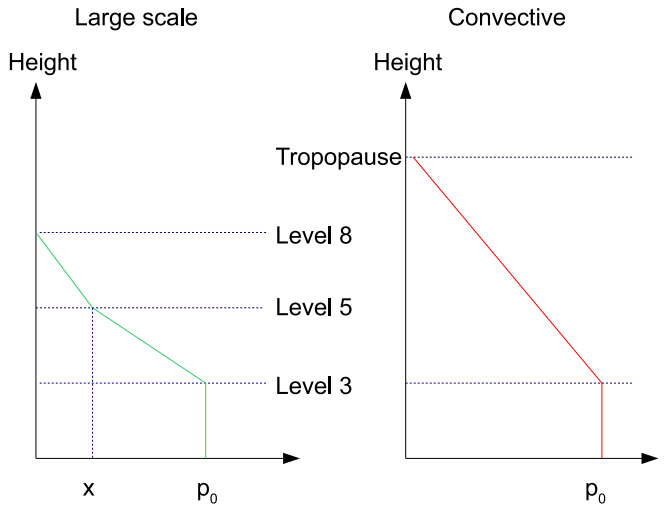

Figure 2-11 The vertical profile of precipitation for convective and large scale precipitation taken from Lunt (2001).

ERA-40 six hourly large scale precipitation, convective precipitation, low cloud and medium cloud cover data is downloaded from the ECMWF website http://data.ecmwf.int/data/d/era40_daily/. The data is interpolated from a 2.5 x 2.5 grid to a T42 spatial resolution.

2.6 Optimising TOMCAT

The most computationally intensive part of the LPJ-dust model is the transport component. This is because the tracer mass is transported by advection, convention and diffusion on a hourly basis in 3 dimensions. Therefore, several actions are taken to ensure the TOMCAT runs as fast as possible. A modification is made to the TOMCAT source code in order to speed up the simulation time. In the original source code a convection/diffusion matrix is defined. This matrix contains values by which the tracer mass is multiplied by, to move it into or out of a grid box by convection and diffusion. The matrix is written the disk every

six hours and read back into memory every hour. The reading and writing of this variable to disk is not efficient but the code was originally written this way because of limitations in memory on older machines. The source code is changed so that the matrix is stored in memory instead of reading and writing to the disk. The Appendix contains the modifications to the source code. To verify that the change does not cause an error the output dust fields are compared before and after this change is made. Storing the convection/diffusion matrix in memory gives a 10% reduction in the simulation time.

A single TOMCAT simulation can transport several tracers at a time. As the tracers do not interact with each other the simulations can be divided up so that one TOMCAT simulation contains one tracer. Transporting one tracer per TOMCAT simulation instead of eight tracers per simulation gives a 65% reduction in the simulation time. A further 20% improvement in the simulation time is obtained by running TOMCAT using openmp.

2.7 A base line dust simulation

A flow chart of the dust model is shown in Figure 2-12. A dust cycle simulation is run for the years 1987 to 1989. These years are chosen so that surface emissions could be compared to the work of Tegen et al., (2002). Figure 2-13 shows the annual mean dust source areas calculated using LPJ vegetation cover, soil moisture and snow depth data using Equation 2-10. Figure 2-14 shows the corresponding surface emissions.

The model predicts dust emissions from North America (the great Basin, Mojave and the Sonoran deserts). In South America, the model predicts dust emissions from the Atacama Desert which extends up the coast of Chile and in Patagonia in south central Argentina. In Africa the model predicts dust emission from the Sahara in the north and the Namib and the Kalahari deserts in the south. There are also dust emissions from Somalia in east Africa. In Asia there are dust emissions from Gobi desert in the East Asia and the Taklimakan and Kara-Kum deserts in central Asia. In India and Pakistan dust emissions from the Thar Desert are simulated. Dust emission from the Australian continent and the Arabian Peninsula are also predicted by the model. High latitude dust emissions can be seen in the Canadian Arctic and in North West Russia.

The amount of dust removed by wet and dry deposition and the total deposition (wet +dry) is shown in Figure 2-15. The total dust deposition is largest close to the source regions.

Dry deposition is dominant close to the dust source regions because of the abundance of heavy particles at the source. In addition to this, there is generally a lack of precipitation in these regions which means dry deposition is the prevailing mechanism for removal. In contrast wet deposition dominates in areas far from the source.

The model shows that dust emitted from North Africa is transported westward across the Atlantic Ocean. Asian dust is transported eastward over the Pacific Ocean. Australian dust is transported northward across the Indian Ocean and south-eastwards towards New Zealand.

The annual mean surface emissions predicted by the new dust model are 1944 $Mtyr^{-1}$ (averaged over the years 1987-1990). Table 2-2 shows a comparison between the annual mean emissions estimated by other dust cycle models. The surface emissions lie within the range predicted by the other models. However, this range varies by a factor of 2. Although all the models agree that the highest emissions come from North Africa there are regional differences in the estimates of the surface emissions between the models. The baseline simulation presented here has not been validated against measurement data. In then next chapter the LPJ-dust model will be tuned to observational data. The tuning will aim to find the threshold parameters and sub-cloud scavenging scheme which optimises the fit between the model output and observational data.

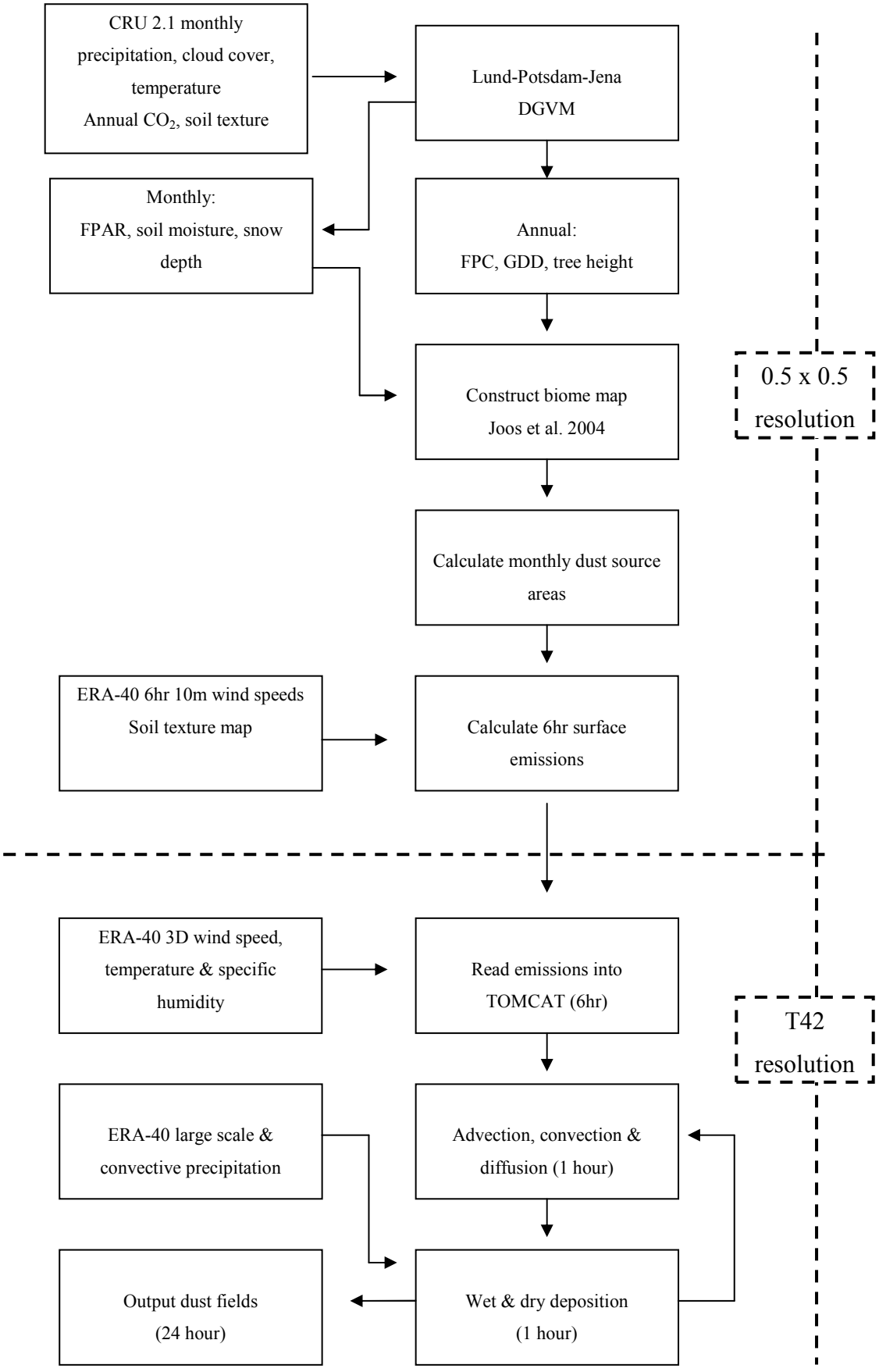

Figure 2-12 A flow chart of the dust cycle model

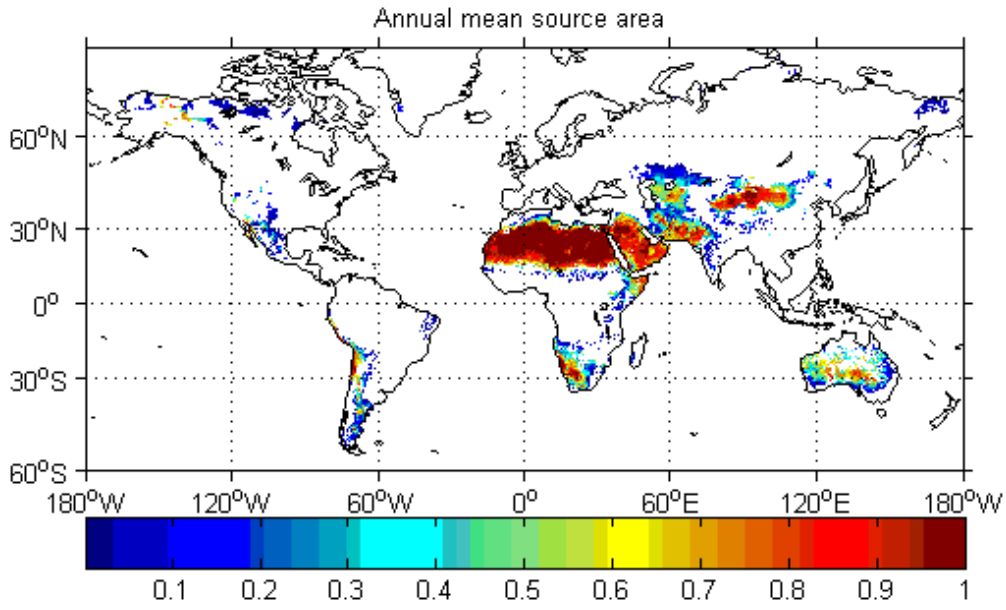

Figure 2-13 Annual mean dust source areas calculated using LPJ vegetation cover, soil moisture and snow depth data for the year 1987. The threshold limits used to calculate this are FPAR=0.5, snow depth =0.05m, soil moisture=20mm

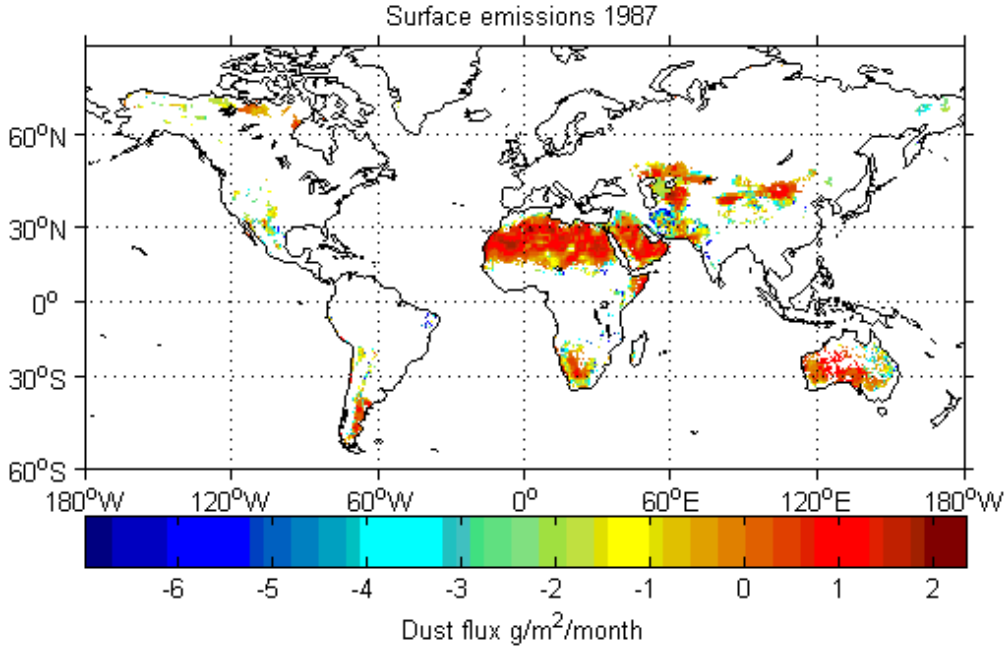

Figure 2-14 Annual mean dust flux calculated using LPJ source areas for the year 1987 (A logarithmic scale has been used)

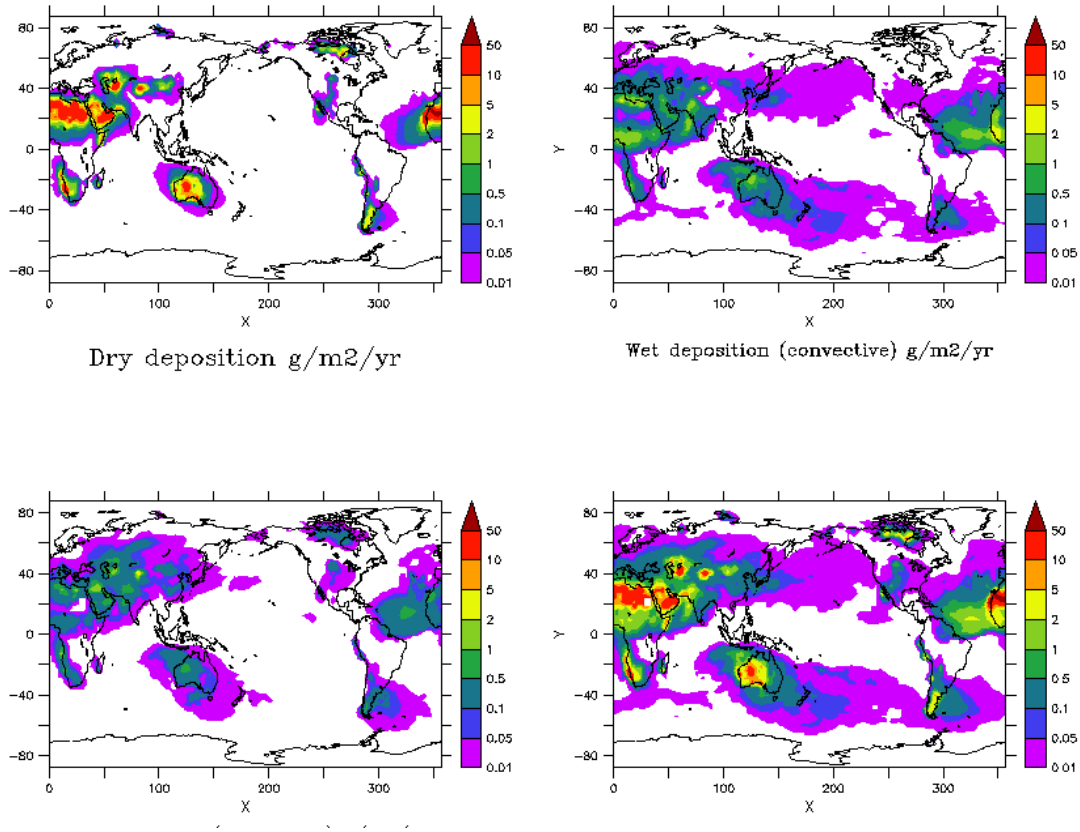

Figure 2-15 The amount of dust removed by dry deposition (top left), convective precipitation (top right), large scale precipitation (bottom left) and the total dust removed (bottom right) for the year 1988.

	Africa		Asia			America		Australia	Global
	North	*South*	*Arabia*	*Central*	*East*	*North*	*South*		
This work	60%	5%	10%	11%		1%	3%	10%	1944
(Tanaka and Chiba 2006)	58%	3%	12%	8%	11%	0.1%	2%	6%	1877
(Werner et al. 2002)	65%		10%	9%				5%	1060
(Luo et al. 2003)	67%		7%		3%			8%	1654
(Zender et al. 2003a)	66%		28%			0.5%	2%	3%	1490
(Ginoux et al. 2004)	69%		24%			0.4%	3%	3%	2073
(Miller et al. 2004)	51%		4%	16%	5%	5%		15%	1019

2-2 Comparison of the annual mean dust emissions categorised by region between this study and other studies. The dust emissions are in units of Mt yr^{-1}. This table has been taken from the work of Tanaka and Chiba (2006) and extended.

3 Dust model tuning

The previous chapter showed that the basic LPJ-dust model predicted annual mean surface emissions of 1944 Mtyr-$^{1.}$ This lies within the range of estimates predicted by previous dust modelling studies, however, theses estimates vary by a factor of 3 (see the dust model inter-comparison Table 1.5-1).

Uncertainty in the surface emissions can arise from the meteorological data used to drive the model. The surface emissions are forced using ERA-40 6 hourly wind speed data. Measurements of wind speeds over southwest Asia have been found to exceed 40ms^{-1} (Middleton 1986) . According to the ERA-40 data maximum wind speeds in this region reach only 27ms^{-1}. The ERA-40 reanalysis data requires data from meteorological stations which are sparsely distributed in remote dust source regions. This means that the reconstructed wind speeds may be less accurate in regions where there are little or no meteorological stations (Trenberth and Olson 1988).

Uncertainty in the surface emissions also arises from the way in which the soil type is described. This is because the soil type determines the size of particles available for dust entrainment. The LPJ-dust model uses the Zobler soil texture map (Zobler 1986) to describe the soil type. This map does not include different soil types for preferential source regions in which highly erodible alluvium sediment has accumulated. Furthermore, the data does not account for regions where the soil is compacted, cemented or crusted. Dust emissions will not occur in these regions even if the wind speeds are very high.

The threshold parameters used to calculate the surface emissions are another source of uncertainty in the LPJ-dust model. It was seen in Chapter 2 that a threshold limit for FPAR, soil moisture, snow cover and threshold friction velocity was required to calculate surface emissions.

Values for the threshold friction velocity for particles of different sizes have been measured in wind tunnel experiments (Bagnold 1941; Gillette 1977; Shao and Raupach 1993), however, less is known about the threshold limits for vegetation cover, soil moisture and snow cover.

A study by Kimura et al., (2009) found dust outbreaks occurred when vegetation cover was below 18%, soil moisture (ratio of surface soil water content to the field capacity (θ_r)) was greater than 2 with wind speed ≥ 7 m s^{-1} and $\theta_r < 0.2$ with wind speed ≥ 9 m s^{-1}. This study was carried out over the Loess Plateau in East Asia using NDVI data, wind measurements from surface synoptic observations and a three layer soil model to calculate soil moisture.

Using threshold limits from an observational study such as Kimura et al., (2009), in the LPJ-dust model, would have limitations. 18% vegetation cover calculated from NDVI data may not be comparable to the density of vegetation associated with LPJ FPAR. Indeed, in chapter 2, it was seen that LPJ systematically overestimated FPAR compared to remote sensing derived FPAR from SeaWiFS. The study was carried out in the Loess Plateau in East Asia and considered heavy loam, medium loam, light loam, sandy loam and sand soil types. This may not be applicable to other regions where the soil type is different.

A modelling study by Lunt and Valdes (2002) showed that choice of threshold limits for vegetation cover, soil moisture, and threshold friction velocity affected the atmospheric dust loading. The sensitivity of the atmospheric dust loading model to the threshold values varied regionally. It was shown that increasing the LAI threshold, obtained from the BIOME4 model, from 1.2 to 2 increased the total atmospheric dust loading by a factor of 1.6 with the most sensitivity observed in Australia. Similarly, reducing the soil moisture threshold from 10% to 4% decreased in the total column loading by a factor of 0.71 with most sensitivity seen over Patagonia. A weak sensitivity was found between the total column dust loading at high latitudes and snow cover. When the threshold friction velocity was increased from 0.4 to 6ms^{-1} the total column loading increased globally by a factor of 19. Clearly, the choice of values for the threshold limits in a dust model will have a large impact on both the surface emissions and the total dust loading.

A way to reduce the uncertainty in the threshold values used to calculate the emissions is to perform a model tuning. Tuning involves running the model using different values for the threshold parameters to optimise the fit between the model predictions and the observational data. Dust model tuning has not been carried out before. However, the availability of increased computing resources has made it possible to carry out ensemble simulations such as this.

Different strategies are available to tune the model. An approach taken by Jones et al. (2005) is to iteratively tune the model. They tuned the FAMOUS OAGCM so that it could reproduce the behaviour of HadCM3. FAMOUS uses the same physics and dynamic processes as HadCM3 but has a reduced horizontal and vertical resolution and a longer time step making it run 10 times faster. The iterative tuning was carried out by perturbing one parameter at a time by ±10% of its best estimated value. The performance of the simulation was compared to a control experiment and assigned a skill score. They calculated how the skill varies as a function of each parameter. This is then used to decide which direction the parameter needs to change for the next model run in order to increase the model skill. By doing this they iterated towards the model configuration which maximised the skill score.

Another approach to model tuning has been to select values for tuneable parameters using Latin Hypercube Sampling (McKay et al. 1979). This technique divides each tuneable parameter into equal intervals (N) of equal probability (1/N). One sample is selected at random from each interval and matched up randomly with a sample selected for another parameter. The advantage of this technique over randomly choosing values is that it ensures that all regions of parameter space are evenly sampled.

This approach has been taken by Edwards and Marsh (2005) to tune parameters in a 3-D ocean climate model. The objective of this tuning was to calculate a spread of model predictions for the global mean warming due to uncertainty in the model parameters.

Latin Hypercube Sampling has also been used by Schneider von Deimling et al. (2006) to determine the uncertainty in the *climate sensitivity*. This is defined as the change in the global-mean equilibrium surface air warming caused by a doubling of doubling of CO_2. They tuned parameters in the CLIMBER-2 (Petoukhov et al. 2000) intermediate complexity climate model. Ensemble simulations for the LGM were run and proxy data for sea surface temperatures were used to constrain the model. By doing this, they could estimate the uncertainty in the climate sensitivity caused by uncertainty in the model parameters.

More complex algorithms have been used to tune Earth systems models such as the Kalman filter (Annan et al. 2005) and the Kriging and Genetic Algorithm (Price et al. 2007). The advantage of the Latin Hypercube Sampling technique is it can be easily

implemented. For this reason, it is used to tune the threshold limits for vegetation cover, soil moisture, snow cover and threshold friction velocity the LPJ-dust model.

Another source of uncertainty in the LPJ-dust arises from the way in which physical processes are parameterised. This is called structural uncertainty. The parameterisation of wet deposition is an example of this. In the LPJ-dust model wet deposition is parameterised by the process of sub cloud scavenging. This is calculated simply as a function of precipitation rate (Brandt et al. 2002).

Sub cloud scavenging can be parameterised in different ways. The scavenging coefficient can be calculated as a function of raindrop size and particle-raindrop collision efficiency using the semi empirical relationship described by Slinn (1983). Alternatively, many dust models have used an empirical parameter called the scavenging ratio to calculate the rate of dust removal by sub cloud scavenging (Tegen and Miller 1998; Tegen et al. 2002; Cakmur et al. 2006). This is defined as the ratio of dust in collected precipitation divided by that in air. Measurements show that the scavenging ratio for submicron particles can vary from 500 to 1000 and is approximately 300 for larger size particles (Buat-Menard 1986).

Jung and Shao, (2006) examined the characteristics of four different sub cloud scavenging schemes within the framework of a dust cycle model. The choice of sub cloud scavenging scheme affected the ability of the model to accurately predict surface concentrations of dust at selected locations in Asia. Furthermore, the scavenging coefficient deviated by a factor of 1000 depending on the precipitation rate and particle size.

The objective of this chapter is to improve the performance of the basic LPJ-dust model. The threshold limits used to calculate dust emissions are tuned using Latin Hypercube Sampling and alternative sub cloud scavenging parameterisations are tested. The ensemble dust simulations are compared to observational data to assess which set of threshold values and removal scheme produces the best results.

3.1 Tuning the threshold limits for surface emissions

The threshold limits to be tuned using Latin Hypercube Sampling are the 1) FPAR limit, 2) soil moisture limit, 3) snow depth limit and 4) the threshold friction velocity. The model

calculates a different threshold friction velocity for each particle size using the semi-empirical relationship from Iversen and White (1982). The velocities are modified using the threshold friction velocity scale factor (TFVSF). Tuning TFVSF enables the threshold friction velocities to be tuned.

To select the values for the threshold limits using Latin Hypercube Sampling, the minimum and maximum range of each parameter and the total number of experiments must be known. It was decided to generate 20 sets of surface emissions using the threshold limits determined from Latin Hypercube Sampling. An extra set of surface emissions is calculated using the threshold limits for the baseline experiment in Chapter 2. This totals 21 sets of surface emissions. These are combined with three removal schemes giving a total of 63 experiments. The reason for carrying out this number of experiments is because of file space restrictions on the University of Bristol compute cluster. To avoid reading and writing large amount of data across the network the simulations were run on local nodes on the cluster which had a limited space for storing input and output data. This is also the reason why the tuning experiments are only run for 3 years (1987-1989).

These particular years are chosen for two reasons. The first is because Tegen et al., (2002) chose this time period to study so a comparison of the surface emissions predicted by the LPJ-dust model could be made with the work presented in that publication who show emission for the year 1988. The second reason is because there is good coverage of surface concentration measurements from the University of Miami aerosol network (J. Prospero D. Savoie, personal communication) over this period which is used to test the performance of the model.

The surface emissions are compared to another model (Tegen et al. 2002) to estimate the minimum and maximum range for the tuneable parameters. The saltation and sandblasting component of this model is used in the LPJ-dust model. The Tegen et al., (2002) has also has been found to give realistic results when compared to TOMS aerosol index and deposition rates. The Tegen et al., (2002) model is run for the year 1987 and the annual mean surface emissions are calculated. The LPJ-dust model is run using extreme values for the threshold limits for the year 1987 and the annual mean surface emissions are compared to that predicted by the Tegen et al., (2002) model.

The FPAR threshold range chosen is 0.2-0.5. Choosing values lower than 0.2 leads to very little dust emissions in South America, North America, South Africa and Australia. Choosing an FPAR threshold greater than 0.5 leads to dust emissions from highly productive grass lands where C4 grass is present.

The soil moisture threshold range chosen was 10mm to 25mm. The soil moisture refers to the water contained in the upper soil layer in the LPJ which has a depth of 0.5m. Choosing values lower than 25mm leads to an under prediction of dust emissions from central Asia, Australia and North America. The upper bound was selected so as to include emissions from the boundaries of the deserts, for example Sahel in North Africa.

The snow depth range chosen is 0.01m to 0.1m. Choosing a value less than 0.01m gives rise to an abundance of dust emission at high latitudes in winter. Using a snow depth greater than 0.1m eliminates dust emission from Gobi desert.

The TFVSF range is 0.4-1. This is determined on the basis of the total annual mean dust generated. Choosing a value of 0.4 for the TFVSF gives annual mean dust emissions of 3000 $Mtyr^{-1}$ which is the upper estimate predicted by other dust modelling studies that has been reposted in literature (Tegen and Fung 1994; Mahowald et al. 1999). Choosing a value of 1 for the TFVSC means the threshold friction velocities are not scaled. This results in annual mean dust emissions of 60 $Mtyr^{-1}$.

Figure 3-1 shows the variable space sampled for each parameter using Latin hypercube sampling. The threshold limits used to calculate the six hourly surface emissions are listed in Table 3-1. Because each parameter is randomly paired with another parameter, repeating the selection process would result in different values for the threshold parameters.

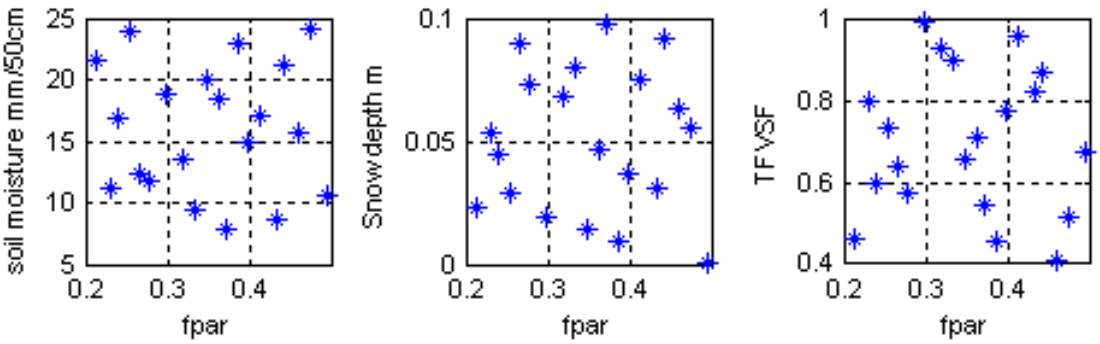

Figure 3-1 Variable space sampled using Latin Hypercube Sampling for the four threshold limits used to determine surface emissions

Experiment number	*FPAR (%)*	*Soil moisture (mm)*	*Snow depth (meters)*	*Threshold wind scale factor*
Range	0.2-0.5	10-25	0.01-0.1	0.4-1
1	0.50	0.20	0.01	0.66
2	0.37	7.79	0.10	0.55
3	0.23	11.09	0.05	0.80
4	0.32	13.56	0.07	0.93
5	0.21	21.50	0.02	0.46
6	0.46	15.75	0.06	0.41
7	0.36	18.47	0.05	0.71
8	0.30	18.82	0.02	0.99
9	0.39	22.99	0.01	0.46
10	0.28	11.68	0.07	0.58
11	0.47	24.18	0.06	0.51
12	0.33	9.49	0.08	0.90
13	0.25	23.88	0.03	0.73
14	0.24	16.86	0.04	0.60
15	0.49	10.53	0.00	0.68
16	0.35	19.92	0.01	0.66
17	0.40	14.93	0.04	0.78
18	0.41	17.04	0.08	0.96
19	0.44	21.24	0.09	0.87
20	0.43	8.65	0.03	0.82
21	0.27	12.41	0.09	0.64

Table 3-1 Threshold limits used to determine source areas. Experiment 1 corresponds to the threshold values used for the basic LPJ-dust simulation described in the Chapter 2. Experiments 2-21 correspond with threshold limits generated by Latin Hypercube Sampling.

3.2 Sub-cloud scavenging schemes

Three sub-cloud scavenging parameterisations are tested. The first parameterisation estimates the scavenging coefficient as a function of the precipitation rate. This parameterisation is taken from the work of Brandt et al., (2002) and has been described in section 2.5.2.

The second and third sub-cloud scavenging schemes are based on the semi-empirical expression for the aerosol droplet collision efficiency described by (Slinn 1984). The collision efficiency is calculated as

$$E = \frac{4}{\mathrm{Re}\,Sc}\left[1 + 0.04\,\mathrm{Re}^{1/2}\,Sc^{1/3} + 0.16\,\mathrm{Re}^{1/2}\,Sc^{1/3}\right] + 4\phi\left[\omega^{-1} + \left(1 + 2\,\mathrm{Re}^{1/2}\right)\phi\right] + \left(\frac{St - S^*}{St - S^* + \frac{2}{3}}\right)^{3/2}$$

(Seinfeld 1998). Re is the Reynolds number, Sc is the Schmidt number, St is the Stokes number, φ is the ratio of the particle diameter to the drop diameter and ω is the ratio of the water viscosity to air viscosity.

The scavenging coefficient is calculated from the collision coefficient by assuming that all the rain droplets have the same size such that

$$\lambda = \frac{3}{2}\frac{Ep_0}{D_{droplet}}$$

Where $D_{droplet}$ is the rain droplet size and p_0 is the precipitation rate. The scavenging coefficient is calculated for a small size rain droplet with diameter 0.5mm and a larger rain droplet with diameter 2mm. These values are taken from measurements of rain droplets in stratisform rain with a precipitation rate of approximately $1\mathrm{mmhr}^{-1}$. (Pruppacher 1981)

Figure 3-2 shows the scavenging coefficient calculated for the three schemes using a precipitation rate of $1\mathrm{mmhr}^{-1}$. The straight line corresponds to the first parameterisation in which the scavenging coefficient is independent of particle size. The size dependent schemes have a hook shaped curve which indicates that scavenging is efficient for very small and very large particles. For very large particles the process of inertial impact is important for the removal while Brownian diffusion is important for very small particles. However, for particles in between the scavenging is not as efficient. This minimum is

called the Greenfield gap and effects particles in the region of 0.1µm diameter. It can be seen that the larger rain droplet has a higher scavenging coefficient than the smaller droplet size. This is because the big droplet sweeps out a larger volume as it falls than the smaller droplet removing more dust on its' descent.

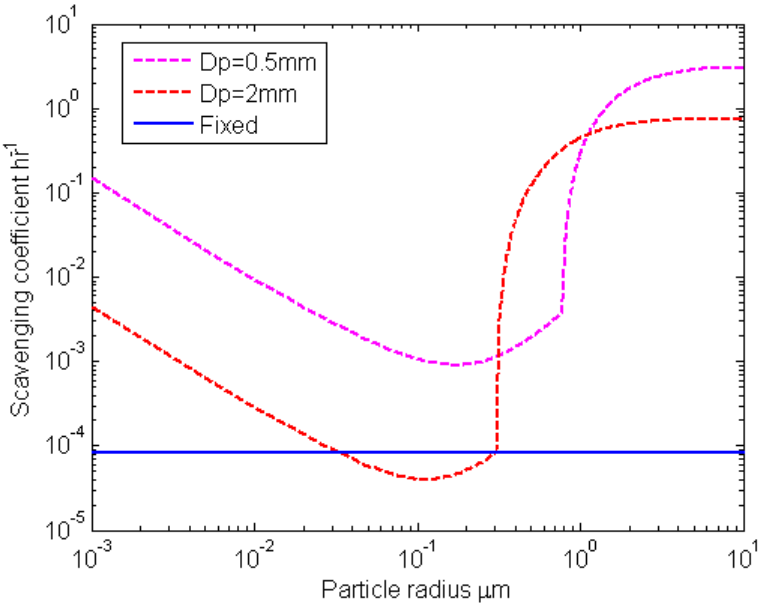

Figure 3-2 Comparison between the scavenging coefficients for three different wet deposition schemes. The dashed lines corresponds is the size dependent removal schemes (Slinn 1983) while the fixed line corresponds to the scheme fixed removal (Brandt et al. 2002). A precipitation rate of 1mmhr^{-1} is used to calculate the scavenging coefficient.

Table 3-2 lists the collision efficiency for each particle in the model assuming a rain drop diameter of 0.5mm and 2mm and precipitation rates of 1mmhr^{-1}. The table shows that dust particles with diameter greater than or equal to 13.8µm are removed with 100% efficiency in the LPJ-dust model.

D_p (µm)	***0.17***	***0.5***	***1.51***	***4.57***	***13.8***	***41.69***	***125.89***	***380.19***
0.5mm	3.9×10^{-4}	3.3×10^{-4}	1.2×10^{-3}	6.5×10^{-1}	1	1	1	1
2.0mm	5.6×10^{-5}	8.6×10^{-5}	4.1×10^{-1}	9.0×10^{-1}	1	1	1	1

Table 3-2 Collision efficiency between a falling rain droplet of size 0.5mm and 2mm assuming a precipitation rates of 1mmhr^{-1}. Values of 1 mean dust is removed with 100% efficiency.

As mentioned previously 63 tuning experiments are carried out. The experiments are run for the years 1987-1989. Data from the first year (1987) is discarded in the analysis as the model is allowed 1 year to spin up. The amount of dust removed by wet and dry deposition and the surface concentrations are output daily.

3.3 Target datasets

Three datasets are used to evaluate the performance of the experiments. Two of these datasets contain dust deposition rates and one contains surface concentration data.

The first deposition dataset is the Dust Indicators and Records of Terrestrial and MArine Palaeoenvironments (DIRTMAP version 2) (Kohfeld and Harrison 2001). DIRTMAP data has been used to validate many dust cycle models (Mahowald et al. 1999; Lunt and Valdes 2002; Tegen et al. 2002; Werner et al. 2002; Mahowald 2006; Yue et al. 2009). This dataset contains dust deposition data from ice cores, marine sediment cores, sediment traps and loess data at various locations around the globe. DIRTMAP data is downloaded from the publically available website ftp://ftp.ncdc.noaa.gov/pub/data/paleo/loess/dirtmap/version2/.

Dust deposition rates are derived from ice core measurements by combining measurements of particle concentration in ice with estimates of ice accumulation rates. The concentration of dust particles in ice is measured using several techniques. These techniques include laser light scattering, using atomic absorption to determine the Aluminium concentration or using Coulter counter measurements of number particle concentration. The error in the deposition rate is associated with the uncertainty in the estimate of the ice accumulation rate.

The DIRTMAP dataset also contains dust deposition estimated from sediment traps and marine sediment cores. A sediment trap is an instrument used to measure the quantity of sinking particulate matter in the ocean. The fraction of matter containing dust is calculated by extracting the organic carbon, carbonate and opaline components from the total particles. Marine sediment cores are samples taken from the ocean floor. The dust flux is calculated by measuring the dust fraction in the core and combining this with the sedimentation rate of the core. The dust fraction is found by extracting the carbonate and

opaline components of the core. Most cores are taken from the open ocean to avoid contamination from biogenic debris from rivers run off.

Dust deposition rates obtained from loess deposits are excluded in the analysis because there is evidence that they can be eroded (Derbyshire 2000) which would lead to unreliable estimates of deposition rates.

The second deposition dataset used for the model validation has been compiled by Ginoux et al., 2001. This consists of 16 measurement sites. The majority of the measurements come from the sea/air exchange program (SEAREX). This was a program established to monitor the transport of aerosols over the Pacific Ocean. Dust data collection in the North Pacific network started in early 1981 and in the southern Pacific in 1983. Dust deposition was measured using a conical funnel. The wet deposited parties fall into the funnel while the dry deposited particles settle on the outside of the funnel. The sample is filtered through a nylon mesh to remove debris and analysed for its Aluminium content.

The Ginoux et al., (2001) dataset also contains dust deposition rates measured from a high resolution ice core in the Alps in which Aluminium and Calcium record have been analysed to determine the dust composition. 13 out of the 16 sites in the Ginoux dataset have been taken over the period 1980-1990 which coincides with the time the dust model is run. The Ginoux data has been used to evaluate the performance of several dust models (Ginoux et al. 2001; Luo et al. 2003; Zender et al. 2003a; Zender et al. 2003b)

The third target dataset is surface concentration measurements from the University of Miami aerosol network (J. Prospero D. Savoie, personal communication). The network measures surface concentrations of dust at a number of different sites. All the sites are located at remote regions to avoid contaminating the measurement with dust from local sources. The longest dataset extends from 1965 to the present from Barbados. Before 1971 there was no electrical power on the island and measurements were taken by suspending a nylon mesh net in the wind. After that, measurements were taken by passing air through a filter using a pump. The mineral dust content is determined by baking the filter at 500^{o}C to remove the water soluble material. The remaining material on the filter is assumed to be mineral dust. A description of the measurement technique is contained in Prospero (1999).

The measurement data from this network is not available at all sites over all time periods. Complete data is available for the year 1989 at: Barbados, Bermuda, Miami, Mace Head, Midway Island and Izaña. The University of Miami surface concentrations data has been used to validate numerous dust cycle models (Ginoux et al. 2001; Lunt and Valdes 2002; Tegen et al. 2002; Luo et al. 2003; Zender et al. 2003a; Tanaka and Chiba 2006; Yue et al. 2009).

The monthly surface concentrations are used later in Chapter 4 to test if the model can predict the seasonal variability in surface concentrations. In chapter 5 the monthly measurements are also used to test if the model can predict inter-annual variability in surface concentrations.

Figure 3-3 shows the spatial distribution of the DIRTMAP, Ginoux and University of Miami data. The Ginoux data provides coverage in parts of the mid-Pacific ocean where there is no DIRTMAP data. It also provides data on land in Spain, the Alps and in the Taklimakan desert. The DIRTMAP data provides good spatial coverage in the ocean, the Arctic and in Antarctica. The University of Miami data provides additional data in the North West Atlantic where there is a scarcity of deposition data.

3.4 Results

To evaluate which simulation gives the best overall result, the experiments are ranked using a skills score. The skills score ranks the performance of the simulations using the normalised root mean square error (NRMSE). The NRMSE is used as opposed to the root mean square error because the measurement datasets have different units. The deposition data has units of ($gm^{-2}yr^{-1}$) while the surface concentration data has units μgm^{-3}.

First, the global tuning factor is calculated (T). This is the value by which the data is adjusted by to minimise the normalised root mean square error (NRMSE). T acts to move the modelled data up or down so that it fits on the ideal 1:1 line with the least amount of scatter. T is calculated by iterating through a range of values for T from 0.1 in steps of 0.1 to 100. The modelled data is multiplied by T and the value which minimises the NRMSE is selected and applied to the data.

The NRMSE is calculated as follows

$$NRMSE = \frac{RMSE}{o_{\max} - o_{\min}} \qquad \text{Equation 3-1}$$

Where o_{max} and o_{min} are the minimum and maximum observed values and RMSE is the root mean square error calculated as

$$RMSE = \sqrt{\sum_{i=1}^{n} \frac{(o_i - m_i)^2}{n}} \qquad \text{Equation 3-2}$$

Where m_i is the model data, o_i is the observations and n is the number of data points.

After T has been applied to the data the NRMSE associated with the DIRTMAP, Ginoux and Miami data is summed for each experiment to give a total NRMSE. The simulations are ranked according to the total NRMSE.

Table A (see the appendix) lists the experiments ranked by the total NRMSE after the tuning factor has been applied. Lower values of the total NRMSE indicate less error and a better match with measurement data. Table A also lists the T values for each dataset.

It can be seen from Table A that the best experiment is number 23 because it has the lowest total NRMSE. This experiment has threshold limits FPAR =0.37, soil moisture =7.79mm, snow depth =0.01m and TFVSF=0.55 and uses the size dependent removal scheme with rain droplet diameter 0.5mm. Incidentally, this experiment gives the highest correlation coefficient of all the experiments with monthly surface concentration data at Barbados. This is important as the longest continuous measurements of surface concentrations have been made at Barbados. The Barbados dust record is studied in further detail in Chapter 5. The un-tuned experiment ranks among the worst performing experiments, in 47th place.

Although not presented here, the same analysis was carried out using skills score based on correlation coefficient instead of NRMSE. Experiment number 23 ranked in the top 13% of all the experiments when correlation coefficient is used. The NRMSE is a better metric to use for the skills core because it quantifies the error between the measurements and the model data. The correlation coefficient is a measure to which the model data is linearly related to the measurements but does not quantify the total error.

Figure 3-4 shows the experiments ranked according to the total NRMSE. This is a graphical representation of the data from Table A (see the appendix). Experiments that use

the size dependent removal scheme using a rain droplet diameter of 0.5mm produce better results that the other two removal schemes.

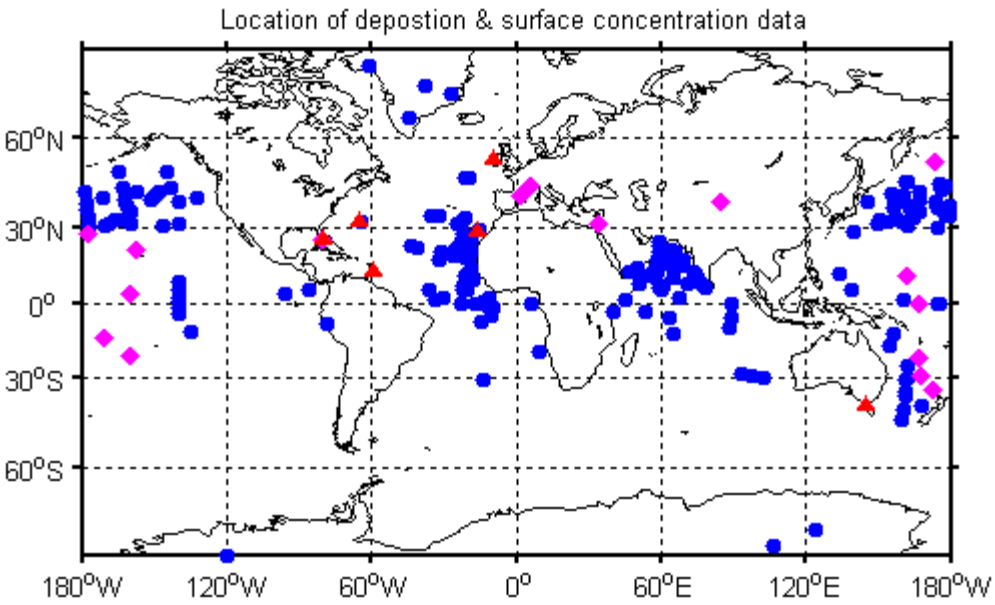

Figure 3-3 Location of DIRTMAP sites (blue), Ginoux data (Pink) and University of Miami data (Red).

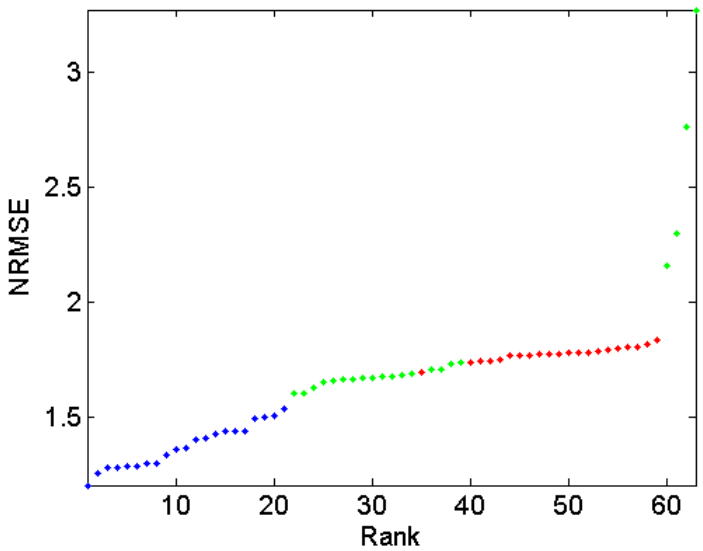

Figure 3-4 Experiments ranked according to the total NRMSE with the three validation datasets. Lower values of NRMSE indicate a better match with the measurement data. The removal schemes are designated by colour; the size dependent removal scheme with drop diameter 0.5mm (blue), the size dependent removal scheme with drop diameter 2mm (green) and the fixed scavenging schemes (red)

Figure 3-5 shows a comparison between the modelled deposition rates and the DIRTMAP data for source scheme 1, which is used in the un-tuned model and source scheme 2, which is used in the best experiment. The deposition rates predicted by the two source schemes and the three removal schemes are shown. In all cases the model successfully reproduces the range of high and low deposition over four orders of magnitude. There is very little change in the simulated deposition rates when a different source scheme used. However when the removal scheme is changed a notable different is observed.

The best experiment seen in Figure 3-5 (a) is successful at predicting the very low dust deposition found ice core records from Greenland and Antarctica. This indicates that the size dependent removal parameterisation with droplet diameter 0.5mm is good at simulating the long range transport of dust to Antarctica. In contrast the un-tuned experiment seen in Figure 3-5 (f) underestimates dust deposition in the North Pacific, Arabian Sea and the North Atlantic which can be seen in the abundance of points below the 1:1 line. There is an improvement in the correlation coefficient of 0.70 to 0.76 between the un-tuned experiment and the best experiment.

The T for each experiment is also shown in Figure 3-5. The removal scheme that uses a 0.5mm rain droplet results in higher T values than the removal scheme that uses a 2mm rain droplet. This is reasonable as it is expected that the large rain droplet will remove more dust than the smaller drop size, therefore the simulated data needs to be adjusted by a smaller amount to match the measurements.

Figure 3-6 shows a comparison with the Ginoux deposition data for the two different source schemes and three removal parameterisations. The best experiment seen in Figure 3-6 (a) correlates well with the measurements (r=0.94). The correlation coefficient may be artificially high because of the dominance of the Taklimakan data point which is located close to an active dust source. When this point is removed the correlation coefficient is 0.90. This is comparable to Zender et al., (2003b) found a correlation coefficient of 0.52-0.79 when the Taklimakan data point was removed. The fixed scavenging scheme underestimates dust deposition to the North Atlantic, the South Pacific and the North Pacific. Estimates of dust deposition to these regions are improved when the size dependent removal scheme with droplet diameter 0.5mm is used.

Figure 3-7 shows a comparison between the simulated surface concentrations and the measurements from the University of Miami aerosol network. The un-tuned experiment (Figure 3-7 (f)) underestimates surface concentrations in the North Atlantic but this is improved in the best experiment (Figure 3-7 (a)). Unlike the other two datasets, the simulated surface concentrations show sensitivity to both the choice of source schemes and removal schemes. This can be seen by the changes in correlation coefficient between experiments which use the same removal scheme but different source schemes and vice versa. This shows that tuning the threshold values improves estimates of surface emissions at remote regions. As with the other two datasets, the size dependent removal scheme with the drop diameter 0.5mm produces the best results.

Figure 3-8 shows the dust deposition fields for the three different sub cloud scavenging schemes. Source scheme 2 is used for each experiment so that the only difference between plates (a), (b) and (c) is the dust removed by wet deposition. The choice of sub cloud scavenging parameterisation does not have a large impact on deposition rates close to the source regions where dry deposition is the dominant removal mechanism. However, away from the source regions differences are evident as wet deposition is more effective at removing dust at long distances from the source regions. The size dependent removal scheme with droplet diameter 2mm and the fixed removal scheme produce more dust deposition downwind of the source regions than the fixed removal scheme with droplet diameter 0.5mm. This is seen over the North Pacific Ocean, the North Atlantic and the Southern Ocean.

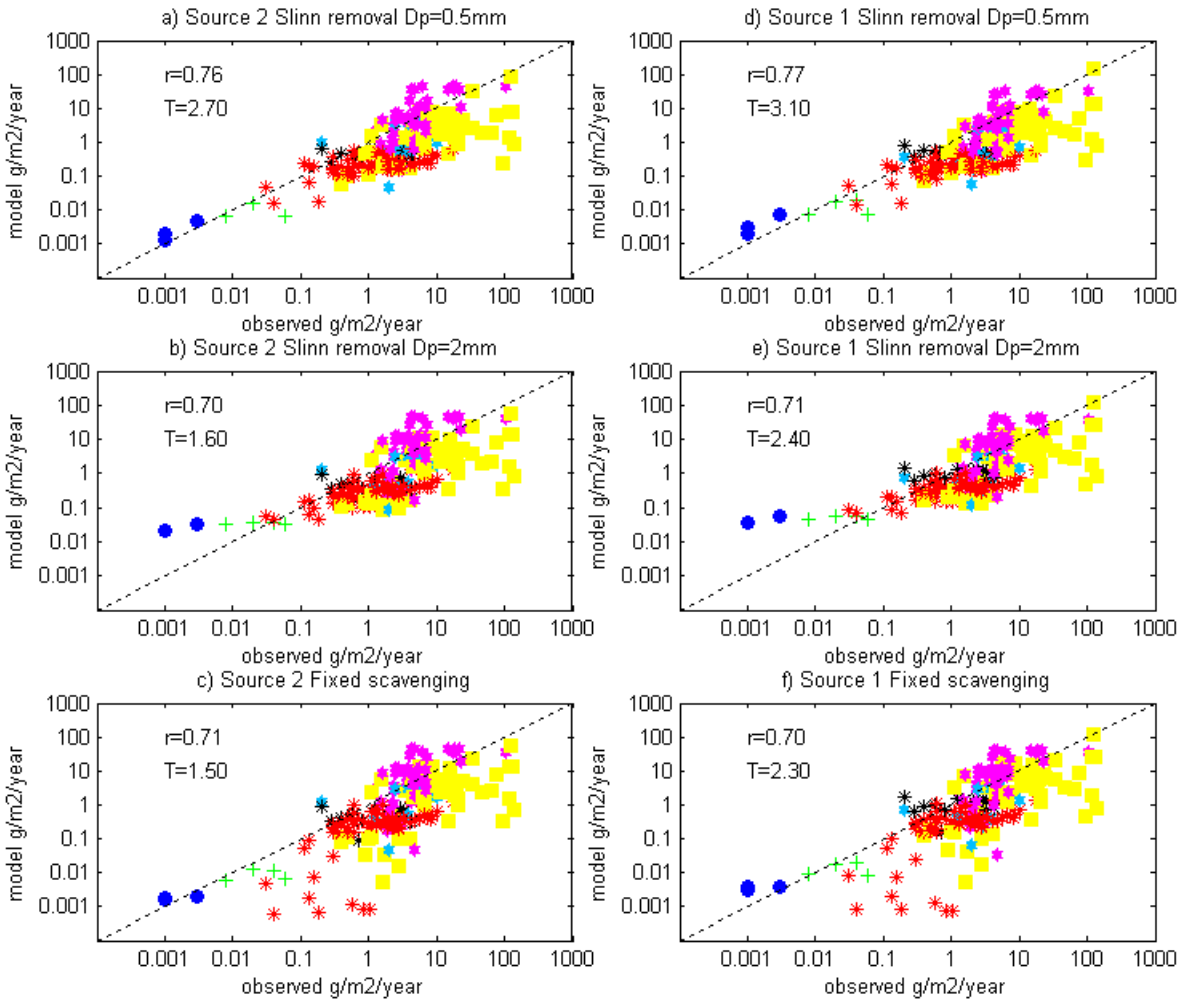

Figure 3-5 Comparison between the modelled deposition rates and DIRTMAP data using source scheme 2 (left hand side) and source scheme 1 (right hand side) and three removal parameterisations. The location of measurement sites are denoted by colour; Greenland (green), Antarctica (blue), North Pacific (red), South Pacific (black), North Atlantic (magenta), South Atlantic (pale blue), Arabian sea (yellow). The global tuning factor and logarithmic correlation coefficients are shown. Plate (a) corresponds to the best experiment while plate (f) to the un-tuned experiment.

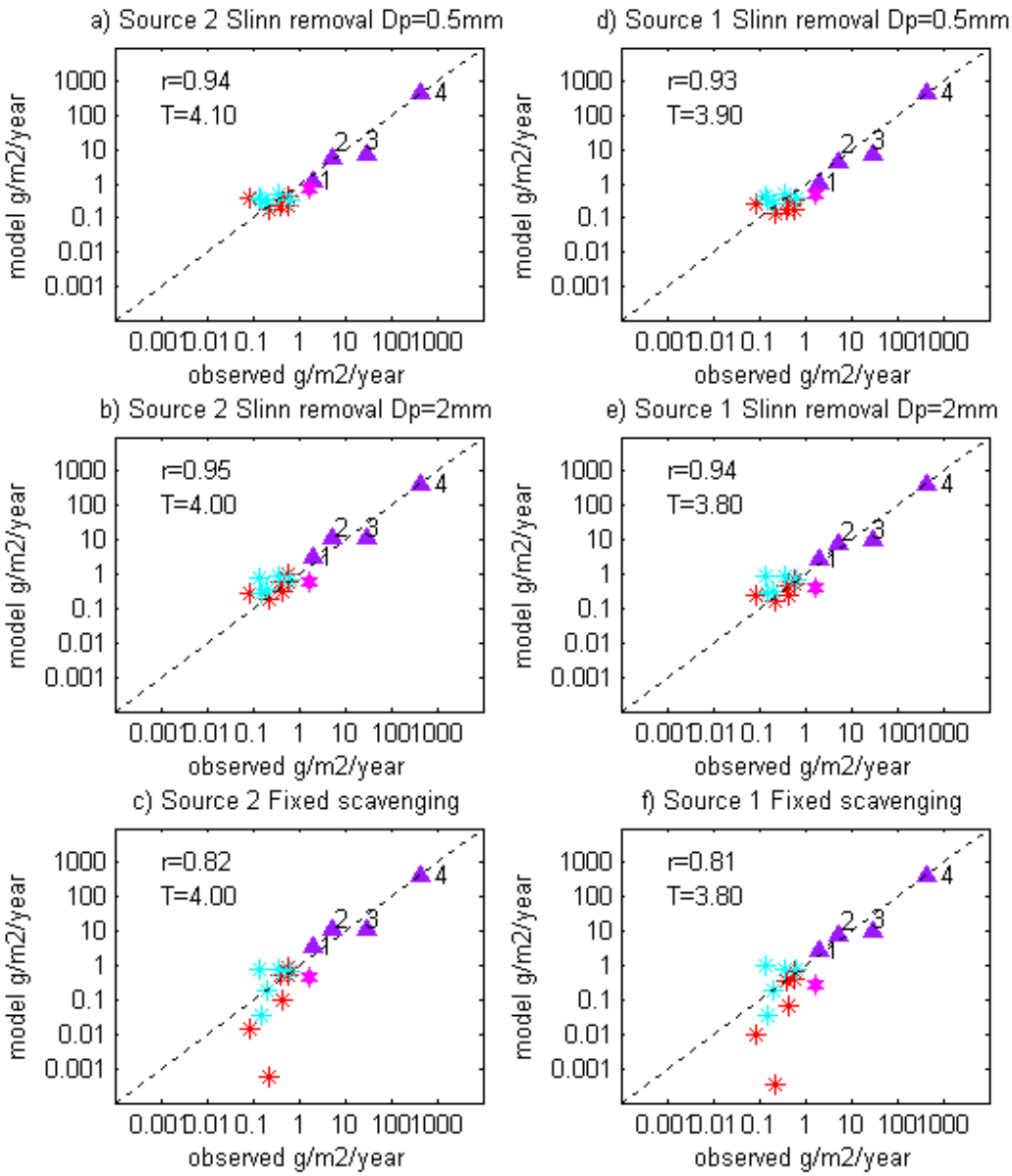

Figure 3-6 Comparison of modelled deposition rates against deposition data compiled by Ginoux et al., (2001). The plots show a comparison for three removal schemes using source scheme 2 (left and side) and 2 (right hand side). Sites are denoted in colour; North Pacific (red), North Atlantic (magenta), South Pacific (turquoise) , French Alps (purple 1), Spain (purple 2), Tel Aviv (purple 3) and the Taklimakan desert (purple 4). Plate (a) corresponds to the best experiment while plate (f) to the un-tuned experiment.

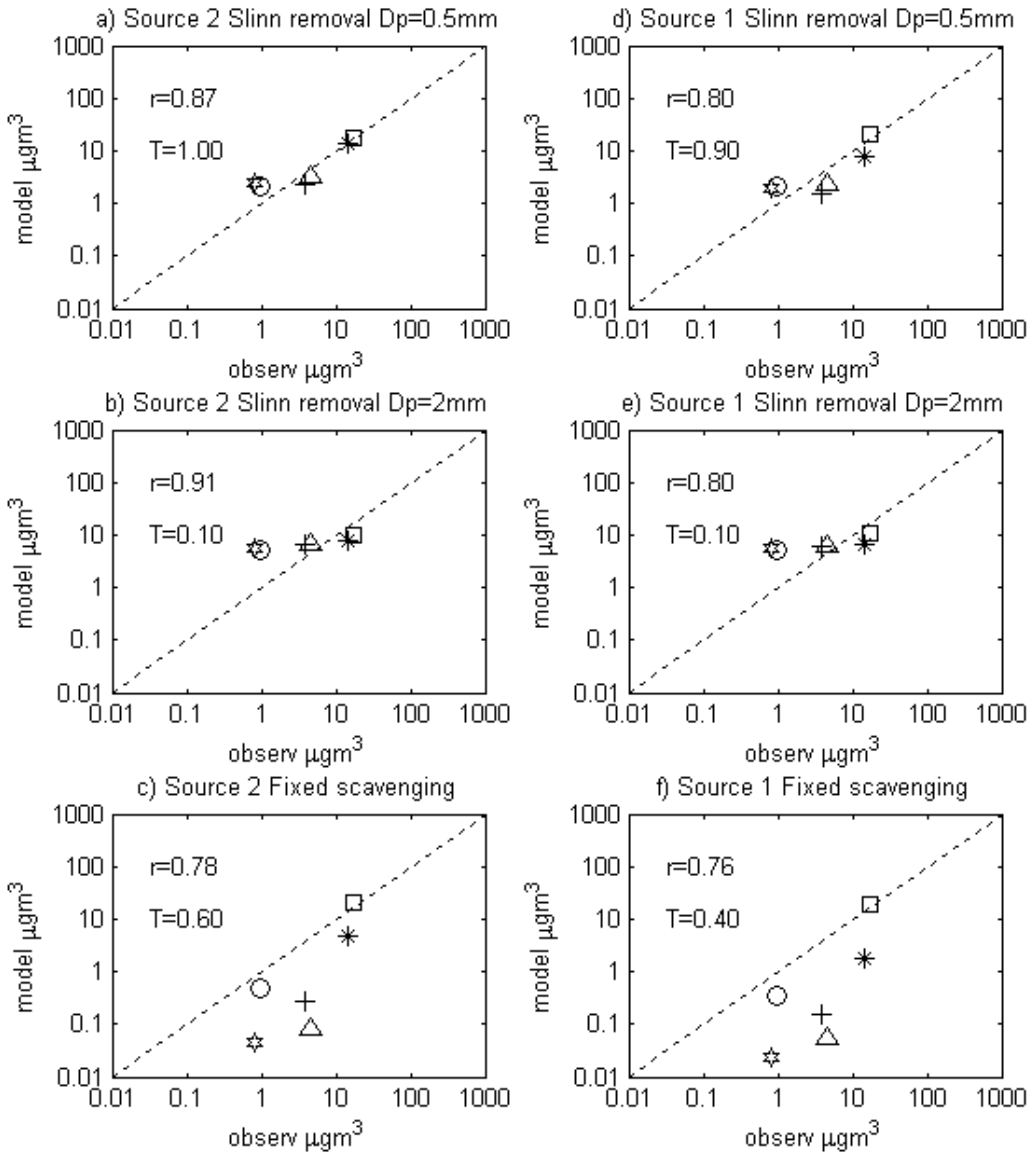

Figure 3-7 Comparison of simulated annual mean surface concentrations with data from the University of Miami aerosol network. The data points correspond to measurements made at 6 sites for the year 1989. The Barbados (asterix), Bermuda (triangle), Cape Grim (circle), Izana (square), Mace Head (star) and Miami (plus sign). Plate (a) corresponds to the best experiment while plate (f) to the un-tuned experiment.

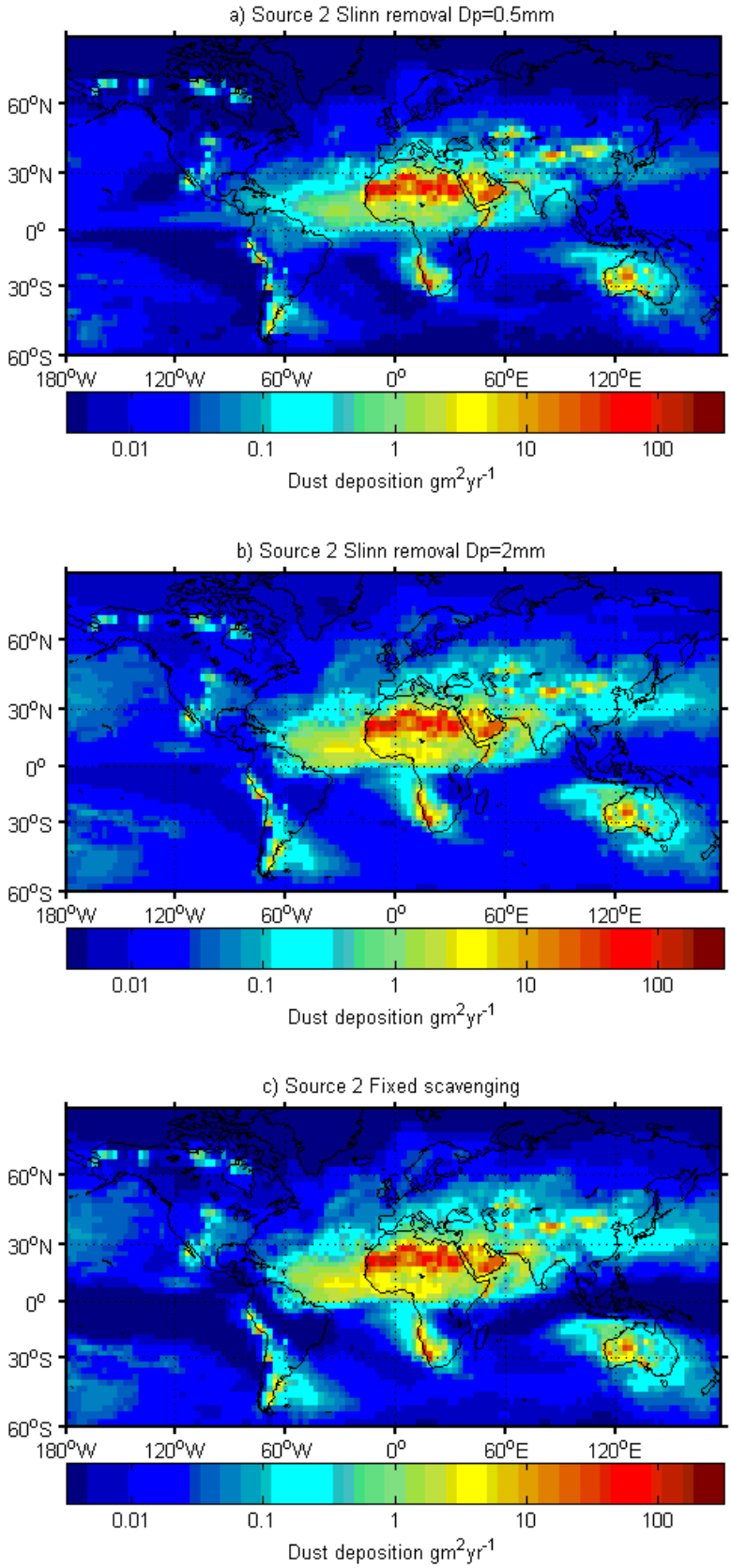

Figure 3-8 Comparison between simulated dust deposition fields, averaged over the year 1988 and 1989, when the three sub cloud scavenging schemes are used. Dust deposition referrs to the total dust removed by wet and dry deposition. Source scheme 2 is used for each experiment.

3.5 Uncertainties in the estimates of the surface emissions

The tuning factors for the best experiment are different for each target dataset. This results in different estimates for the annual mean surface emissions. These estimates range from 1136Mtyr^{-1} (T=1, University of Miami), 3065 Mtyr^{-1} (T=2.7, DIRTMAP) and 4654 Mtyr^{-1} (T=4.1, Ginoux). This spread arises from a number of factors.

The two deposition datasets measure dust deposition differently. Indeed, within the DIRTMAP and Ginoux datasets several different techniques are used to measure dust deposition. The techniques used also have uncertainties. Where deposition rates have been derived from ice core measurements, the ice accumulation rate is required to convert dust concentrations in ice core to units of deposition flux. The uncertainty in the ice accumulation rate may lead to an error in the values of the flux estimates. Errors in marine core data may be caused when ocean currents move sediment about.

The uncertainty is also caused by the differences in temporal coverage of the three datasets. The DIRTMAP data represents deposition over a long period of time while the Ginoux data contains measurements from the 1980s which is closer to the simulation period. Moreover, the University of Miami surface concentration data overlaps the simulation period exactly.

In Chapter 5 a long dust simulation is run for the years 1958-2000. The global tuning factor when comparing simulated deposition rates to DIRTMAP data is 0.93. This is closer to the value of T=1 calculated from the University of Miami data suggesting that a dust loading of 1136Mtyr^{-1} may be more likely.

Another source of uncertainty is caused by the spatial distribution of the measurement data. The data points are distributed unevenly which means that some regions are weighted more than others. Each observation whether from DIRTMAP, Ginoux or the University of Miami datasets has been made at a point source and might not be representative of the surrounding area.

3.6 Conclusions

This is the first time an objective tuning of a dust cycle model has been carried out. Tuning the dust model has resulted in improved estimates for the threshold parameters used to determine surface emissions and has identified the type of removal scheme required to predict the relative range of high to low deposition rates (and surface concentrations) close to and far from the source regions.

There is still a large degree of uncertainty in the estimates of the annual mean surface emissions even after tuning the model. This is a result of constraining the simulated deposition rates (and surface concentrations) against multiple measurement datasets. The estimate of the annual mean surface emissions varies from 1136 to 4654 $Mtyr^{-1}$ depending on which dataset the model output is compared to. Revisiting Table 1.5-1 in Chapter 1, which lists the total surface emissions estimated by previous modelling studies, it can be seen that a value of $1136Mtyr^{-1}$ lies within the range of values reported in the literature while a value of 4654 $Mtyr^{-1-}$ exceeds that estimated by previous work.

A large range of estimates for the annual mean surface emission has been found by Cakmur et al. (2006) who used multiple datasets to constrain dust emissions. In that study, a dust cycle model was optimised against DIRTMAP data, surface concentrations data, aerosol optical depth data and aerosol optical depth retrievals from the AVHRR sensor. They estimated that the annual mean surface emissions varied from of $1000\text{-}3000Mtyr^{--1}$.

There are places where improvements could be made to the model tuning. More measurement data could be used to assess the performance of the model. Measurement data close to the source region may be particularly useful. The majority of the measurements used in this tuning have been made in remote regions to minimise contamination from anthropogenic sources.

Another possible way to improve the model tuning is to introduce a weighting system. Cakmur et al., (2006) applied a weighting system when using observational data to constrain dust emissions. The weighing system they used, however, was somewhat arbitrary. AERONET data was weighted twice as much as TOMS data, while DIRTMAP and Ginoux deposition data was weighted half as much as the surface concentration data from the University of Miami aerosol network. Careful consideration would have to be

taken if a weighting system were to be introduced. This is because of inconsistencies between the spatial and temporal sampling used to produce each observational dataset.

The threshold values for the best experiment and the size dependent removal scheme with droplet diameter 0.5mm will be used in Chapters 4 and 5.

4 Seasonal variability in the global dust cycle

Much of what is known about the seasonality in the dust cycle originates from observational studies of dust storm frequencies (McTainsh and Pitblado 1987; Littmann 1991; Goudie and Middleton 1992) and remote sensing data over dust source regions (Prospero et al. 2002; Kaufman et al. 2005; Evan et al. 2006). Section 1.3.1 contains a summary of some of these observational studies. The studies show that there is a strong seasonal cycle in dust emissions which varies from region to region.

Dust cycle models are broadly able to predict the seasonal variability in surface emissions (Ginoux et al. 2001; Lunt and Valdes 2002; Tegen et al. 2002; Luo et al. 2003; Zender et al. 2003a; Tanaka and Chiba 2006; Yue et al. 2009). This has been determined by comparing simulated surface concentrations, down wind of the source regions, to in situ measurement data. The extent to which simulated surface concentrations agree with measurements, however, varies for individual models.

No dust cycle modelling studies have been reported in the literature which address the question of which processes are responsible for the seasonality in surface emissions or in dust loading after transport has taken place. Some dust cycle models may not be suited to this type of study because the seasonality in vegetation cover is not included (Lunt and Valdes 2002; Yue et al. 2009). In models where the seasonality in vegetation cover is included, the soil moisture used to suppress dust emissions is inconsistent with the vegetation cover. For example, in the work of Tegen et al., (2002) the BIOME4 model was used to predict the distribution of dust emitting biomes in conjunction with remote sensing NDVI to determine the seasonality in the vegetation cover. ERA-40 reanalysis soil moisture data was used in the model to suppress emissions. Similarly, Zender et al., (2002) used remote sensing derived monthly LAI to predict the distribution of vegetation cover combined with NCEP/NCAR volumetric water content to constrain dust emissions.

In contrast to previous studies the LPJ-dust model may be particularly suited to study the cause of seasonal variability in the dust cycle because it simulates seasonality in vegetation cover, soil moisture and snow cover, each of which impact dust emissions. Furthermore, there is consistency between the vegetation cover and the hydrology.

Chapter 4: Determining the cause of seasonal variability in the global dust cycle

There are two objectives in this chapter. The first is to evaluate how well the tuned LPJ-dust model predicts seasonality in the dust cycle. A comparison is made between the simulated total column dust loading and Total Ozone Mapping Spectrometer (TOMS) aerosol index to test if the model can predict the spatial distribution of the total atmospheric dust loading for different seasons. The simulated monthly mean surface concentrations are compared to measurements of surface concentrations from the University of Miami aerosol network as another means of model validation.

The second objective of this chapter is to investigate which processes control the seasonality in the dust cycle. The atmospheric dust loading is influenced by a number of factors. These include precipitation, which controls dust removal and soil moisture which inhibits dust emissions. The presence of snow, vegetation cover and surface wind speeds also influence dust emissions. It is possible then, that these factors also contribute to the seasonality in the dust cycle. For this reason sensitivity studies are carried out to investigate the extent to which wet deposition, surface wind speeds, soil moisture, snow cover and vegetation cover control the seasonal variability in the dust cycle in different regions.

4.1 Experimental setup

The LPJ-dust model is run for years 1990-2000 using threshold parameters and the size-dependent removal scheme determined from the model tuning carried out in chapter 3. This period has been chosen because the majority of the surface concentration measurements from the University of Miami aerosol network have been made over this period. The simulated surface concentrations and the total column dust loading are output daily. The total column dust loading is calculated by summing of the dust mass per unit meter in all 31 model levels.

4.2 Results

Figure 4-1 shows the seasonal variation in the simulated surface concentrations averaged over the simulation period 1990 to 2000. The highest surface concentrations are found close to the source regions in North Africa, Central Asia, China and Mongloia, Australia, South Africa, Patagonia and North America.

The model shows a latitudinal shift in the dust plume over the North Atlantic from DJF to JJA. This seasonal shift is associated with a change ITCZ which moves northwards in the JJA transporting dust to the Caribbean. In the DJF the ITCZ shifts southwards transporting dust to South America. The change in transport between the JJA and DJF predicted by the model has been observed from remote sensing retrievals of dust loading (Prospero et al. 2002; Kaufman et al. 2005; Evan et al. 2006).

The model predicts an increase in surface concentrations in spring in Asia. This is particularly evident in the Taklimakan and the Gobi. The increase in surface concentrations in spring is consistent with observations of dust storm frequencies which have a maximum in the spring (Littmann 1991; Goudie and Middleton 1992; Wang et al. 2004). The model produces higher surface concentrations over Patagonia in DJF than during the rest of the year. This agrees with measurements of dust deposition rates over Patagonia which have been found to increase in DJF (Gaiero et al. 2003).

In Australia, the surface concentrations are expected to peak in DJF when temperatures are highest, soil moisture is at its lowest and dust storm events are more frequent (McTainsh and Pitblado (1987). However, it can be seen that an increase in surface concentrations in Australia actually begin in SON which is earlier than expected. A closer inspection of the simulated emissions from Australia in Figure 4-2 shows that the increase occurs between September-January. The early onset of maximum dust emissions is because LPJ predicts minimum vegetation cover four months earlier than observed (See the comparison between the timing of the minimum FPAR from LPJ and SeaWiFS in Figure 2-3).

It is not clear from Figure 4-1 how the surface concentrations change seasonally over North America and South Africa, so these regions are also discussed in further detail in the following section, in which the simulated dust loading is compared to remote sensing data.

The annual mean surface emissions predicted by the model is 2660 ± 340Mtyr^{1} where the error refers to the standard deviation of the annual mean values. This value has been calculated over the period 1990-2000. This estimate is different from the value estimated in chapter 3, which was which 1136 Mtyr^{1,} calculated over a 3 year period from 1987-1989. The values for the total surface emissions are comparable to previous modelling studies (see Table 1.5-1)

4.2.1 Simulated dust loading: Comparison with TOMS

In this section the simulated dust loading is compared to satellite derived data to provide a qualitative evaluation of the spatial distribution of the dust loading as it varies seasonally. The comparison is focused on five major dust producing regions; North Africa and the Arabian peninsula, South Africa, North America, South America and Asia. Australia is not included in the comparison because the model is unable to predict the seasonality correctly.

The simulated dust loading is compared to TOMS aerosol index (Herman et al. 1997) obtained from the Earth probe satellite. The TOMS instrument measures radiation in the UV spectrum which is sensitive to the presence of aerosols such as black carbon, soot and mineral dust. TOMS aerosol index is calculated by dividing the measured UV radiation backscattered to space by the UV radiation backscattered to space in a pure Raleigh atmosphere such that

$$AI = 100 \log_{10} \frac{I_{360}^{meas}}{I_{360}^{calc}} \qquad \text{Equation 4-1}$$

Where I_{360}^{meas} is the measured radiation at 360mn and I_{360}^{calc} is the calculated radiance assuming a pure Raleigh atmosphere.

The magnitude of the AI depends on a number of factors such as the optical properties of the aerosol, the thickness and height of the aerosol layer, the viewing angle of the sensor and whether cloud is present. It is worth noting that the TOMS AI data does not distinguish between natural mineral dust and other absorbing aerosols such as black carbon from a biomass burning.

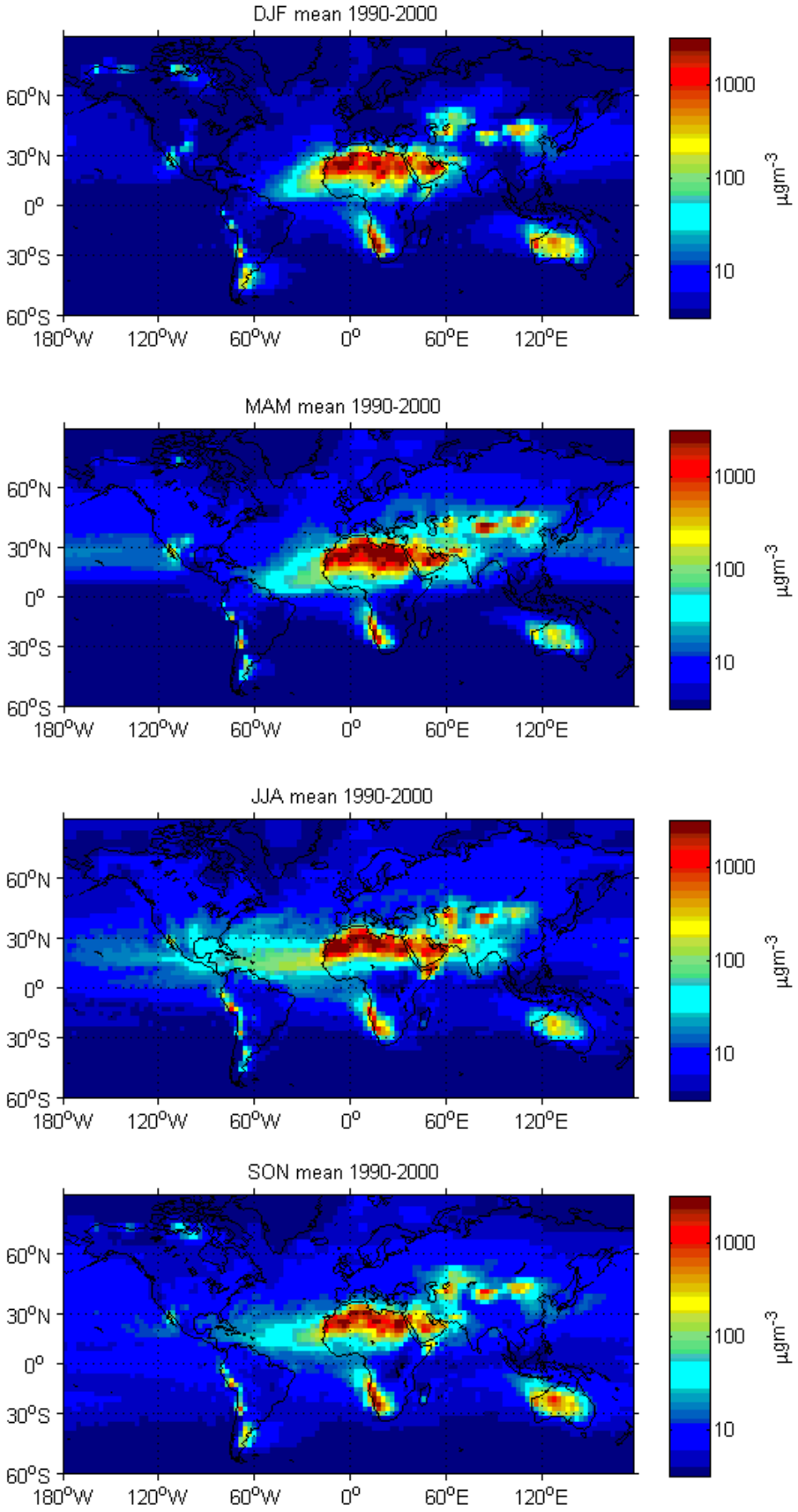

Figure 4-1 Seasonal variation in simulated surface concentrations. The seasons are defined as December-January-February (DJF), March-April-May (MAM), June-July-August (JJA) and September- October-November (SON)

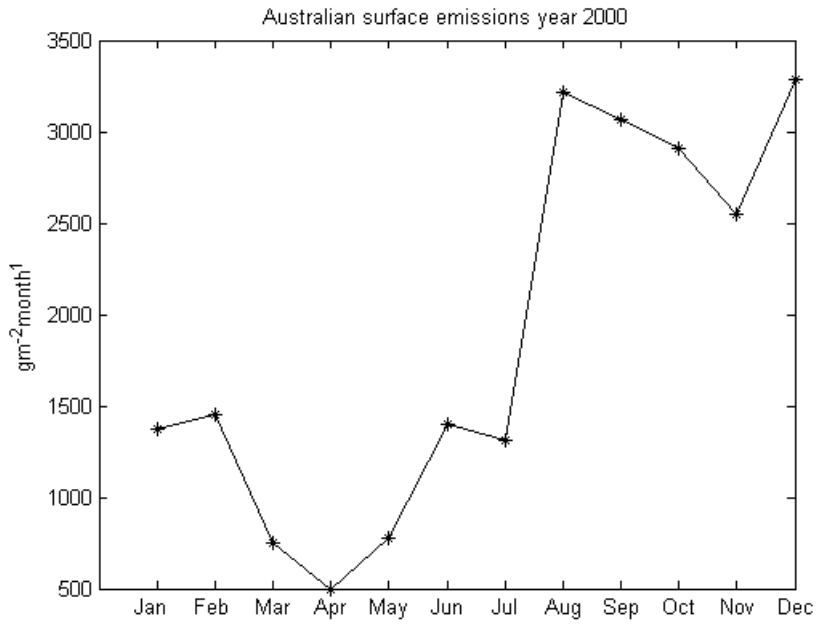

Figure 4-2 Simulated monthly surface emissions from the Australian continent. The emissions are summed over longitudes 100°E to 170°E and latitudes 50°S to 0°. Maximum emissions from Australia are expected in DJF. The model predicts maximum emissions commencing in August. This coincides with the period when LPJ simulates a minimum in vegetation cover.

The TOMS AI data provides a useful qualitative tool to evaluate the model and has been used previously to map the location of major dust sources (Prospero et al. 2002). TOMS data has also been used to monitor the inter-annual variability in dust transport from North Africa (Chiapello et al. 2005). The monthly composite TOMS aerosol index data for the year 2000 is downloaded from the NASA website (ftp://toms.gsfc.nasa.gov/pub/eptoms/data/monthly_averages/aerosol/). The data has a spatial resolution of 1° latitude and 1.25° longitude.

Figure 4-3 shows the total column dust loading over the North Atlantic predicted by the model in DJF and JJA and the TOMS aerosol index. The model is able to predict the high dust loadings in JJA over North Africa, the Arabian Peninsula and the North Atlantic that is seen in the TOMS data. The latitudinal shift in dust transport over the North Atlantic in the DJF and the JJA caused by the movement of the ITCZ can be seen in the model and the observations. The TOMS data shows high dust aerosol loading just north of the equator in JJA which is not seen in the model. This is caused by smoke from biomass burning (Prospero et al. 2002).

The simulated total column dust loading and the TOMS AI for South America in DJF and JJA is shown in Figure 4-4. The model correctly predicts the high dust loading in the DJF in the Patagonian desert compared to JJA.

The model does a reasonably good job at predicting the spring increase in dust loading over Asia compared to the TOMS data as seen in Figure 4-5. Observational studies suggests that the peak dust loadings in spring are caused by cold fronts emerging from Siberia which increases the frequency of wind speed events (Littmann 1991; Goudie and Middleton 1992; Wang et al. 2004).

In North America, the model and the remote sensing data predict higher dust loading in spring than in winter. This can be seen in Figure 4-6. This is consistent with observational studies of visibility and total suspended particulates at sites in the northern US which show an increase in spring time (Orgill and Sehmel 1976).

The simulated dust loading over South Africa in DJF and JJA and the TOMS data are shown in Figure 4-7. The model correctly predicts an increase in dust loading in the DJF compared to JJA. High dust loadings are seen in the TOMS data in the west coast of South Africa in JJA. This is not seen in the model and is associated with biomass burning (Hao and Liu 1994; Prospero et al. 2002).

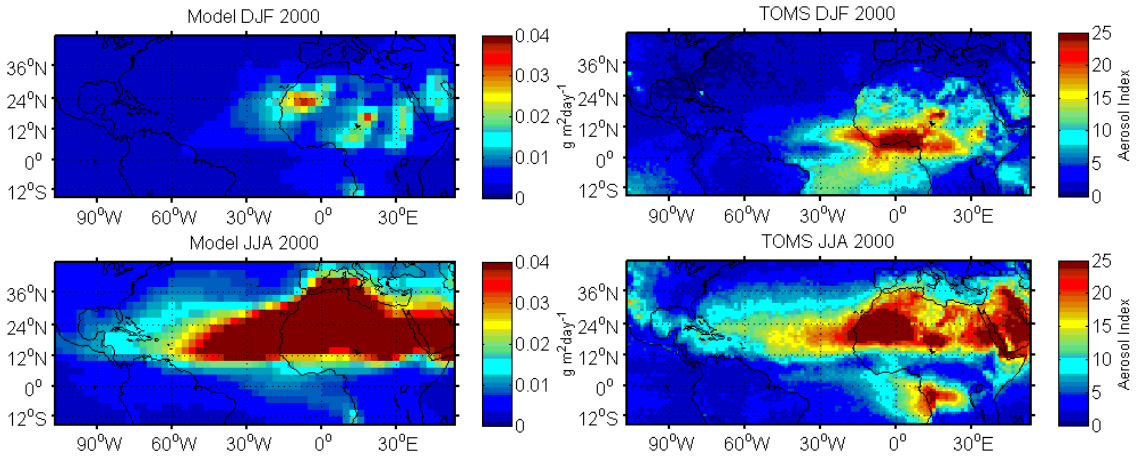

Figure 4-3 Comparison of total column dust loading over the North Atlantic for the NH winter (December-January-February) and summer (June-July-August) compared to TOMS aerosol Index.

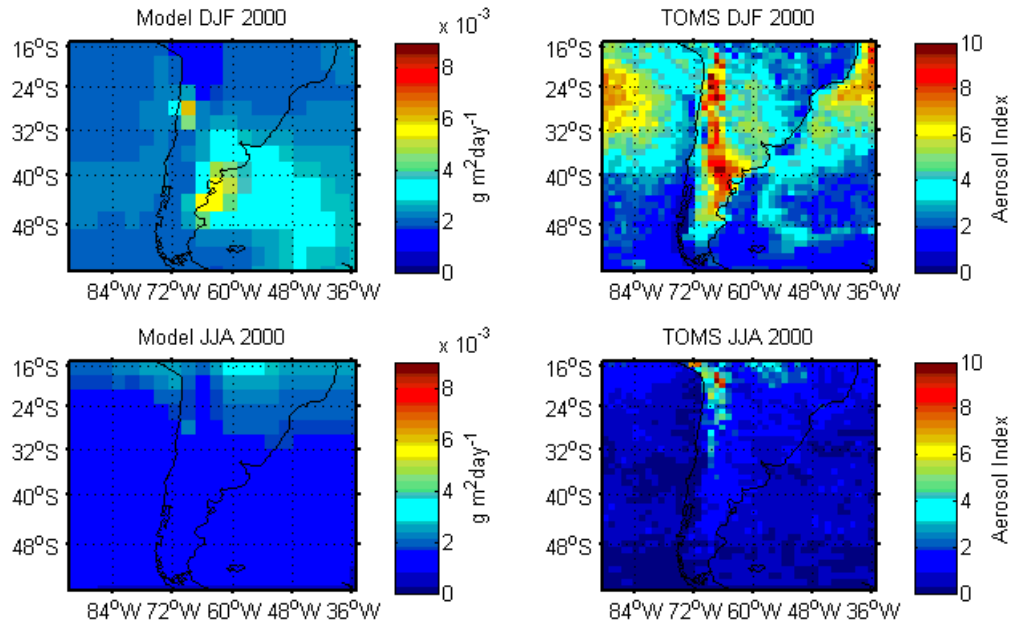

Figure 4-4 Comparison of dust modelled loading from Patagonia in DJF and JJA and TOMS AI data. Increased dust activity is seen in DJF in the model and the TOMS data.

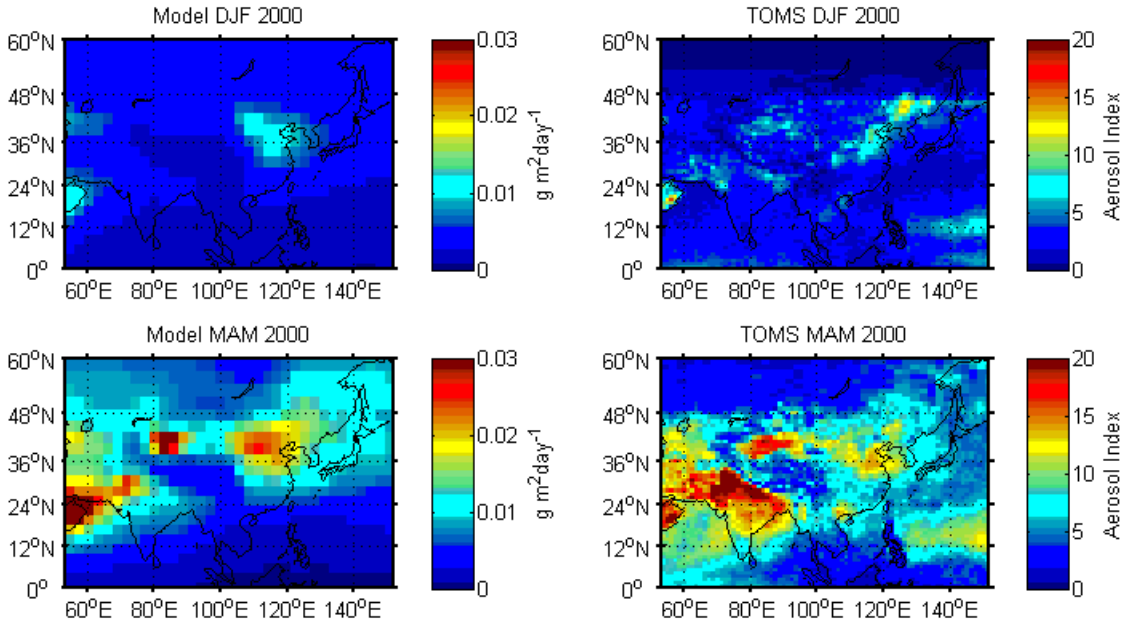

Figure 4-5 Comparison of simulated total column dust loading with TOMS AI over Asia in DJF and MAM.

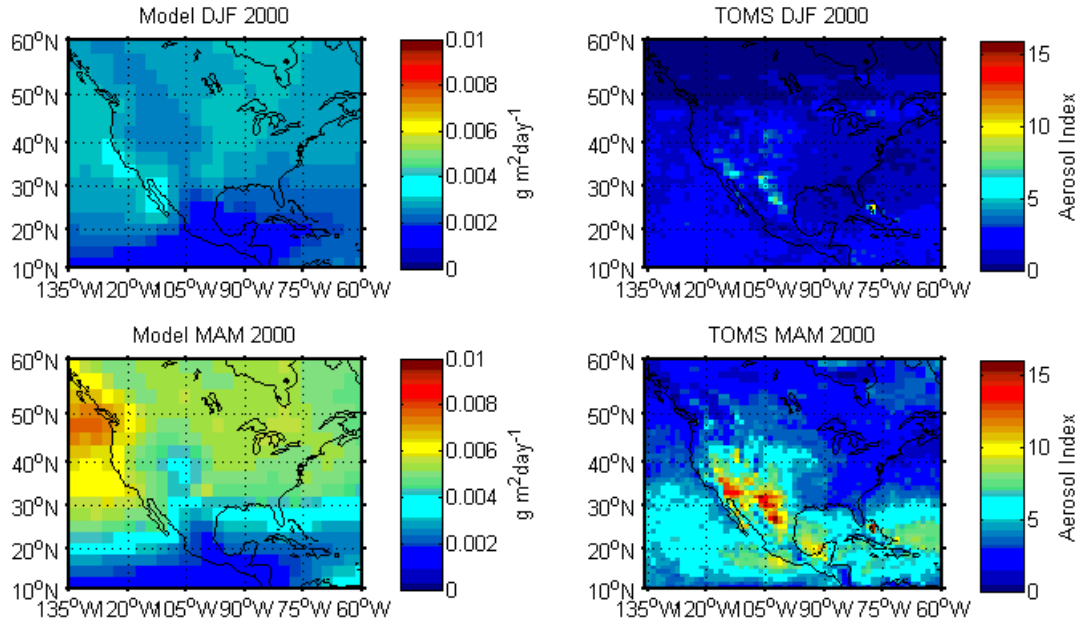

Figure 4-6 Comparison of simulated total column dust loading with TOMS AI over North America in DJF and MAM.

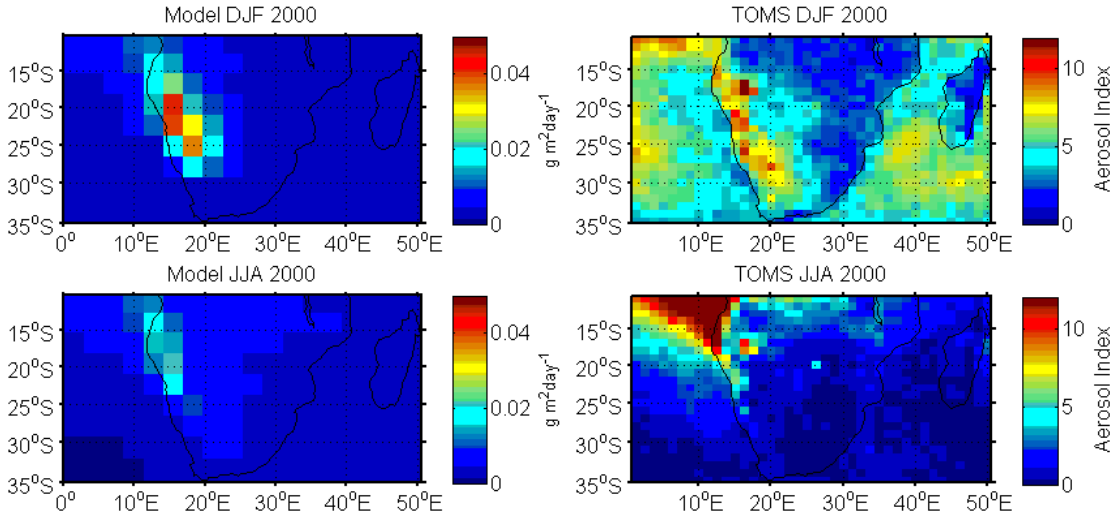

Figure 4-7 Comparison of simulated total column dust loading with TOMS AI over South Africa in JJA and DJF.

4.2.2 Simulated surface concentrations: Comparison with measurements

The comparison with the remote sensing data in the previous section provided a qualitative assessment of how well the model predicts seasonality in the dust loading. In this section a

quantitative evaluation is carried out. The simulated surface concentrations are compared to measurement data from the University of Miami aerosol network. The locations of the sites in the network are shown in Figure 4-8. The correlation coefficients between the simulated monthly mean surface concentrations and the measurements are listed in Table 4-1. The measured and modelled surface concentrations are shown in Figure 4-9. Note that the simulated surface concentrations have been scaled in Figure 4-9 so that the seasonality can be seen more easily. To scale the data the modelled surface concentrations have been divided by a scale factor (shown in the plots) so that the mean modelled data matches the mean measurement data. The un-scaled data is shown in Figure 4-10.

It can be seen from Figure 4-9 that the model is successful at predicting the timing of the maximum dust concentrations in JJA at Bermuda (r=0.9), Miami (r=0.87) and Barbados (r=0.84). At Mace Head the model is unable to reproduce the observed seasonality in surface concentrations (r=0.13). Measurements at Mace Head are only taken when the prevailing wind is from the west. This is to minimise contamination from local sources. North African dust is likely to arrive at the site from the East. It is possible that not all North African dust arriving at the site is sampled, which may also explain why the model estimates are 9 times higher than the measurements.

The model under predicts the maximum concentrations in JJA at Izana in Tenerife (r=-0.10). This site is close to the Saharan source. The poor correlation may be because the measurements are taken at an altitude of 2360m which corresponds to eight model levels above the surface in TOMCAT.

At sites in the Pacific which are affected by Asian dust emissions the model is successful at predicting the maximum surface concentrations in spring at Funafuti (r=0.9), Hedo (r=0.79), Midway Island (r=0.55), Enewtak (0.51). At Cheju the correlation coefficient is low (r=0.3) but the model is able to predict the increase in dust concentrations in the spring.

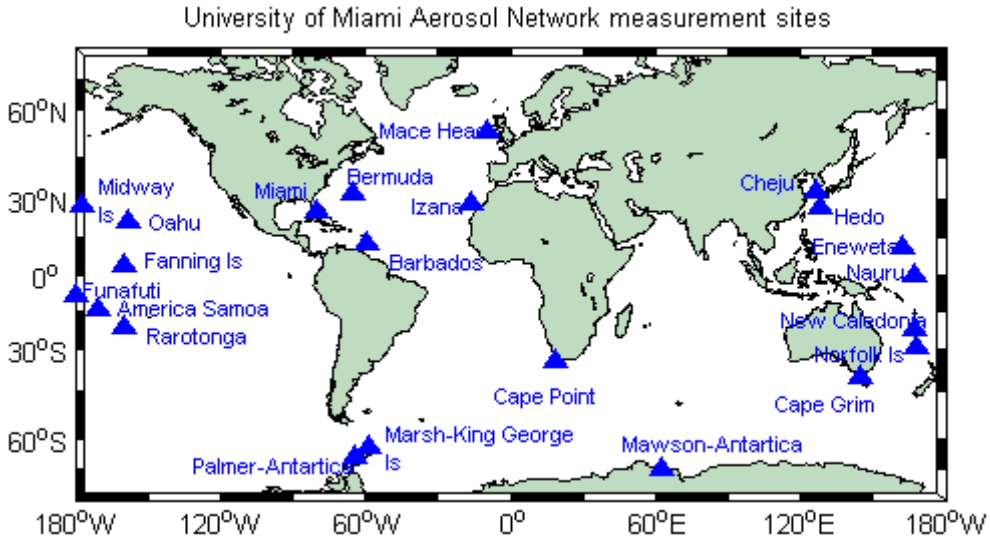

Figure 4-8 The location of sites in the University of Miami aerosol network where monthly surface concentration data is available.

At Nauru and Fanning Island, the model is unable to predict the spring maximum in surface concentrations seen in the measurements, but instead predicts a peak in August which is typical of the North African dust signal. The model over predicts the surface concentrations by a factor of 37 and 56 at these sites respectively. Returning to Figure 4-1 it can be seen that in JJA some North African dust crosses the US to the northern Pacific. This suggests that the model over estimates the transport of North African dust to the Pacific. This may be caused by an underestimate of the amount of dust removed by wet deposition. A similar seasonal cycle in surface concentrations at Fanning Island was found in the work of Tegen et al., (2002) although no explanation was put forward for this.

At Mawson in Antarctica the model predicts that maximum concentrations occur in the DJF which is consistent with the measurements. This agrees with the maximum in surface emissions coming off Patagonia (see Figure 4-4) which contributes to the dust measured at Mawson. At the other two Antarctic sites (Marsh-King George Island and Palmer) the modelled seasonality is poor.

The measurements sites at New Caledonia and Norfolk Island, Cape Grim, America Samoa and Rarotonga are influenced by Australian dust emissions and the model is unable to predict the peak in surface concentrations observed in January-February at the majority of these sites. Instead, the model predicts that the maximum surface concentrations occur

between August and December. This is coincides with when LPJ predicts the timing of the minimum vegetation cover which is incorrect, as discussed in section 4.2.

Figure 4-10 shows a comparison between the simulated surface concentrations and measurements when the modelled data is un-scaled. At North Atlantic sites (Bermuda, Barbados and Miami) the model predicts the magnitude of the surfaces concentration well. The measurements lie within the standard deviation of the model estimates. The fact that the model predicts the magnitude of the surface concentrations well at Barbados is significant for the work carried out in chapter 5. This chapter investigates if decadal scale changes in vegetation cover in the Sahel can explain the variability in dust concentrations measured at Barbados.

At sites close to the Asia source (Cheju and Hedo) the model is successful at predicting the magnitude of the surface concentrations. However, the model overestimates concentrations at sites in the remote Pacific (Oahu, Midway Island and Enwetak).
Figure 4-9 shows that concentrations at these sites are over predicted by a factor of 15-30.

To summarise, the key findings of the comparison with the TOMS aerosol index data and the surface concentration measurements;

i. The model is successful at predicting the maximum in dust emissions from North Africa in JJA, in South America in DJF, in South Africa in DJF, in Asia in MAM and North America in MAM.

ii. In Australia, the model predicts the timing of the maximum emissions between August and December rather than in DJF. This coincides with when LPJ predicts the timing of the minimum vegetation cover.

iii. The model is able to predict the magnitude of the surface concentrations at sites influenced by North African dust and at sites close to the Asian source but overestimates the magnitude of the surface concentrations at sites in the remote Pacific by a factor of 15-30.

Site location	*Correlation coefficient*
Bermuda 32.27N 64.87W	0.90
Funafuti 8.5S 179.20W	0.90
Miami 25.75N 80.25W	0.87
Barbados 13.17N 59.43W	0.84
Mawson - Antarctica 67.60S 62.50E	0.80
Hedo Japan 26.92N 128.25E	0.79
Yate–New Caledonia 22.15°S 167.00°E	0.65
Midway Island 28.22N 177.35W	0.55
Cape Point 34.35S 18.48E	0.54
Enewtak 11.33N 162.33E	0.51
Norfolk Island 29.08S 167.98E	0.39
Cheju 33.52N 125.48E	0.30
Oahu 21.33N 157.7W	0.16
Mace Head 53.32N 9.85W	0.13
Marsh-King George Island 62.18S 58.3W	0.06
Rarotonga 21.25S 159.75W	-0.04
Izana 28.30N 16.5W	-0.10
Palmer - Antarctica 64.77S 64.05W	-0.21
Nauru 0.53S 166.95E	-0.27
Fanning Island 3.92N 159.33W	-0.34
Cape Grim 40.68S 144.68E	-0.47
American Samoa 14.25S 170.58W	-0.68

Table 4-1 Correlation coefficients between the simulated monthly mean surface concentrations and measurements from the university of Miami aerosol network. The sites are listed in order highest of correlation coefficient.

4.3 Determining the cause of seasonality in the dust cycle

The previous section showed that the LPJ-dust model did a reasonably good job predicting the seasonality in the dust loading and in surface concentrations in most regions with the exception of Australia. Now the model can be used to address the question of which processes control the seasonality in the dust cycle. Five sensitivity experiments are carried out to examine the influence of vegetation cover, soil moisture, snow cover, surface wind speeds and wet deposition on the seasonality of the dust cycle. In each sensitivity experiment, the factor concerned is held constant at its mean annual value, while all other factors are allowed to vary seasonally. To calculate the seasonally invariant wet deposition, the model is run using annual mean convective precipitation, large scale precipitation, low cloud and medium cloud amounts. The annual mean values have been calculated from the 6 hourly ERA-40 reanalysis data.

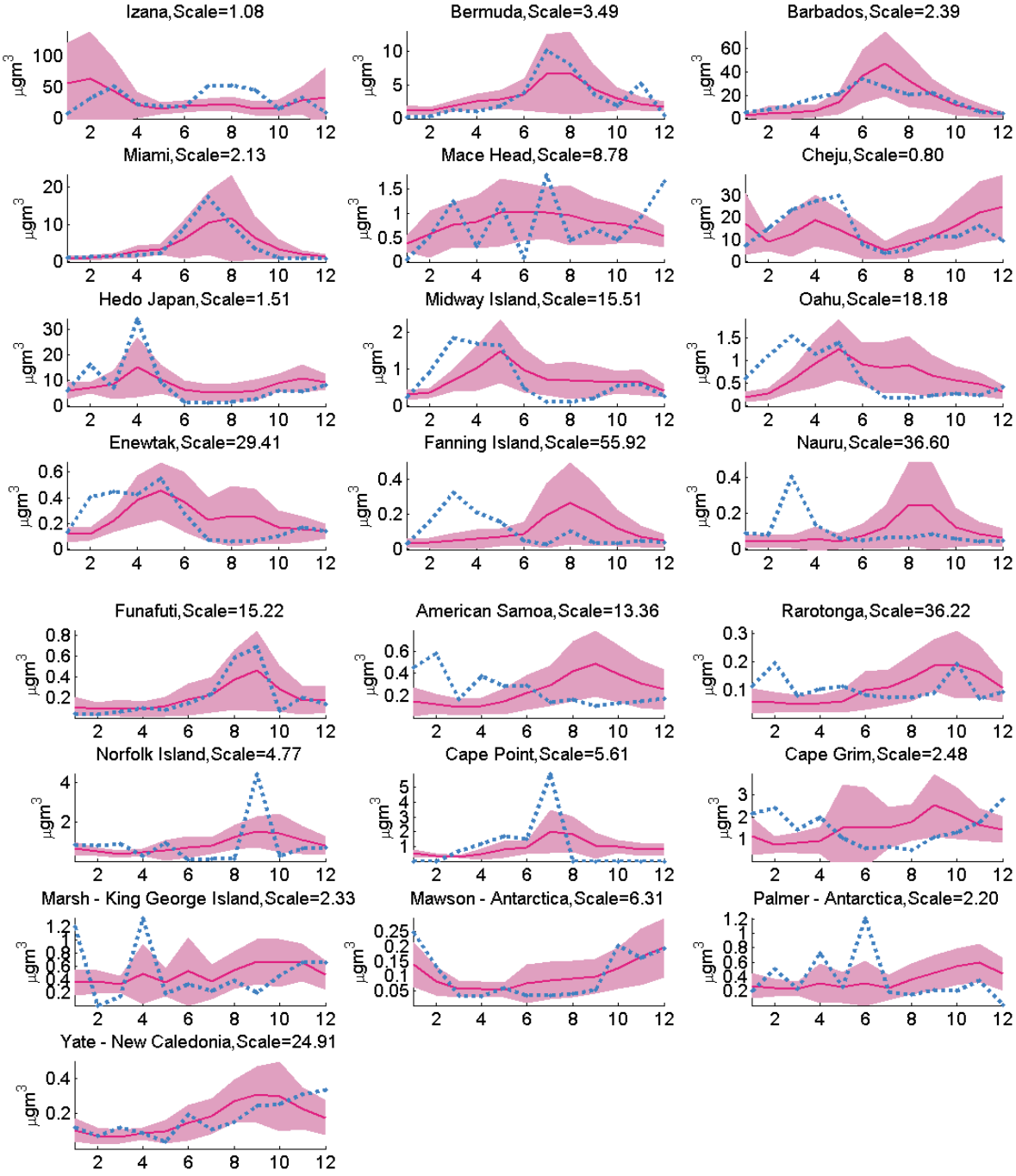

Figure 4-9 Comparison between the simulated monthly mean surface concentrations and measurements from the University of Miami aerosol network. The pink line is the mean modelled surface concentrations over the period 1990-2000. The pink shaded area corresponds to the standard deviation of the modelled mean over the period 1990-2000. The blue dashed line denotes the measurements. Note the data has been scaled.

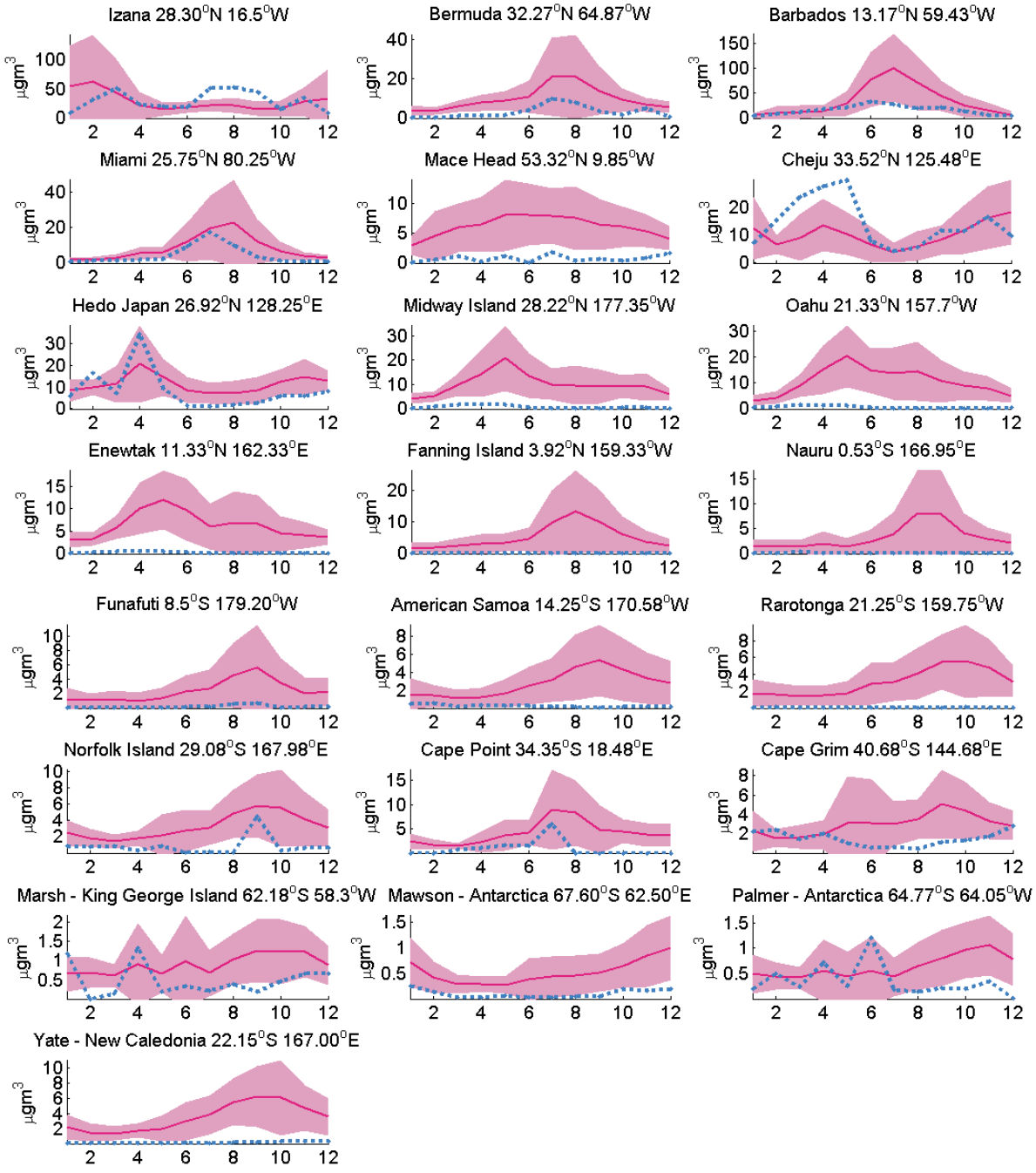

Figure 4-10 Comparison between the simulated surface concentrations and measurements from the University of Miami aerosol network. The plot is the same as Figure 4-9. This time, however, the data has not been scaled.

The experiment described in section 4.1 is used as the control experiment. The sensitivity experiments are run for the same simulation period (1990-2000) as the control experiment.

Two experiments were run to test the impact of seasonal changes in surface wind speeds on the dust loading. In the first experiment the surface emissions are generated using July ERA-40 10m wind speeds of each year while all other parameters in the model are allowed to vary seasonally. This is repeated using January ERA-40 10m wind speed data. The purpose of repeating the experiments using January and July wind speeds is so the model is forced by summer/winter wind speeds for the Northern and Southern Hemisphere.

The analyses of the results are divided into three sections. The first section aims to understand the cause of seasonal variability in surface emissions. The second aims to understand the cause of seasonality variability in the dust loading after transport has taken place. The third section investigates which processes are responsible for the seasonality in the surface concentration measurements used in section 4.2.2 to validate the model.

4.3.1 Seasonality in surface emissions

This section analyses the experiments which use seasonally invariant vegetation cover, soil moisture, snow cover and surface wind speeds. These experiments are selected because these processes are used to calculate surface emissions in the model. For each sensitivity experiment, the monthly surface emissions are averaged over the years 1990-2000. The timing of the year when the surface emissions have a maximum value is plotted and discussed.

To help gain a better understanding of the processes which cause the seasonality in the emissions the ERA-40 wind speed and precipitation over selected dust producing regions is also analysed. The selected regions of study are; the Sahara, the Sahel, China and Mongolia, Central Asia, South West Asia, North Africa, South America and South Africa.

Three parameters are calculated for the analysis. Firstly, the monthly mean precipitation is calculated from the ERA-40 6 hourly large scale and convective precipitation. This is then averaged over each region.

Secondly, the number of times in a month when the wind speed exceeds a minimum threshold for dust emissions is calculated from the 6 hourly wind speeds. This is summed over each region. The chosen minimum threshold friction velocity for dust emissions is $2ms^{-1}$. This corresponds to the wind speed required to mobilise a particle with diameter of 72μm. Higher wind speeds are required to mobilise larger and smaller particles (see Figure 1-1). In the case of larger particles, a higher threshold velocity is required because more energy is needed to overcome the force of gravity. A higher threshold friction velocity is required for smaller particles because of strong inter-particle cohesion forces. It was found that using the number of wind events greater than $2ms^{-1}$ was more informative than using mean wind speeds. This is because periods when wind speeds exceed the threshold limit for emissions are averaged out.

Thirdly, the monthly mean emissions are summed over the selected regions. The three parameters are calculated for each region for the years 1990 to 2000 and averaged. The correlation coefficients between the monthly dust emissions, the number of times the wind speeds exceed $2ms^{-1}$ and the monthly mean precipitation are listed in Table 4-2. The table also includes the months when the model predicts highest emissions and the months when dust storm frequency is highest. The dust storm data is taken from Table 4.7 in Goudie (2006) and is based on multiple observational studies of dust storms over different regions.

Figure 4-11 shows the timing of the maximum surface emissions for each experiment over North Africa and the Arabian Peninsula. The control experiment shows that maximum emissions occur between January and July depending on which region is examined. Seasonal changes in wind speeds are responsible for the timing of the maximum emissions over most of North Africa, the Arabian Peninsula and Ethiopia, as can be seen by comparing the seasonally invariant wind speed experiments to the control.

As expected, snow cover has no effect on the timing of the surface emission because no snow falls in this region. Soil moisture affects the timing of maximum emissions in the eastern Sahel at longitudes greater then $30^{o}E$.

The number of wind events greater then $2ms^{-1}$, the monthly mean precipitation and emissions over the Sahara is plotted in Figure 4-12. The maximum emissions in the Sahara occur between March and August. This coincides with months when the number of wind speed events greater than $2ms^{-1}$ is high.

It has been hypothesised by Engelstaedter et al., (2006) that the increase in emissions during JJA in North Africa is caused by an increase in wind speeds resulting from the North-South movement of the ITCZ. In JJA, the ITCZ moves northwards between 15^{o}N-23^{o}N and retreats back southwards during DJF. It was proposed that the crossing of the convergence belt may enhance the frequency of deep convention which increases surface wind speeds, resulting in more emissions.

Figure 4-13 shows the number of wind events greater than 2ms^{-1}, the monthly precipitation and emissions over the Sahel. The emissions are highest in May just before the monsoon season which commences in June. The high precipitation rates between June and September are caused by the northwards movement of the ITCZ which brings rainfall to the Sahel. A study by Engelstaedter et al., (2006) showed using TOMS AI data and precipitation data that rainfall during the Monsoon season reduces dust emissions. From Table 4-2 it can be see that dust emissions are correlated with wind speeds (r=0.84) and anti-correlated with precipitation (r=-0.68) which indicates that both processes are possibly important in determining the seasonality in dust emissions from the Sahel.

Figure 4-14 shows the timing of the maximum surface emissions over Asia. Broadly speaking there are three areas where dust emissions occur in Asia; China and Mongolia, Southwest Asia (Afghanistan, Pakistan and India) and Central Asia (Caspian Sea and Aral Sea regions). The factors that control the timing of the maximum dust activity are different for each region.

In Mongolia and China, Figure 4-14 shows that the dominant factor that controls the timing of the peak emissions in spring is the wind speeds. Vegetation cover does not appear to exert a strong control on the timing of the maximum emissions in this region, although a small impact is observed in Eastern Asia in which the control experiment shows emissions in March and April, but the seasonally invariant FPAR experiment shows no emissions.

	Correlation with wind events >2ms^{-1}	Correlation with precipitation	Timing of maximum emissions	Maximum dust storm frequency (Goudie 2006)
Patagonia	-0.24	-0.70	Nov-Jan	-
China & Mongolia	0.56	0.04	Mar-May	April-May (Mongolia)
Sahara	0.59	-0.48	Apr-Jun	Apr-Aug
Sahel	0.84	-0.68	Feb-Apr	Nov-Mar
Central Asia	0.60	-0.54	Jul-Aug	May-Aug (Kazakhstan)
North America	0.59	0.22	Mar-May	Mar-May
South West Asia	0.67	0.49	May-Jul	May-Sep(Afghanistan)
South Africa	0.17	0.33	Oct-Nov	Aug-Nov (Namibia)

Table 4-2 Column 2 lists the correlation coefficients between monthly emissions summed over each region and the number of times the ERA-40 wind speeds exceed 2ms^{-1} summed over each region. Column 3 lists the correlation coefficients between the monthly emissions summed over each region and the ERA-40 monthly mean precipitation averaged over the region. The period when the model predicts maximum emissions is listed in column 4. Column 5 lists the timing of maximum dust storm activity compiled by Goudie (2006) from multiple observational studies.

The seasonality in snow cover causes maximum emissions at the boundary of the Taklimakan desert in December which would otherwise occur in March-April.

Figure 4-15 shows that the maximum emissions in China and Mongolia in MAM coincide with an increase in the number of wind speeds greater then 2ms^{-1} and occurs just before JJA which brings rainfall to the region. A positive correlation (r=0.56) is found between the emissions and the number of times the wind speed exceeds 2ms^{-1}. The correlation with wind speeds is in agreement with previous studies that have found the peak in dust storm activity in Asia is caused by cold fronts from Siberia which caused high wind speeds over China and Mongolia (Littmann 1991; Goudie and Middleton 1992). Husar et al.,(2001) studied the metrological conditions that contributed to two extreme spring time dust events in Asia and found that the low pressure cold fronts traversing Mongolia and China caused major storms which resulted in wind speeds in excess of 20ms^{-1}.

Figure 4-14 shows that in Southwest Asia, greatest activity occurs in May and June. Wind speeds and soil moisture influenced the seasonality in emissions. It can be seen in Figure 4-16 that the maximum emissions occur in May-June after many months of low precipitation. The summer monsoon in July–August results in a sharp drop in dust emissions as precipitation increases the soil moisture. Another factor that increases the dust emissions in this region is the occurrence of thunderstorms. The highest thunderstorm

activity occurs during the summer monsoon season but there is also activity in May–June prior to the onset of the monsoon. This can be seen in the increase in the number of times the wind speeds exceed $2ms^{-1}$ in May-June.

In Central Asia in the area to the south of the Aral Sea, the timing of the maximum emissions in November-December is controlled by wind speeds as can be seen from Figure 4-14. To the north of the Aral Sea the presence of vegetation cover causes the maximum emissions to occur in November-December. This can be explained by the fact that the model simulates dry grasses in this region (see Figure 2-7). Dry grasses vary seasonally in the model which causes a contraction and expansion of the dust source area. The minimum vegetation cover in this region occurs in December (See Figure 2-3) which coincides with the timing of the maximum emissions.

To the north of the Aral Sea the seasonality in snow cover contributes to the timing of the maximum emissions in November-December while soil moisture affects the timing of the emission to the north and the south of the Aral Sea. It can be seen in Figure 4-17 that the Caspian and Aral Sea region emits dust continuously between April and December. The decrease in precipitation between May–October sees a corresponding increase in dust emissions.

There are very few observational studies of dust storm frequencies in the Caspian and Aral Sea regions. TOMS AI data shows that the dust activity in this region starts in May and reaches a peak in June-July (Prospero et al. 2002). The model predicts a maximum activity in November–December which is different to the TOMS AI. A possible explanation for the disparity is that this region is affected by human activity (Prospero et al. 2002). During World War II the Amu Darya River which feeds into the Aral Sea was dammed, causing the Aral Sea to shrink, exposing large areas of sediments to erosion. It has been suggested by Prospero et al (2002) the TOMS AI detects dust emission from the dried out lake bed.

In South America Figure 4-18 shows the area of most dust activity is concentrated around Patagonia. The maximum emissions occur in December and are controlled by soil moisture. This result is consistent with the findings of Lunt and Values (2002) who carried out sensitivity studies with a dust cycle model and found that Patagonian dust emissions were sensitive to the choice of soil moisture threshold. Figure 4-19 shows that the wind speeds in Patagonia are persistently higher than $2ms^{-1}$ throughout the year. Maximum

emissions occur in NDJ when precipitation is low. Conversely there are low dust emissions between March and October when precipitation is high. Dust emissions are strongly anti-correlated (-0.70) with precipitation. The correlation with wind speeds is very low suggesting that the mechanism that controls the sensitivity in dust emission over Patagonia is precipitation, which in turn affects soil moisture.

Figure 4-21 shows the timing of the maximum emissions from North America. In the southern high plains (in North West Texas and eastern New Mexico) maximum activity occurs in April and is influenced by wind speeds, vegetation cover and soil moisture. This agrees with a study by Strout (2001) who carried out measurements of particulate mass with diameter less than 10μm (PM10) in Texas. It was found that the days with the highest PM10 concentrations occurred in spring and coincided with the frequency of winds greater $4ms^{-1}$. They also found that wind speeds alone were not a perfect indicator of dust concentrations and that low soil moisture during spring also contributed to the high concentrations. No soil moisture data was available for this region but it was inferred from relative humidity measurements. The study also showed that in spring vegetation cover was sparse, although the vegetation referred to in the study was cotton, which is not simulated in LPJ.

Figure 4-20 shows that maximum emissions over the North American occur in spring and coincide with a period when the number of times the wind speeds exceed $2ms^{-1}$ is high. A positive correlation of 0.59 is found between the wind speeds and the surface emissions. The results suggest that the seasonality in emissions in North America is controlled by the combination of vegetation cover, soil moisture and the frequency of wind speeds greater than $2ms^{-1}$.

In central South Africa the model predicts maximum dust activity in June-August as seen in Figure 4-22. Along the western coast, maximum emissions occur between December and January. Wind speeds contribute to the timing of the maximum emissions along the coastal regions and inland. Vegetation cover and soil moisture influence the timing of the emissions in the interior. LPJ predicts dry grass in the inland (Figure 2-7). This has a minimum in June-August (Figure 2-3) and coincides with the timing of the maximum emissions.

Figure 4-23 shows that increases in dust emission start in June and reach a maximum in November. This coincides with the months when the wind speeds most frequently exceed 2ms^{-1} and after many months of low precipitation. The correlation with wind speeds in South Africa is low overall (r=0.17). These results suggest that multiple environment factors control the seasonality in dust emissions from South Africa. Maximum emissions occur in inland in JJA due to the combined effect of low vegetation cover, low soil moisture and a high frequency of wind speeds greater then 2ms^{-1}

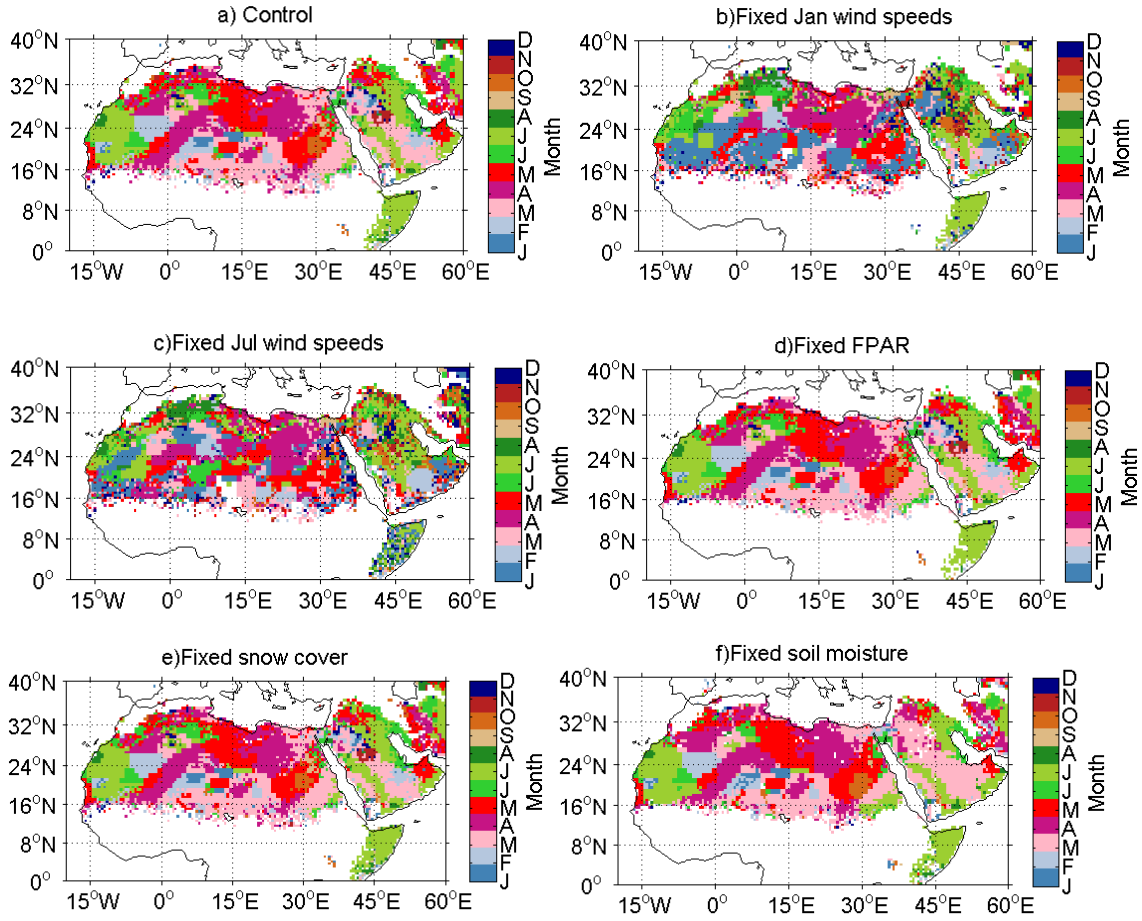

Figure 4-11 The timing of the maximum surface emission over North Africa and the Arabian peninsula for the control experiment and the sensitivity experiments

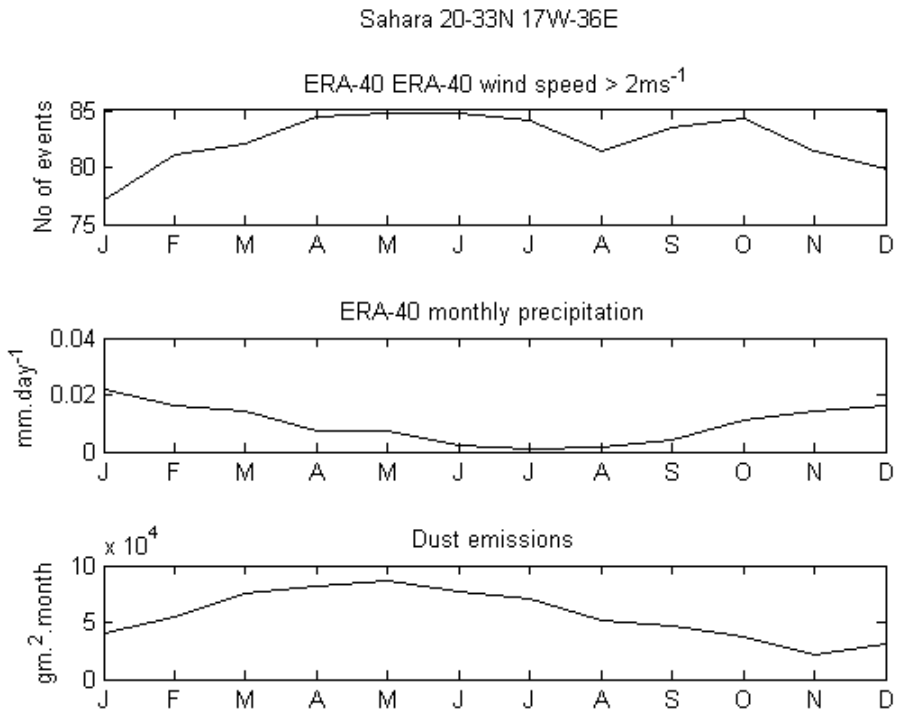

Figure 4-12 Monthly mean surface emissions, the number of times in a month the wind speeds exceed 2ms^{-1} and monthly precipitation data. The data has been averaged for the years 1990-2000 over the Sahara.

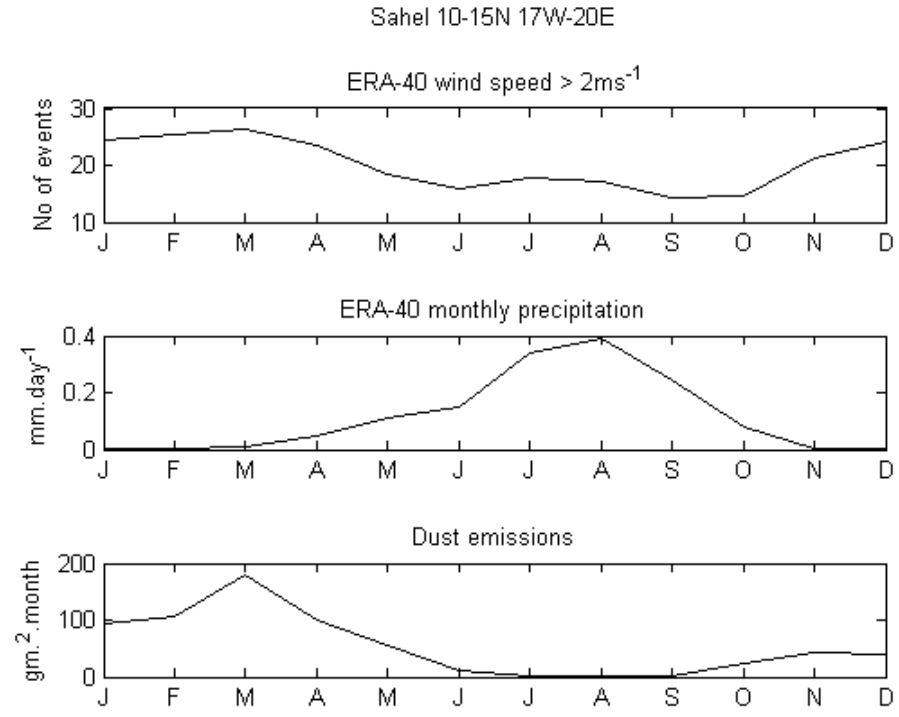

Figure 4-13 Monthly mean surface emissions, the number of times in a month the wind speeds exceed 2ms^{-1} and monthly precipitation data. The data has been averaged for the years 1990-2000 over the Sahel.

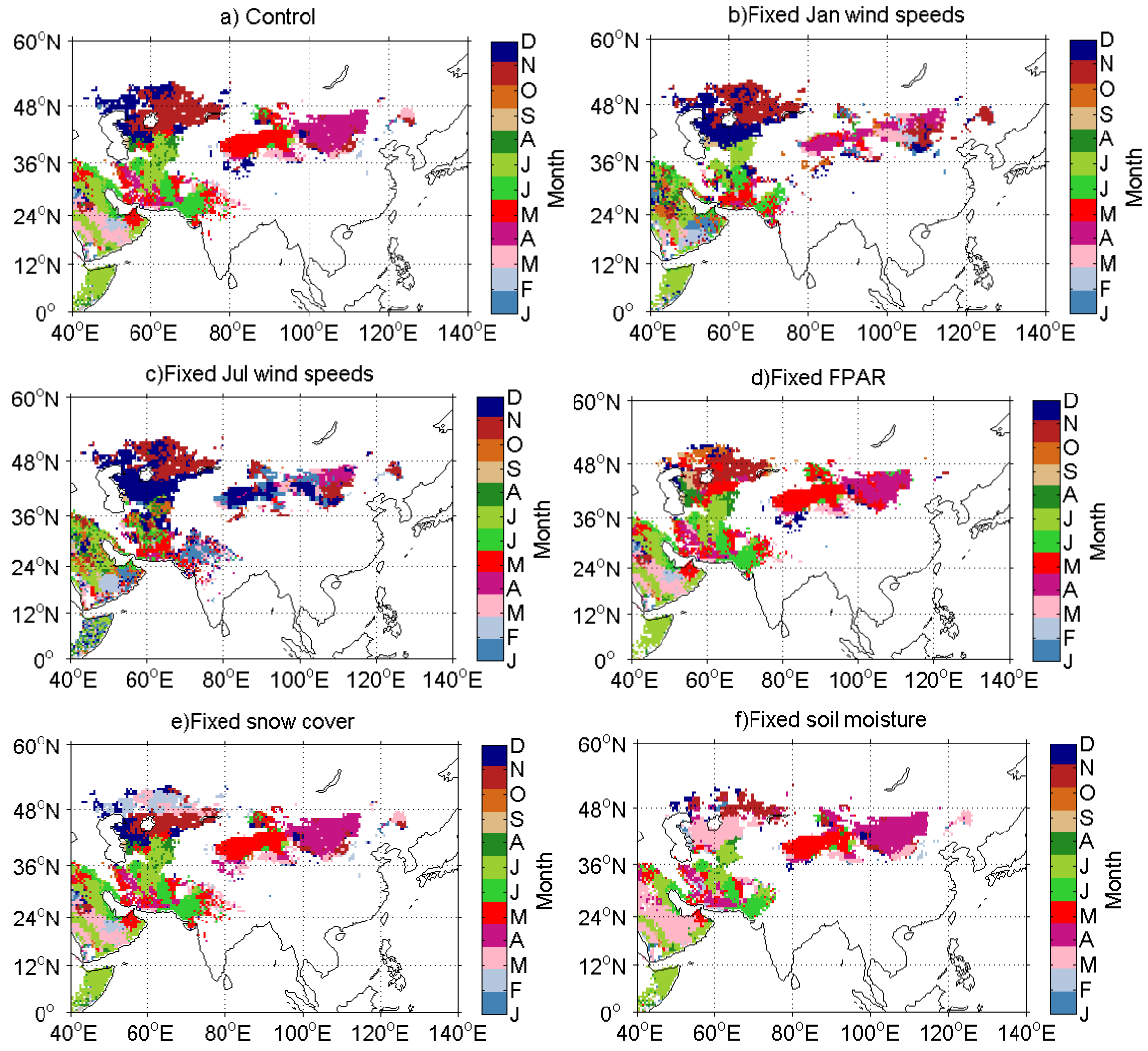

Figure 4-14 The timing of the maximum surface emissions over Asia for the control experiment and the sensitivity experiments.

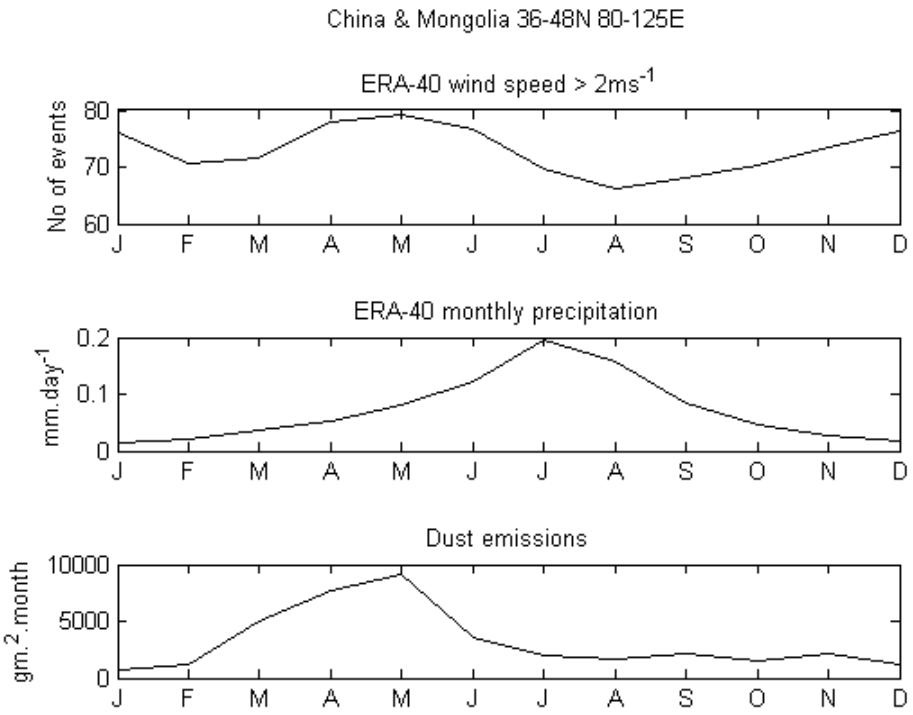

Figure 4-15 Monthly mean surface emissions, the number of times in a month the wind speeds exceed $2ms^{-1}$ and monthly precipitation data. The data has been averaged for the years 1990-2000 over China and Mongolia.

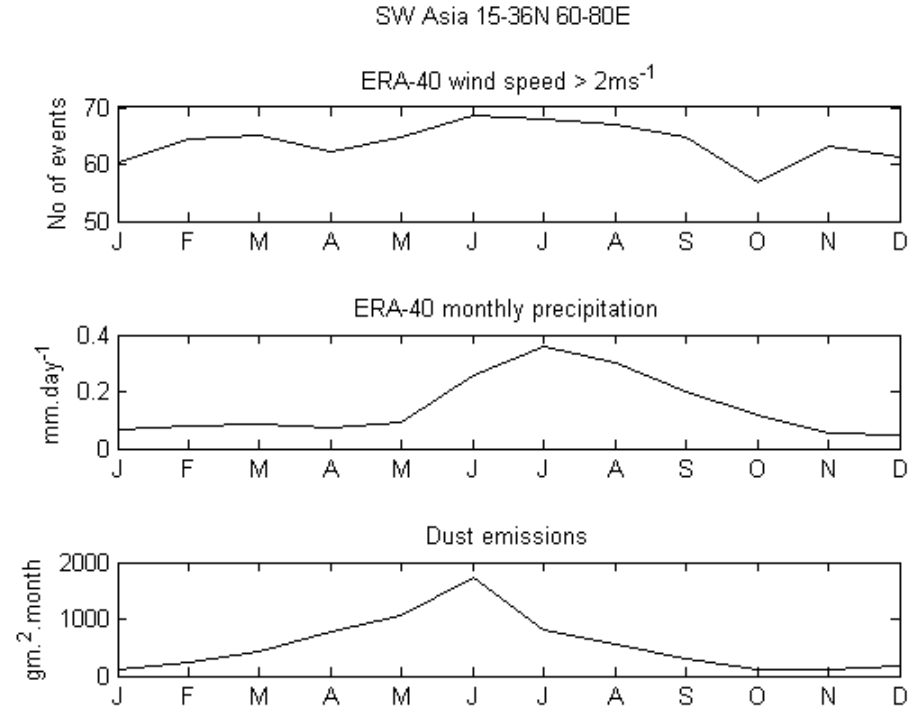

Figure 4-16 Monthly mean surface emissions, the number of times in a month the wind speeds exceed $2ms^{-1}$ and monthly precipitation data. The data has been averaged for the years 1990-2000 over the south west Asia.

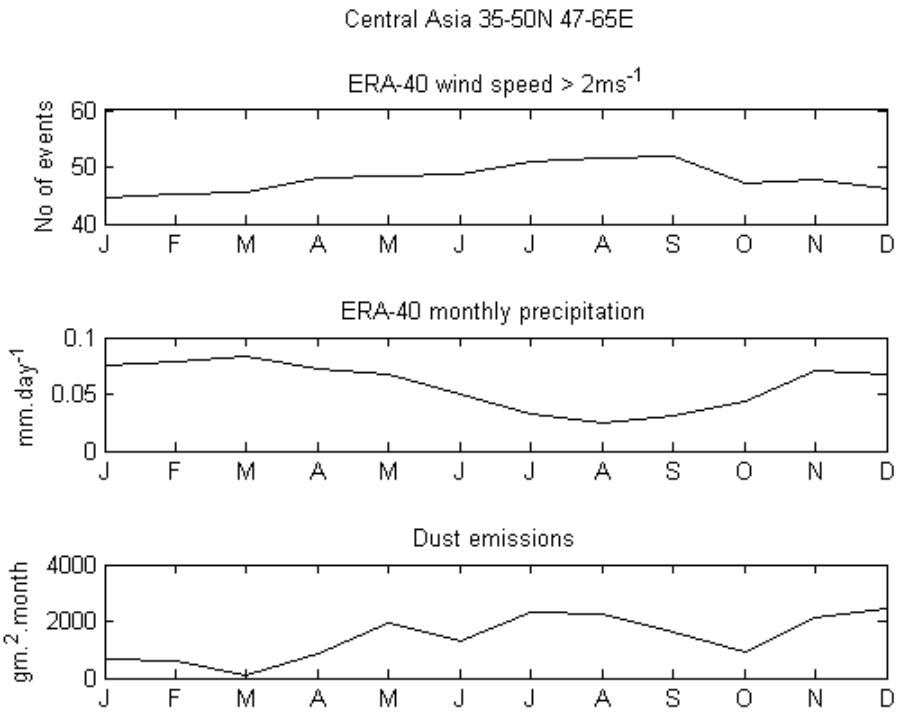

Figure 4-17 Monthly mean surface emissions, the number of times in a month the wind speeds exceed $2ms^{-1}$ and monthly precipitation data. The data has been averaged for the years 1990-2000 over central Asia.

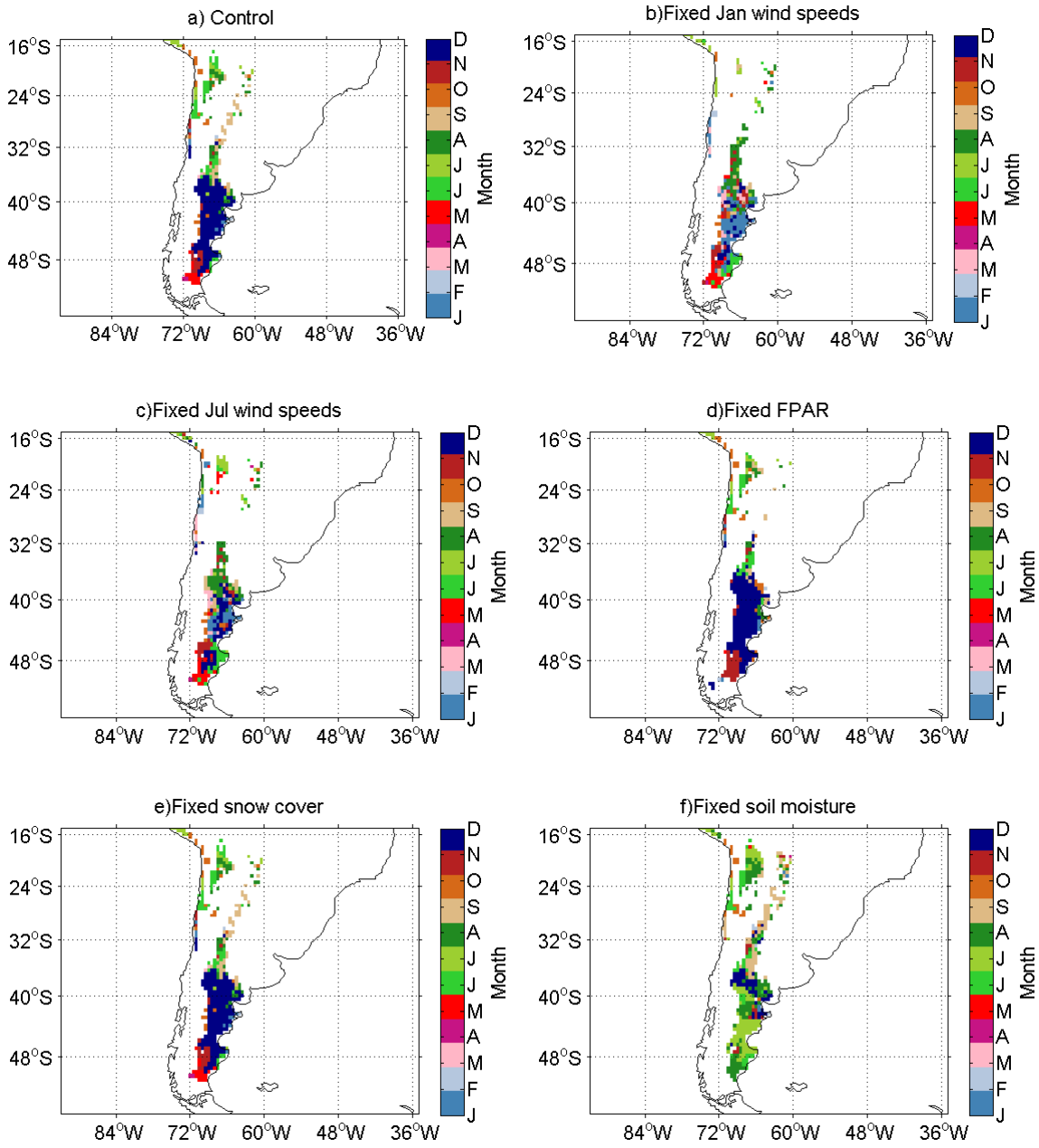

Figure 4-18 The timing of the maximum surface emission for South America for the control experiment and the sensitivity experiments.

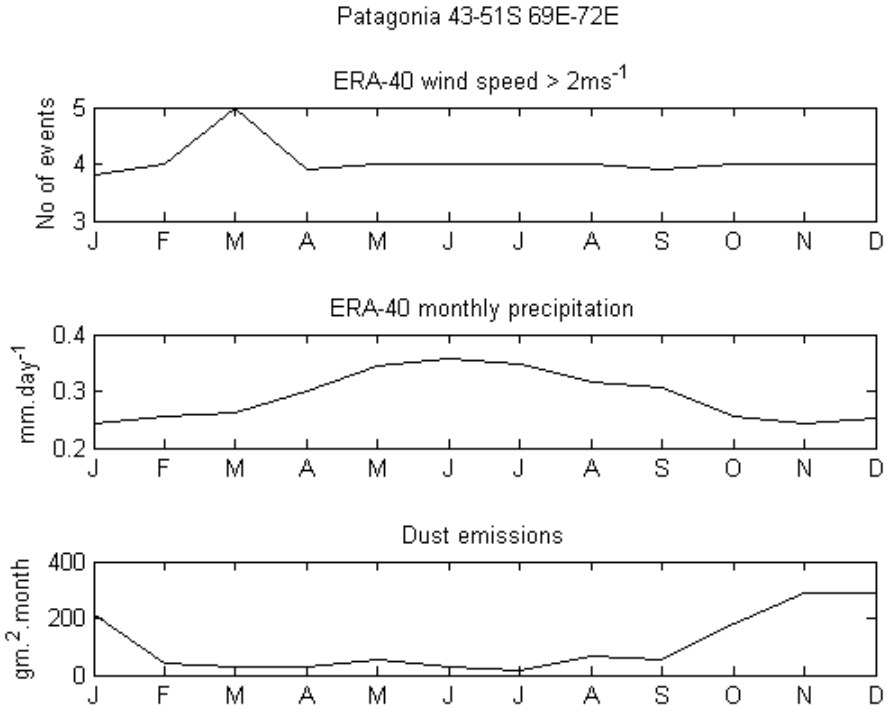

Figure 4-19 Monthly mean surface emissions, the number of times in a month the wind speeds exceed 2ms^{-1} and monthly precipitation data. The data has been averaged for the years 1990-2000 over Patagonia

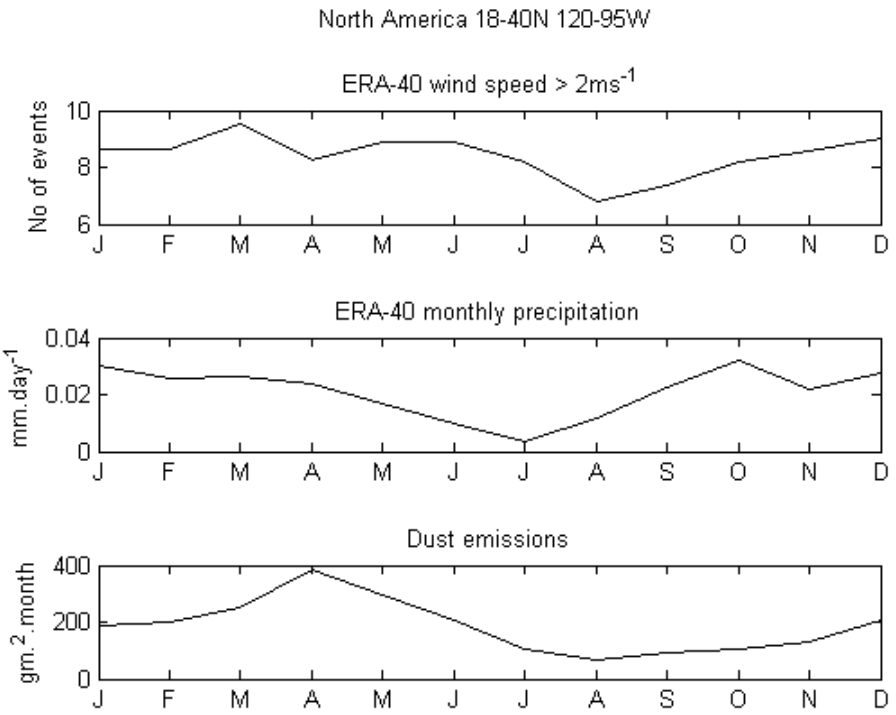

Figure 4-20 Monthly mean surface emissions, the number of times in a month the wind speeds exceed 2ms-1 and monthly precipitation data. The data has been averaged for the years 1990-2000 over North America.

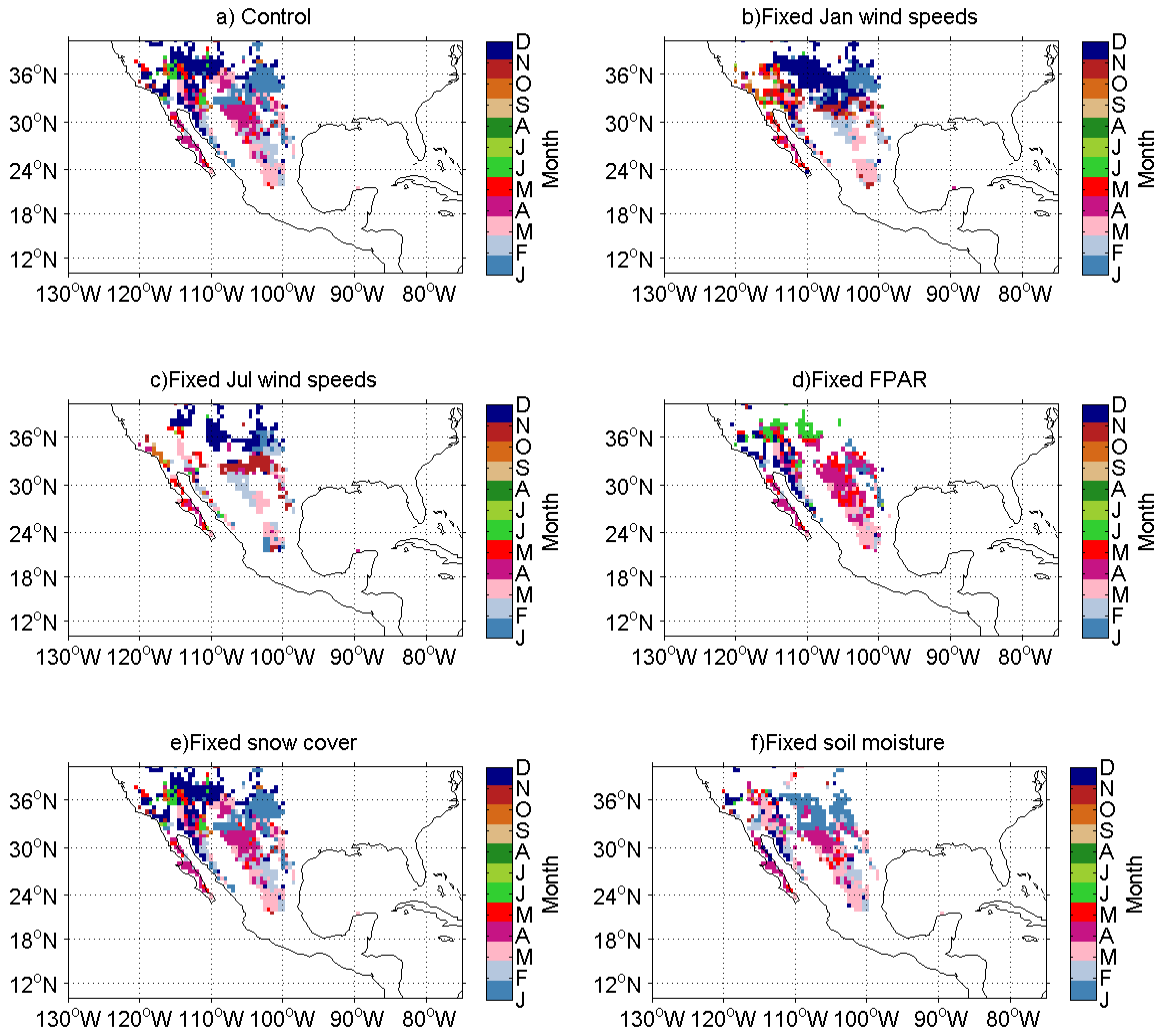

Figure 4-21 The timing of the maximum surface emissions over North America for the control experiment and the seasonality experiments.

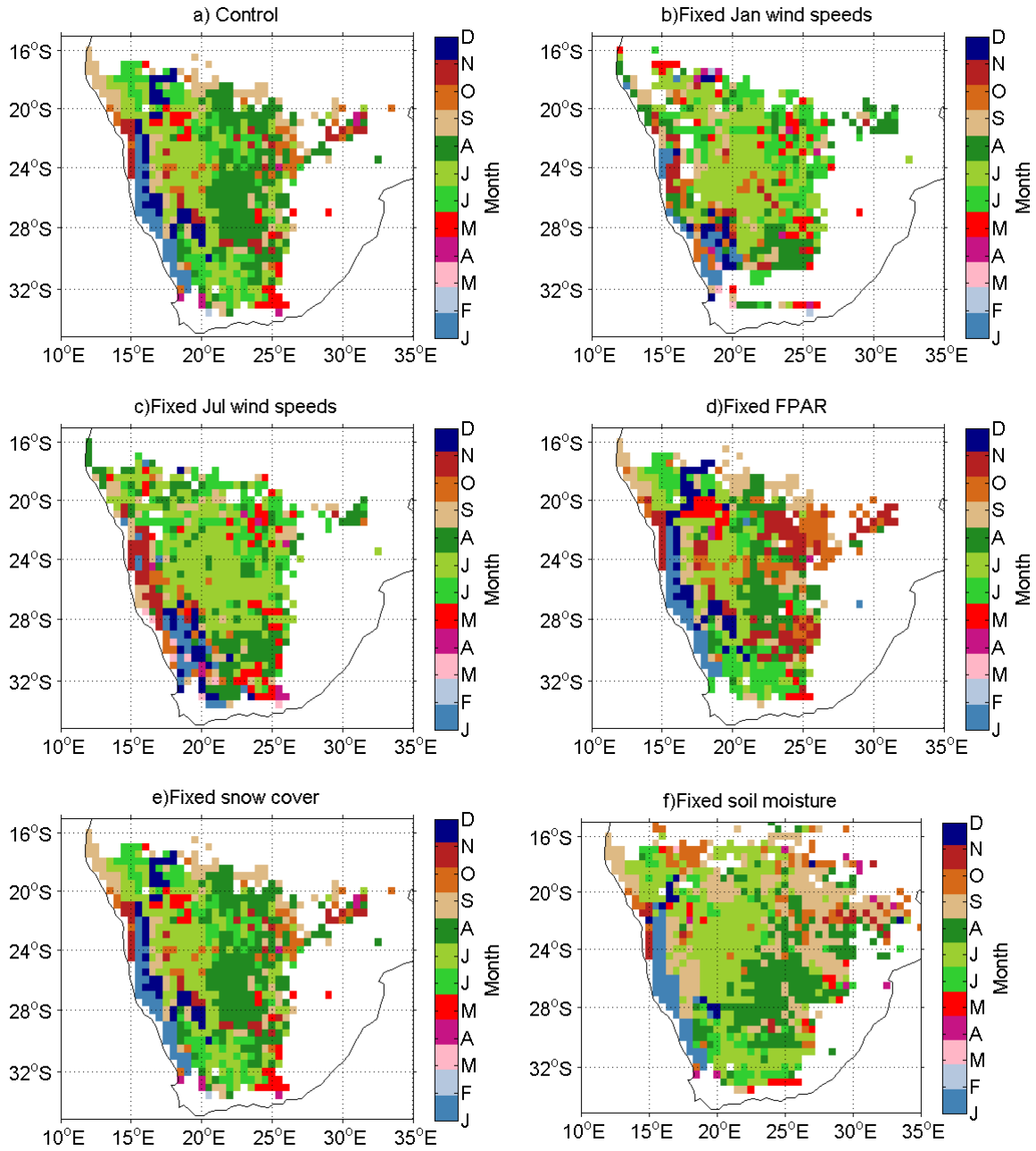

Figure 4-22 The timing of the maximum surface emissions over South Africa for the control experiments and the sensitivity experiments.

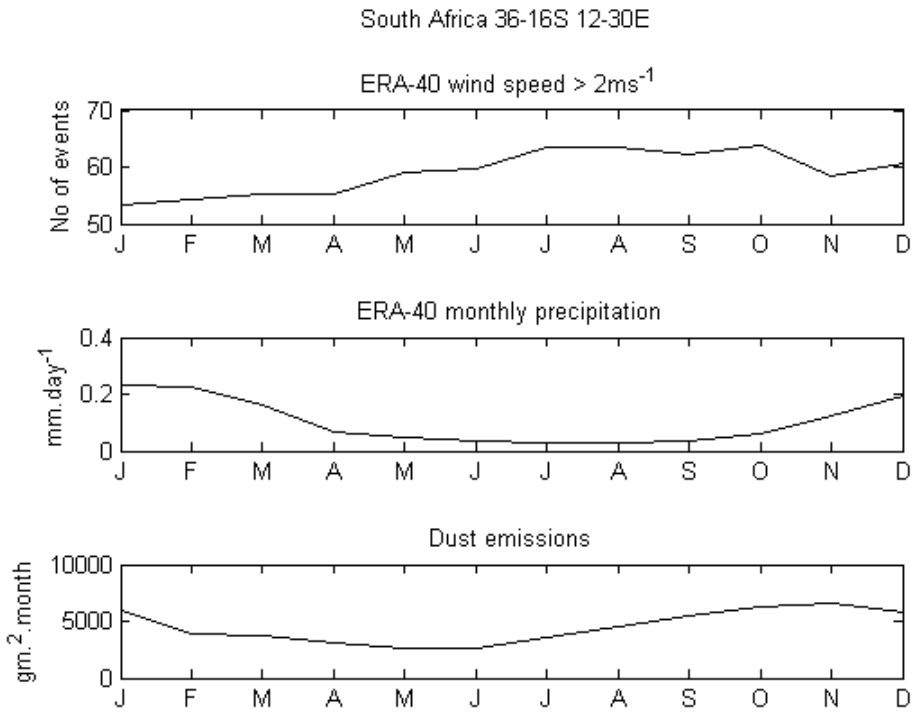

Figure 4-23 Monthly mean surface emissions, the number of times in a month the wind speeds exceed $2ms^{-1}$ and monthly precipitation data. The data has been averaged for the years 1990-2000 over South Africa.

4.3.2 Seasonality in the atmospheric dust loading

In this section the scope of the analysis is extended to understand which factors contribute to the seasonality in the dust loading after dust emissions have been transported from the source regions. Once again, Australia is excluded from the discussion because the model is unable to predict the seasonality correctly. Results are presented for experiments which use seasonally invariant wind speeds, vegetation cover, soil moisture, snow cover and wet deposition. The daily total column dust loading from each experiment is output for the years 1990-2000 and converted into monthly averages. These monthly averages were used to construct the monthly climatology over the years 1990-2000.

Figure 4-24 shows the timing of the maximum dust loading for the control experiment and the sensitivity experiments. The maximum dust loading in the control experiment at latitudes approximately greater then 30^{o}N occurs in April-May. The previous section saw that that peak emissions from China and Mongolia occurred in April-May. This indicates that the timing of the dust loading is caused by the dispersion of Asian dust.

When the surface emissions are calculated using January wind speeds, the timing of the maximum dust loading in the northern hemisphere over Russia, Greenland and in the Canadian Arctic occurs in December. This is because of an increase in the Southern Hemisphere dust sources caused when the model is forced with Southern Hemipshere summer winds. An increase in the Southern Hemisphere dust signal is also seen at latitudes below 0^{o}.

It can be seen that changes in FPAR do not have a very large affect on the timing of the total column dust loading globally. The effect is small and localised in over Eastern China and over the north west of the Caspian Sea. In the previous section vegetation cover was found to affect the timing of the maximum emission in these areas. Vegetation cover does not have an impact of the timing of the dust loading far from the source regions, although a small impact is observed in Northern Greenland and in Northern Russia.

Soil moisture affects the timing of the maximum total column loading over several regions. This can be seen in South Africa, central Asia and in the Sahel. Soil moisture strongly influences the timing of the minimum dust loading over Patagonia and this has an impact of the dust loading over the southern Atlantic Ocean.

The control experiment shows that maximum dust loading occurs in JJA over the North Atlantic. It is worth pointing out that North African dust is transported to the Pacific. This explains why dust concentrations at Nauru and Fanning Island were over estimated (see section 4.2.2) and why peak concentrations occurred in August, which is typical of the Saharan dust signal, rather than in March–April as the measurements show. This is another reason to suspect that the model overestimates the long range transport of North African dust.

Wet deposition does not have a strong effect on the timing of the maximum dust over North Africa because precipitation rates are very low. It does have an impact on the timing of maximum dust loading over eastern China and the Caspian Sea region. The seasonally invariant wet deposition experiment shows an increase in dust loading with a JJA maximum over the North Atlantic, the Arctic Ocean, north Russia and Alaska. To understand why this is, it is necessary to look to the next section. Figure 4-25 shows the simulated surface concentrations for the sensitivity experiments together with measurement data from the University of Miami aerosol network. The experiment which

Chapter 4: Determining the cause of seasonal variability in the global dust cycle uses seasonally invariant wet deposition results in much higher surface concentrations, indicating that less dust is removed from the atmosphere. Figure 4-24 (g) shows an increase in dust loading at high latitudes in the Northern Hemisphere with a maximum in JJA. This is consequence of less North African dust being removed by wet deposition.

A similar process is responsible for the increase in dust loading in the South Pacific which has a maximum in JJA. These results show that wet deposition controls the timing of the maximum dust loading at long distances from the source region.

4.3.3 Seasonality in dust concentrations

The model was validated using measurements of dust concentrations from the University of Miami aerosol network (section 4.2.2). This section aims to understand the cause of seasonality in these measurements. The monthly mean simulated surface concentrations predicted by the sensitivity experiments are compared to the measurement data. Only sites where the control experiment does a reasonably good job at predicting the surface concentrations are selected for the comparison. This was decided by choosing sites that have a correlation coefficient greater than 0.5 between the simulated surface concentrations and the measurements.

Figure 4-25 shows the monthly mean surface concentrations for the sensitivity experiments and the measurements for the selected sites. It can be seen that seasonal changes in vegetation cover, surface emissions, wind speeds, snow cover, soil moisture and wet deposition affect the magnitude of the surface concentrations, but not the timing of the maximum and minimum concentrations. This suggests that the timing of the minimum and maximum surface concentrations at these locations is controlled by transport processes.

The correlation coefficients between the simulated monthly mean surface concentrations for the sensitivity experiments and the measurements are listed in Table 4-3. The simulated surface concentrations at sites in the North Atlantic (Bermuda, Barbados and Miami) show no sensitivity to vegetation cover.

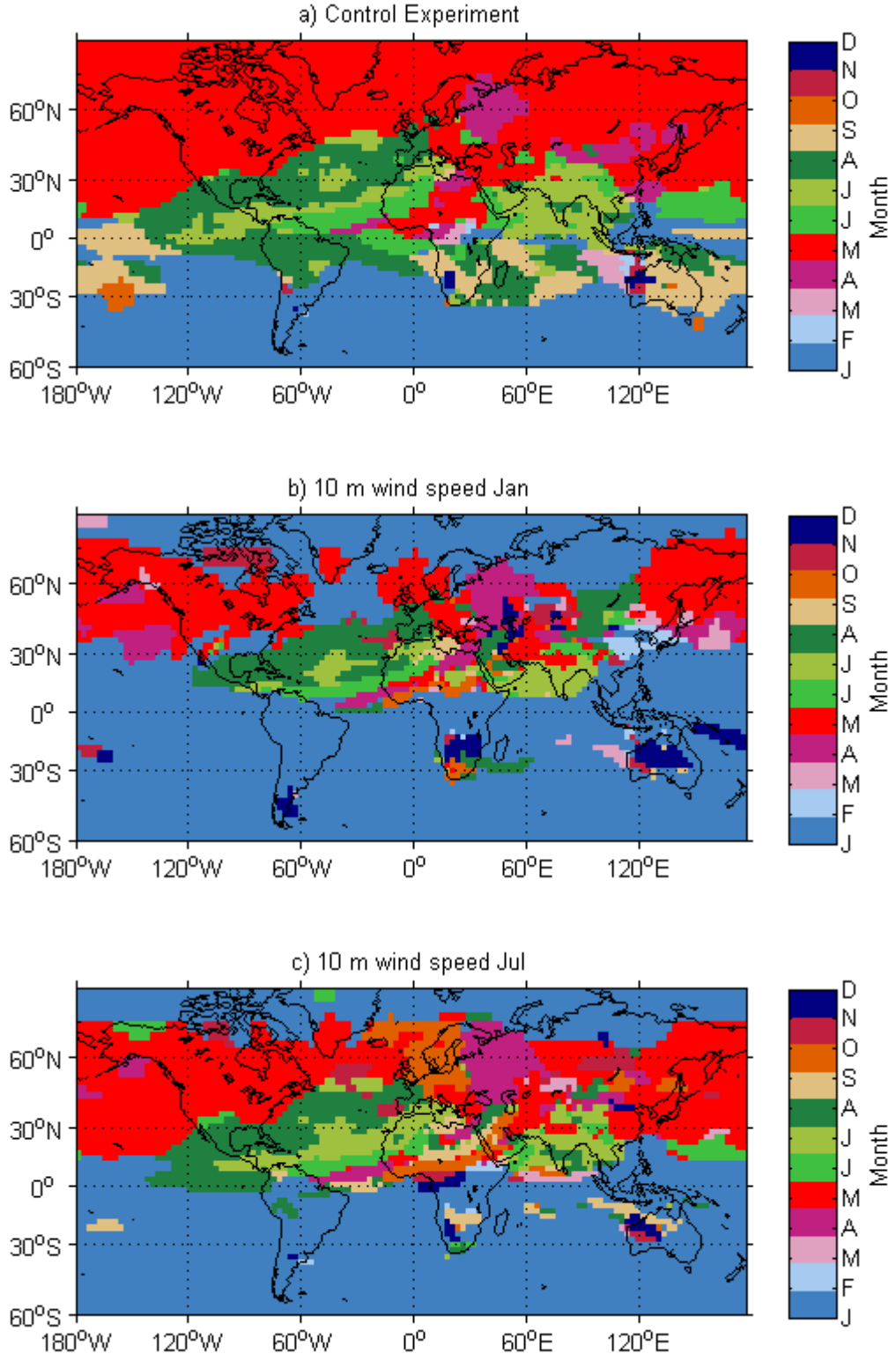

Figure 4-24 The timing of the maximum dust loading for the control experiment and the sensitivity experiments.

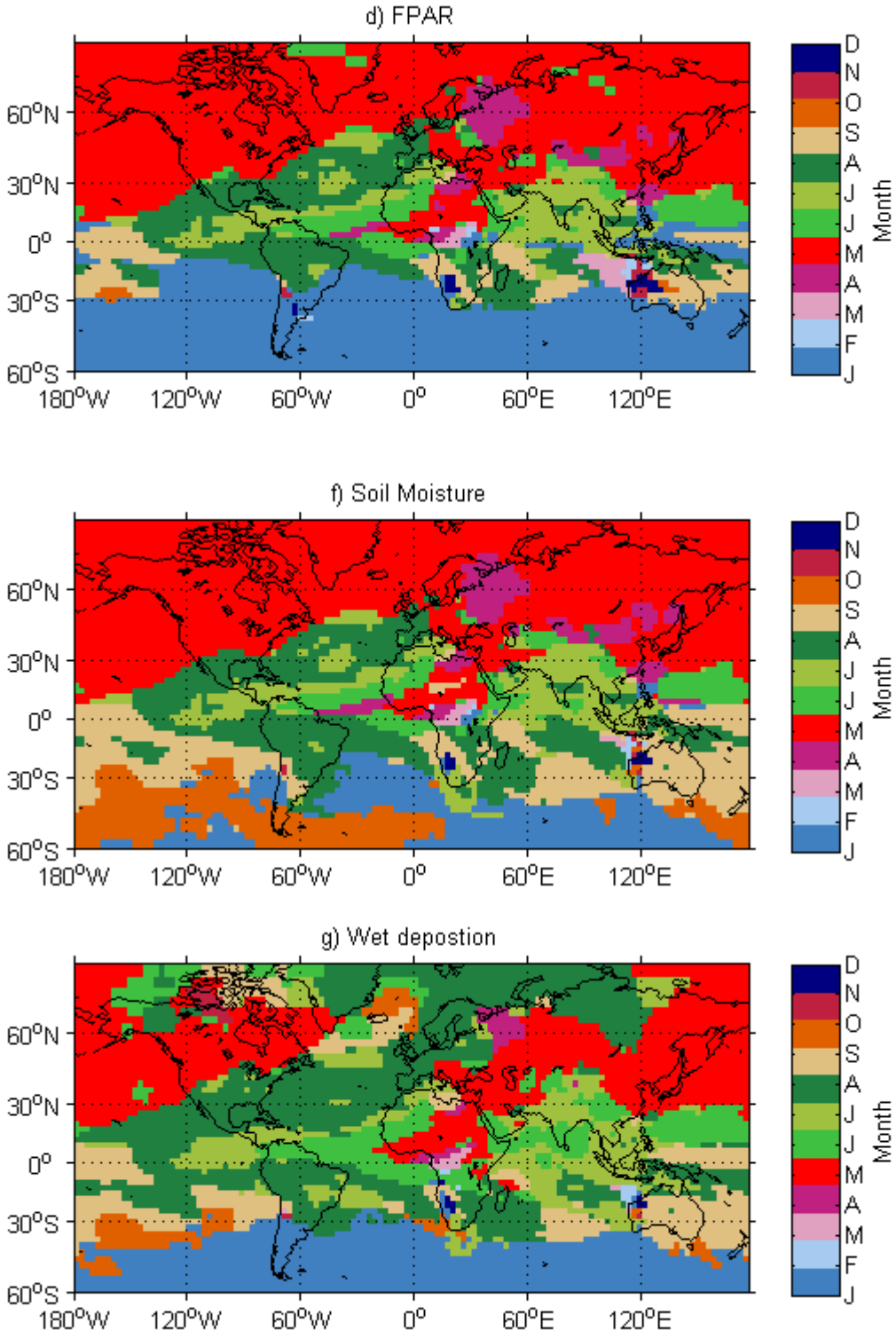

Figure 4-24 (continued)

This is reflected in the fact that there is no difference in the correlation coefficient between the control experiment and the experiment which uses seasonally invariant FPAR. There is also no sensitivity to snow cover which is to be expected as the dust arriving at these sites is influenced by North African dust emissions. The surface concentrations at the North Atlantic sites show a weak sensitivity to surface winds speeds, soil moisture and wet deposition. There is a small improvement in the correlation coefficient when these processes are allowed to vary seasonally.

In contrast to the North Atlantic, sites in the Pacific (Midway Island, Hedo and Enewtak) show a weak sensitivity to FPAR. When the seasonal FPAR is included, the correlation coefficient improves by 8% at Hedo, 11% at Midway Island and 4% at Enewtak. The Pacific sites are also sensitive to the surface wind speeds. This is particularly evident at Hedo, close to the Asian source, where the correlation coefficient improves by 66% when the wind speeds vary seasonally.

At Funafuti there is no sensitivity to vegetation cover or snow cover and a very weak sensitivity to soil moisture, winds speeds and wet deposition. This site is far from the Asian dust source and the seasonality is dominated by transport processes.

The dust concentrations at Mawson in Antarctica are influenced by Patagonian dust. Strong sensitivity to soil moisture is seen at this site. This is confirms the results found in section 4.3.1 which showed that Patagonian dust emissions are controlled by precipitation and its subsequent influence on soil moisture. The correlation coefficient improves from 0.54 to 0.8 when seasonal variability in soil moisture is included in the model.

4.4 Conclusions

This first aim of this chapter has been to assess how well the LPJ-dust model predicts seasonality in the dust cycle. The comparison with TOMS AI shows that the model is successful at predicting the seasonality in total atmospheric dust loading over North Africa, Asia, North America, South America and South Africa. In Australia the model predicts the timing of the maximum surface emissions from August to December instead of DJF. This coincides with when LPJ incorrectly predicts the timing of the minimum vegetation cover.

Site	*Control*	*January winds*	*July winds*	*FPAR*	*Snow cover*	*Soil moisture*	*Wet deposition*
Bermuda	0.90	0.88	0.86	0.90	0.90	0.88	0.88
Barbados	0.84	0.83	0.84	0.84	0.84	0.84	0.87
Miami	0.87	0.81	0.84	0.87	0.87	0.85	0.80
Hedo	0.79	0.18	0.32	0.73	0.82	0.82	0.45
Midway	0.55	0.45	0.61	0.49	0.57	0.61	0.60
Enewtak	0.51	0.62	0.67	0.49	0.52	0.54	0.76
Funafuti	0.90	0.87	0.85	0.90	0.90	0.89	0.87
Mawson	0.80	0.72	0.84	0.82	0.80	0.54	0.48
Cape Point	0.54	0.76	0.74	0.58	0.54	0.66	0.70

Table 4-3 Correlation coefficients between the simulated monthly mean surface concentrations and measurements from the University of Miami aerosol network for the sensitivity experiments and the control experiment.

A comparison of the simulated surface concentrations with measurements shows that the model is able to predict the magnitude of the surface concentrations in the North Atlantic and at sites close to the Asian source region. However, at sites far from the Asian source region, the model overestimates the absolute magnitude of the dust concentrations by a factor of 15-30.

This finding is similar to previous modelling studies in which the surface concentrations were predicted well close to the Asian source region, but overestimated in the central Pacific (Ginoux et al. 2001; Yue et al. 2009). The work of Yue et al., (2009) suggested that the overestimate of dust concentrations in the remote Pacific was caused by inaccuracies in the GCM fields use to drive the model. The GCM fields were taken from the IAP9L-AGCM (Liang 1996).

In the work of Ginoux et al., (2001) surface concentrations were overestimated by a factor of 3-5 in the central Pacific. The discrepancy was attributed to an incorrect parameterisation of the soil size distribution in Asia. The simulated volume size distribution over Asia was compared to retrievals of volume size distribution derived from AERONET data (Dubovik and King 2000) and it was found that the model over estimated small particles with diameter 1.5μm by a factor of 3-5. The soil size distribution was calculated using the Zobler soil texture map (Zobler 1986) which is also used in the LPJ-dust model.

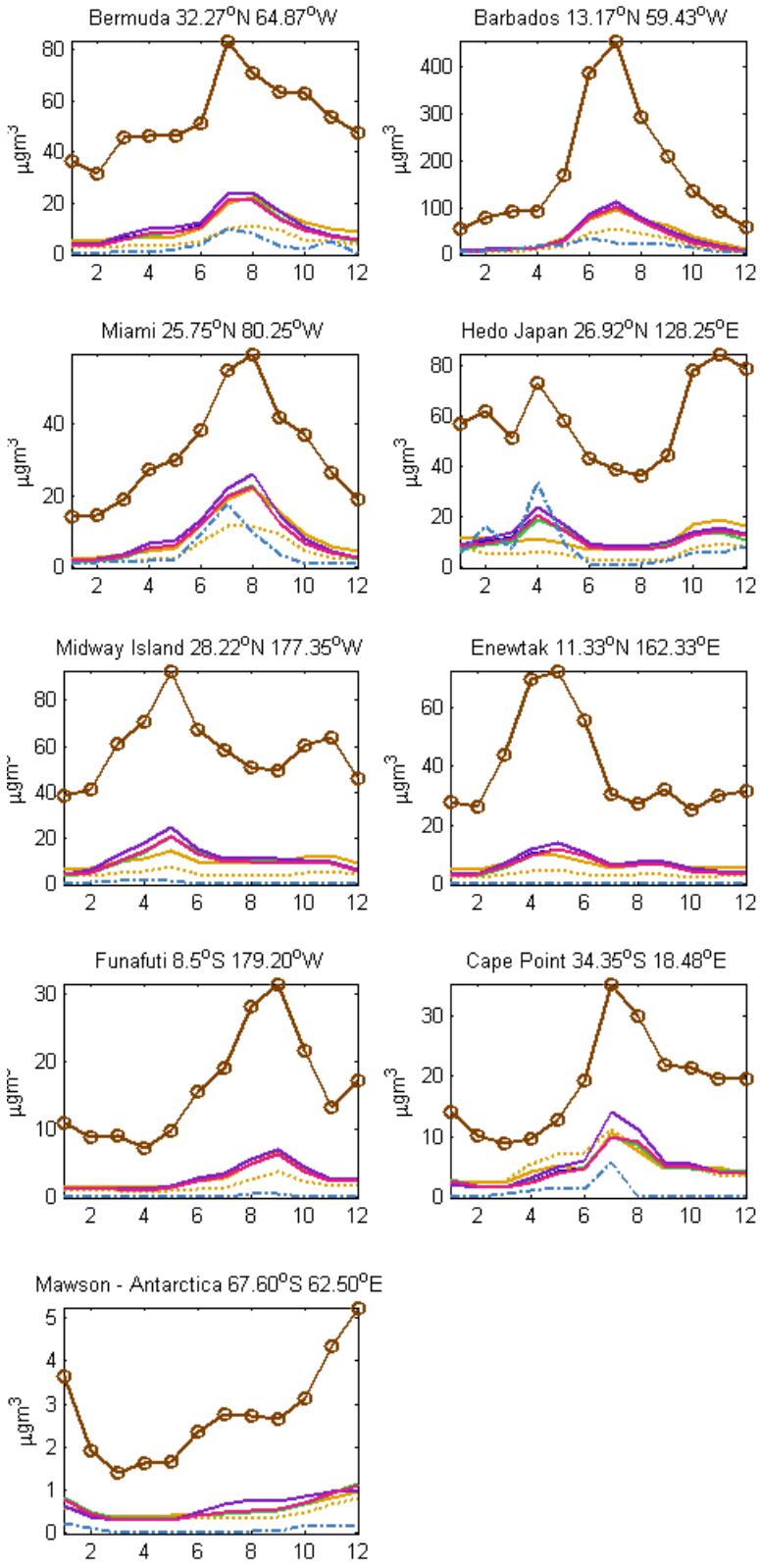

Figure 4-25 Simulated monthly mean surface concentrations for the sensitivity experiments compared to the measurements from the University of Miami aerosol network. The measurements are shown in (blue dashed), control experiment (pink), seasonally invariant FPAR (green), snow cover (blue), soil moisture (violet) and wet deposition (brown circles). Wind speeds fixed to July values every year (orange line) and January (orange dotted line)

Future development work on the LPJ-dust model could compare the soil size distribution to observational data to investigate if the soil size distribution overestimated in Asia.

Tegen et al., (2002) found the opposite result. Surface concentrations were underestimated in the North Atlantic and in the Pacific close to the source by a factor of 2-4 but there was good agreement in the remote Pacific. It was suggested that the underestimate in surface emissions was because anthropogenic disturbances caused by agriculture were not included in the model. Another explanation was that ERA-40 wind speeds were much lower than in reality. The ERA-40 reanalysis data requires data from meteorological stations which are sparsely distributed in remote dust source regions. This means that the reconstructed wind speeds may be less accurate in regions where there are little or no meteorological stations (Trenberth and Olson 1988).

The second aim of this chapter was to investigate which factors are responsible for the seasonality in surface emissions and dust loadings after transport has taken place.

In all regions maximum emissions occured when low precipitation combined with a high frequency of wind speed events greater than $2ms^{-1}$. In Patagonia, surface emissions were strongly anti-correlated with precipitation because wind speeds exceeded $2ms^{-1}$ continuously throughout the year. The seasonality in soil moisture over Patagonia affected the seasonality in the dust loading over the Southern Ocean.

The results of this study showed that maximum emissions occured from the Sahara in summer and from the Sahel in winter. The seasonality in both regions could be understood in terms of seasonal variability in wind speeds and precipitation caused by north-south movement of the ITCZ. In the winter North African dust from the Sahel is transported to the Amazon (Koren et al. 2006). It has been shown that this dust provides nutrients such as phosphates to the Amazon (Swap et al. 1992). This implies that changes in wind speeds or precipitation which control the seasonality in the Sahelian dust emissions may have an impact on the productivity in the Amazon.

5 Inter-annual variability in the global dust cycle

The LPJ-dust model can be used to test whether the contraction and expansion of dust source regions explains observed trends in the atmospheric dust loading on decadal time scales. In this chapter, the model is applied to two regions where vegetation cover is believed exert a control on the size of the source regions. The regions to be studied are North Africa and China.

At Barbados, measurements of dust concentrations have been made since in 1965. The measurements show there has been a four fold increase in dust concentrations during the 1980s relative to the 1960s (Prospero and Nees 1986). Only one modelling study has been reported in the literature which aimed at understanding the reason for this (Mahowald et al. 2002). The model was unable to reproduce the high dust concentrations during 1984-1985 relative to 1966-1967 and they concluded that there must have been a new desert source in North Africa caused by either a natural vegetation shift or desertification from land use.

In Asia, the second region to be studied, observations show that there has been a decreasing trend in dust storms in China from the mid-1950s to the mid-1990s and an increase from 1997-2002 (Lu et al. 2003). There have been conflicting explanations for the decreasing trend. Observational studies have related this variability to changes in local wind speeds (Zhao 2004; Wang et al. 2006).

Modelling studies have been carried out to investigate the cause of the inter-annual variability in Asian dust emissions. Hara et al., (2006) used a regional dust model to investigate the cause of the downward trend in springtime dust storms in China from 1973-2004. It was found that the downward trend from the early 1980s to 1997 was caused by a decrease in the frequency of strong winds. Zhang et al. (2003) modelled Asian dust emissions using the Northern Aerosol Regional Climate Model (NARCM) from 1960 to 2002. Surface wind speeds and precipitation, which controls soil moisture, were found to be the dominant factors that controlled the emissions. It was not possible to test whether changes in vegetation cover contributed to the viability in Asian dust emissions in these two studies because dynamic vegetation was not included in the models.

There is evidence to suggest that changes in vegetation cover contributes to the inter-annual variability in Asian dust emissions (Zou and Zhai 2004). It was shown using NDVI data that springtime dust storm frequencies were anti-correlated with springtime vegetation cover in Northern China and in Central and Eastern Mongolia over the years 1982-2001.

In this chapter the LPJ-dust model is used to test two hypothesises;

1. Changes in vegetation cover at the Sahara-Sahelian boundary are responsible for the increase in dust concentrations observed at Barbados during the 1980s relative to the 1960s (Mahowald et al. 2002).

2. Changes in vegetation cover have contributed to the variability in springtime dust storm frequency in Northern China (Zou and Zhai 2004).

To test the first hypothesis an long LPJ-dust simulation is run and the simulated surface concentrations are compared to the Barbados dust record. To assess how well the LPJ-dust model predicts inter-annual variability in surface concentrations at other locations the simulated surface concentrations at sites in the University of Miami aerosol network are compared to another modelling study (Mahowald et al. 2003).

To test the second hypothesis a comparison is made between simulated visibility and visibility measurements from meteorological stations in Northern China compiled by (Mahowald et al. 2007). Sensitivity studies are carried out to test if vegetation cover has contributed to the variability in springtime visibility in Asia. The sensitivity studies also investigate the impact of soil moisture, surface wind speeds, snow cover, surface emissions and wet deposition on the springtime visibility.

5.1 Experimental setup

The LPJ-dust model is run for the period 1958-2000 using threshold parameters and the size-dependent removal scheme determined from the model tuning carried out in chapter 3. This simulation period is chosen as it coincides with the availability of ERA-40 reanalysis data and dust concentration measurements from the University of Miami aerosol network.

The total column dust loading and surface concentrations are output on a daily basis for the years 1958-2000.

5.2 Vegetation constraints on North African dust emissions

Figure 5-1 shows the annual mean simulated and measured surface concentrations at Barbados. The correlation coefficient over the complete period 1965-2000 is very poor (r=0.34). However, between 1965 and 1978 the model does a very good job at predicting the annual mean surface concentrations. The correlation coefficient over this period is 0.82 which is statistically significant to the 95% confidence level (p=0.04).

The model is predicts high dust concentrations at Barbados from 1993 to 2000. A preliminary analysis shows that this is not caused by a sharp increase in North African dust emissions but rather from a reduction in the amount of dust removed by wet deposition over the North Atlantic. This is an interesting result because it was shown in Chapter 4 that the model was successful at predicting the seasonality in surface concentrations at sites in the North Atlantic (Barbados, Miami and Bermuda) when simulations are run for the years 1990-2000.

The measurements show a period of years (1983, 1984, 1985 and 1987) where dust concentrations are persistently high. These high dust concentrations are underestimated by the model. The measurements show maximum concentrations during 1983 when the annual mean concentrations are $30\mu gm^{-3}$. In contrast to this, the model predicts concentrations of $19.9\mu gm^{-3}$ for the same year. The underestimate by the model suggests that the LPJ-dust model has missing processes. These missing processes have caused emissions from North Africa to increase up to 60% during the 1980s.

Figure 5-2 (a) shows the annual mean FPAR over the Sahel and Sahara for the year 1966 when the measurements of dust concentrations at Barbados are low. Figure 5-2 (b) shows the annual mean FPAR over the Sahel and Sahara for the year 1984 when measurements of dust concentrations at Barbados are high. The position of the Sahara-Sahelian boundary line was further south in 1984 than in 1966.

The southward movement of the Sahara-Sahelian boundary line has been observed from NDVI data from the AVHRR (Tucker and Nicholson 1999). An analysis for NDVI data

from 1980-1990 showed that the Sahara-Sahelian boundary was at its most southerly position in 1984. This can be explained by the fact there was a prolonged period of drought in the North Africa during the 1980s. Rainfall measurements from the Sahel show that this was the driest decade of the century (Nicholson 1993).

Figure 5-2 (c) and (d) shows the annual mean surface emissions for the same years. It can be seen that the southward movement of the Sahara-Sahelian boundary line in 1984 compared to 1966 resulted in an expansion of the Sahara. Increased emissions are seen south of 18^{o}N in 1984. Over the Sahel at latitudes 10-20^{o}N and longitudes 17 ^{o}W to 40^{o}E, there was a doubling of emissions between 1966 and 1984. The total emissions of particles with diameter less than 220μm is 1.1Mtyr^{-1} in 1966. This increased to 2.2Mtyr^{-1} in 1984.

These results indicate that even though there was an expansion of the Sahara caused by vegetation changes in the Sahel during the 1980s, this is not enough to account for the high dust concentrations at Barbados.

Another possible reason why the model underestimates dust concentrations during the 1980s is because preferential dust source regions are not accounted for in the LPJ-dust model. It is possible that during the 1980s there was a climatic change that increased emissions from preferential sources. An experiment which includes preferential sources is carried out to test whether their inclusion improves the ability of the LPJ-dust model to predict the high dust concentrations observed at Barbados during the 1980s.

Preferential source are assumed to be present in regions where lakes existed in the past in which highly erodible alluvium sediment has accumulated. The same approach was taken by Tegen et al., (2002). A static map of preferential source data was provided by Ina Tegen and is shown in Figure 5-3.

The location of dried out lake beds are identified using the HYDrological Routing Algorithm (Coe 1998). HYDRA uses a land surface topography map to calculate the extent of lakes as a function of precipitation, run off and surface evaporation. The HYDRA model was run using unlimited precipitation and the difference between simulated lakes and lakes present today indicates places where lakes would have existed in the past under a wetter climate. If a preferential dust source is present then the particle size distribution is modified to reflect the fact there is more fine grain sediment on the surface. The mean

particle radius for preferential source in the northern hemisphere is 15μm and in the southern hemisphere is 27μm.

Figure 5-4 shows the simulated annual mean surface concentrations at Barbados when the preferential dust source regions are included and the measurement data. Including the preferential dust source regions increases the amount of dust transported to Barbados. However, the model is still unable to reproduce the high concentrations during the 1980s relative to the low concentrations during the 1960s. The correlation coefficient between the simulated dust concentrations and the observations only increases from 0.34 to 0.37 when preferential dust source regions are included.

Another possible explanation for why the LPJ-dust model under predicts the dust concentrations during the 1980s is because new preferential sources have been created. A possible example for this is Lake Chad. Lake Chad has reduced in size from an area covering approximately 25,000km^2 in 1963 to 1350km^2 in 1996 (Grove 1996). It has been shown that the fastest decline occurred between 1983-1994 when water use for irrigation increased four fold (Coe and Foley 2001). That study concluded that 50% of the variability was caused by the climate and 50% was caused by human water use.

Mahowald et al., (2002) investigated whether the reduction in the size of Lake Chad has increased dust concentrations at Barbados using a dust cycle model. It was found that the additional dust emissions arising from a reduction in Lake Chad was not sufficient to cause the increase observed at Barbados during the 1980s. Furthermore, satellite observations using TOMS aerosol index indicate that Lake Chad is not a strong emitter of dust and that most dust in this region comes not from Lake Chad but from the Bodele depression (Prospero et al. 2002).

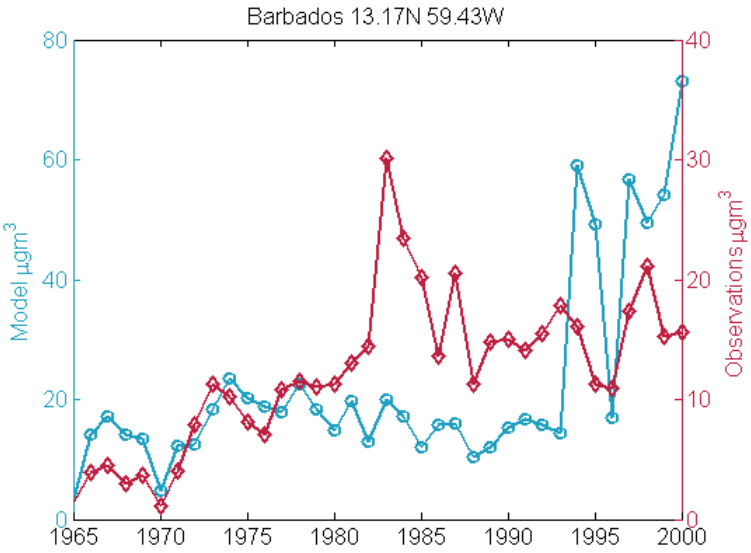

Figure 5-1 Simulated and measured annual mean surface concentrations at Barbados. The correlation coefficient between 1965 and 1978 is 0.82. Thereafter, the model is unable to predict the inter-annual variability.

5.3 Comparison between simulated surface concentrations and observations

Figure 5-5 shows the simulated annual mean dust concentrations and measurements from the University of Miami aerosol network. There are 12 sites in the network that contain more than 12 months of measurements. The correlation coefficients between the simulated annual mean surface concentrations and the observations are listed in Table 5-1. The correlation coefficients are calculated over the period 1979-2000 so a comparison can be made with the modelling study of Mahowald et al., (2003). The correlation coefficients from the modelling study of Mahowald et al., (2003) are also included in Table 5-1.

The comparison with the measurement data shows that the model over predicts the magnitude of the surface concentrations at sites in the Pacific at Enewtak, Funafuti, Midway Island and Hawaii (note the different scale on the y axis) but is successful at predicting the relative year to year variability. The overestimate in surface concentrations at sites in the remote Pacific were also evident in the monthly mean surface concentrations in Chapter 4 (see section 4.2.2).

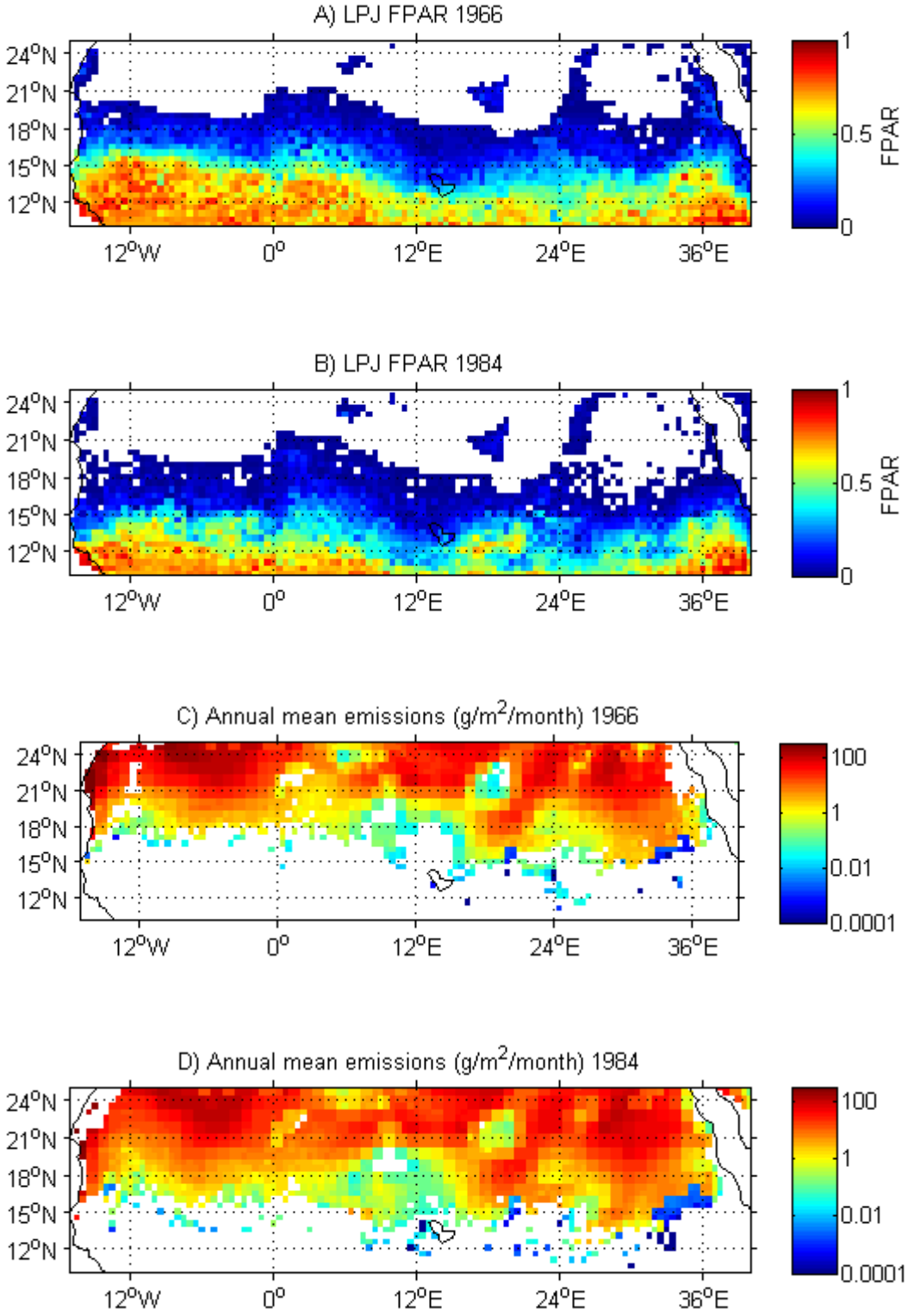

Figure 5-2 Annual mean FPAR and emissions predicted by LPJ Sahara-Sahelian boundary for the years 1984 and 1966.

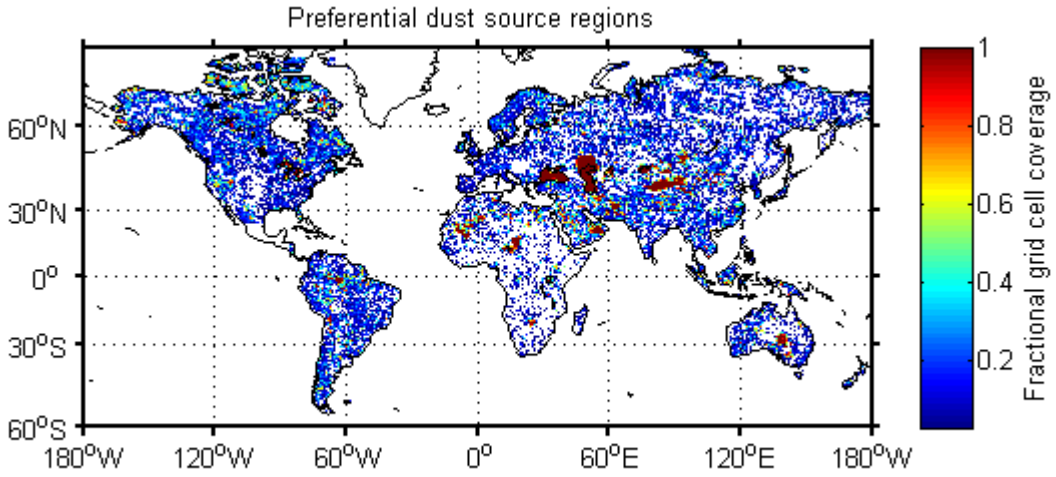

Figure 5-3 Areal coverage of preferential dust sources regions calculated from the extent of potential lake areas using HYDrological Routing Algorithm (Coe 1998).

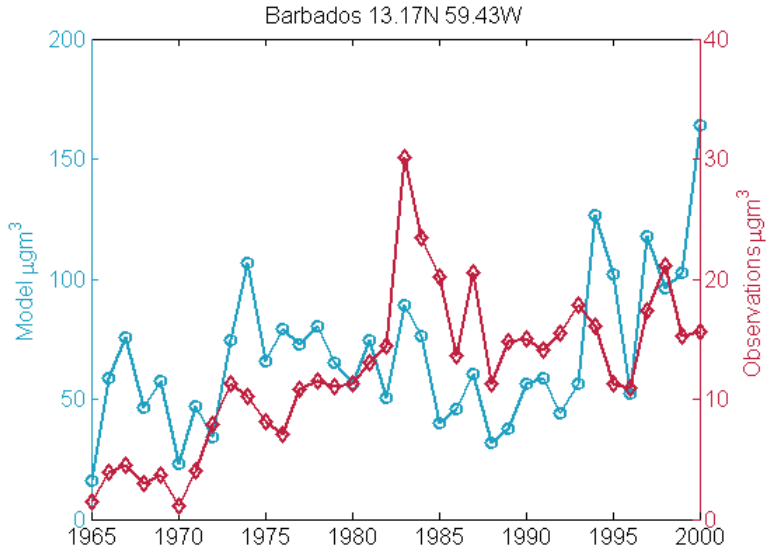

Figure 5-4 Simulated annual mean surfaces concentrations at Barbados when preferential dust source regions are included.

The inter-annual variability is predicted well at Cape Grim (r=0.7) and Norfolk Island (0.77) which are influenced by Australian dust emissions. The correlation coefficients are high at these sites but the number of months of measurement data is low.

The model does a poor job at predicting the inter-annual variability at sites in the North Atlantic (Barbados, Bermuda and Miami) even though these sites have the greatest amount of measurement data. The correlation coefficients for Izaña and Mace Head are better than other sites in the North Atlantic but are still lower than those in the Pacific.

It can be seen from Table 5-1 that the LPJ-dust model performs better than the model used by Mahowald et al., (2003) at the sites affected by Asian dust but worse at sites affected by North African dust. This suggests that some processes that control the inter-annual variability in North African dust emissions are missing in the LPJ-dust model but present in the Mahowald et al., (2003) model.

The model used by Mahowald et al., (2003) is different in many ways to the LPJ-dust and it is unsurprising that there are differences. Their model uses the Desert Entrainment and Deposition model (DEAD) (Zender et al. 2003a). This scheme identifies source regions as topographic lows using a surface elevation map. The bare ground fraction is related to the leaf area index using a vegetation dataset derived from the advanced very high resolution radiometer data (AVHRR). Changes in the vegetation cover caused by fire or land use will be picked up by the AVHRR data but will not be present in the LPJ vegetation. Fire and land use are not included in the LPJ-dust model and this may one reason why the LPJ-dust model does not perform as well over North Africa as the Mahowald et al., (2003) model.

There are several possible reasons why the LPJ-dust model performs better in Asia than the Mahowald et al., (2003) model. One explanation is that estimates of the Asian emissions are improved when the soil moisture is consistent with the vegetation cover as in the case of the LPJ-dust model. Another possible reason is that forcing the model with ERA-40 reanalysis data using TOMCAT gives better results than using NCEP reanalysis data with the MATCH chemical transport model. The wet deposition scheme used by the LPJ-dust model is simpler than that use by the Mahowald et al., (2003) model which includes in-cloud scavenging as well as sub cloud scavenging. It is possible that the more simplified removal scheme gives better estimates of dust concentrations.

5.4 Vegetation constraints on Asian dust emissions

This section tests whether changes in vegetation cover have contributed to the variability in springtime dust storm frequency in Northern China. Observations of visibility have been obtained from Natalie Mahowald by personal communication. The global dataset has been compiled from meteorological stations located in dusty regions (Mahowald et al. 2007).

Visibility is defined as the distance in meters from which a large black object can be seen against the sky at the horizon (Seinfeld 1998). The visibility data contains the fraction of the month when the visibility is less than 5km. The data is available on a monthly time step and extends from 1900 to 2004. Most of the reliable data is available from 1974 to 2003 (Mahowald et al. 2007). Visibility measurements for March and April over Northern China (30 ^{o}N to 50^{o}N and longitudes 90 ^{o}E to 130^{o}E) are extracted from the dataset.

In order to compare to the modelled data with the visibility observations, the daily surface concentrations are converted into visibility. There are many ways to convert dust concentrations to visibility which are based on empirical relationships between measurements of dust concentrations and visibility (Woodruff 1957; Patterson and Gillette 1977; Dayan et al. 2008). The relationship between the visibility and dust concentrations depends on the size of the dust particles and the degree to which the dust attenuates light by scattering and absorption.

The relationship used to convert dust concentrations to visibility is taken from Ette and Olorode (1988). Several other relationships were tested but this one gave the best correlation coefficients with the measured visibility data.

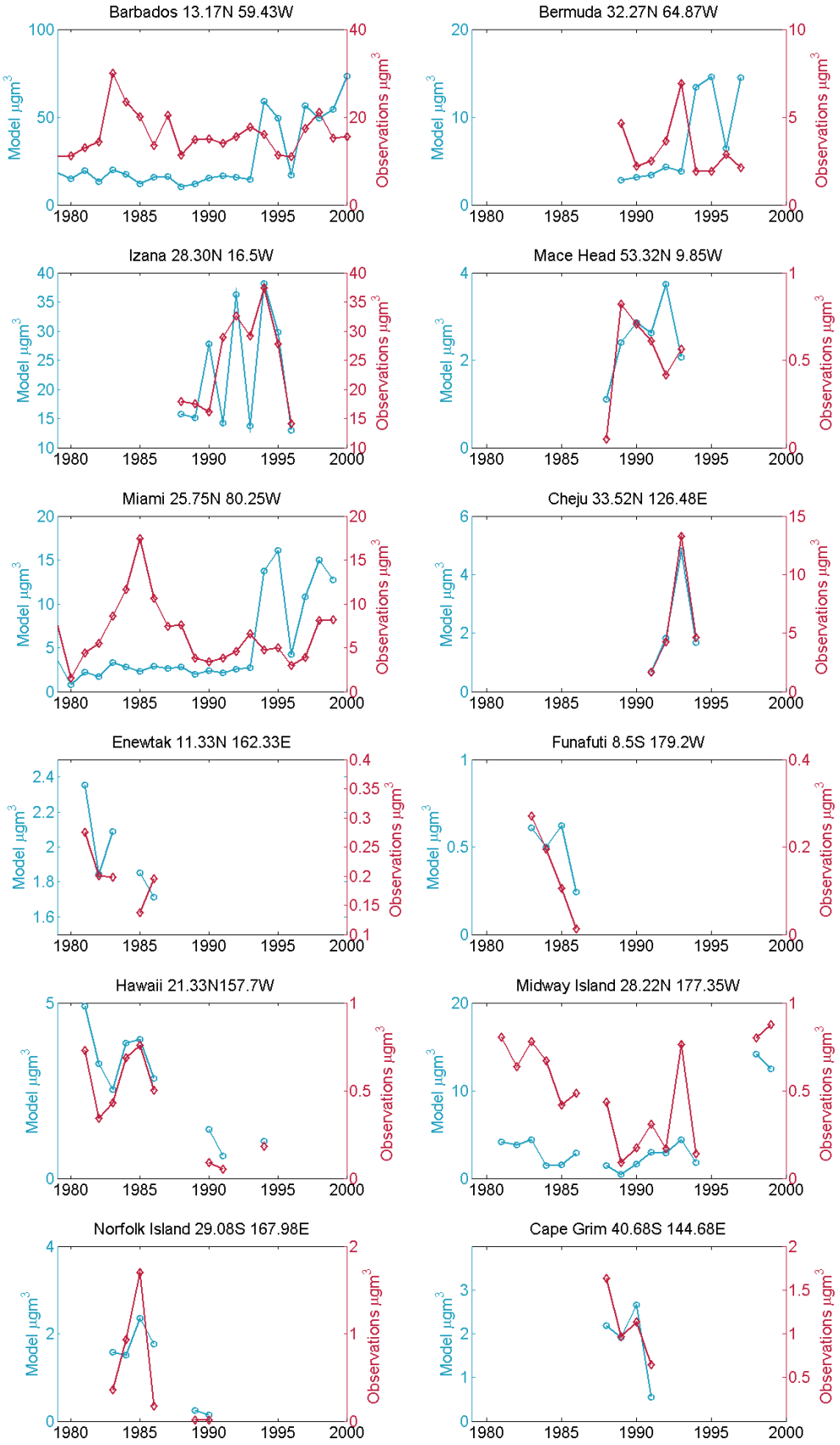

Figure 5-5 Comparison of simulated annual mean surface concentrations and measurements from the University of Miami aerosol network.

Years	*LPJ-dust*	*Mahowald et al., 2003*	*Number of months of*
1979-2000	*Annual correlation*	*Annual correlation*	*data*
Barbados	0.03	0.38	390
Bermuda	-0.56	0.84	108
Cape Grim	0.70	-	40
Cheju	1.0	-	18
Enewtak	**0.75**	**0.71**	**43**
Funafuti	0.73	-	39
Hawaii	**0.94**	**0.48**	**62**
Izaña	0.60	0.64	104
Mace Head	**0.48**	**-0.53**	**59**
Miami	0.06	0.03	260
Midway Island	**0.65**	**-0.41**	**109**
Norfolk Island	**0.77**	**0.39**	**44**

Table 5-1 Correlation coefficients between the simulated annual mean surface concentrations and measurements from the University of Miami aerosol network. The correlation coefficients from the modelling study by Mahowald et al., (2003) are also listed. Sites where the LPJ-dust model performs better than the Mahowald et al., (2003) model are highlighted in bold.

The visibility is calculated using the following relationship

$$Vis(km) = \left[\frac{M(\mu gm^3)}{a} \right]^{-\frac{1}{b}}$$

where M is the monthly simulated surface concentrations, a=1600 ($\mu gm^{-3}km$) and b=0.62 (dimensionless).

Figure 5-6 shows the fraction of the month when the visibility is less than 5km averaged for March and April over Northern China. Data is shown for observations and the model. March and April are selected for study as this is time of year when the majority of dust storms occur in Asia. This was shown in Chapter 4. The measurement data are averaged for sites in Northern China with latitudes 30-50^{o}N and longitudes 90-130^{o}E. Similarly, the modelled visibility is taken for model grid points where the measurements data is available.

It can be seen from Figure 5-6 that the model overestimates the fraction of the month when the visibility is less than 5km by a factor of 10. There are three possible reasons for this overestimation.

The first is that the model overestimates dust emissions from Northern China. In section 0 a comparison was made between simulated and measured surface concentrations. It was seen that the model over estimates surface concentrations at sites at Enewtak by a factor of 6.2, Hawaii by a factor of 5 Midway Island by a factor of 20. The overestimate of Asian dust emission was also highlighted in section 4.2.2.

The second reason why the model overestimates the fraction of the month when the visibility is less than 5km may be because of an uncertainty in the relationship used to convert the surface concentrations data to visibility. The visibility is dependent on the dust particle size. The relationship used to convert the surface concentrations to visibility is valid for dust with diameter less than 3.2μm, while the simulated surface concentrations consists of dust with diameter ranging from 0.1-220μm. Furthermore, the visibility is dependent on the optical properties of the dust which varies from region to region. The third reason is that the visibility measurements may not be reliable. The visibility observations are made by eye which makes the data rather subjective.

Figure 5-6 shows that the model under predicts the visibility from 1975-1981 but agrees well with the observational data after that. A similar finding was reported by O Hara et al., (2006) who used a regional dust model to predict visibility in the Gobi. Their model under predicted springtime visibility from 1972-1981 but agreed well from 1981 to 2003.

The LPJ-dust model is able to predict the overall downward trend between 1983 and 2000 which consists of a downward trend between 1983 and 1992, a subsequent increase from 1992-1994, a decrease from 1994-1997 and an increase from 1997-1998. The correlation coefficient between 1983 and 2000 is 0.53 which is significant to the 95% confidence level ($p=0.02$).

Figure 5-7 (a) and (b) shows the monthly FPAR averaged from March to April from LPJ over Northern China for a year with high springtime visibility (1984) and a year with low springtime visibility (1997). There is no well defined vegetation shift in this region, unlike in the Sahara-Sahel. Figure 5-7 (c) and (d) shows that there are more emissions in 1984 when springtime visibility is high compared to 1997 when springtime visibility is lower. In spring 1984 the total emissions of particles with diameter less than 220μm is 16,265gm^{-2}. This is reduced to 7650 gm^{-2} in spring 1997 when visibility is lower. There is no obvious change in vegetation cover between these years which suggests that another processes is

responsible for the decrease in emissions. Sensitivity studies are carried out in the next section to test which processes are responsible for the change.

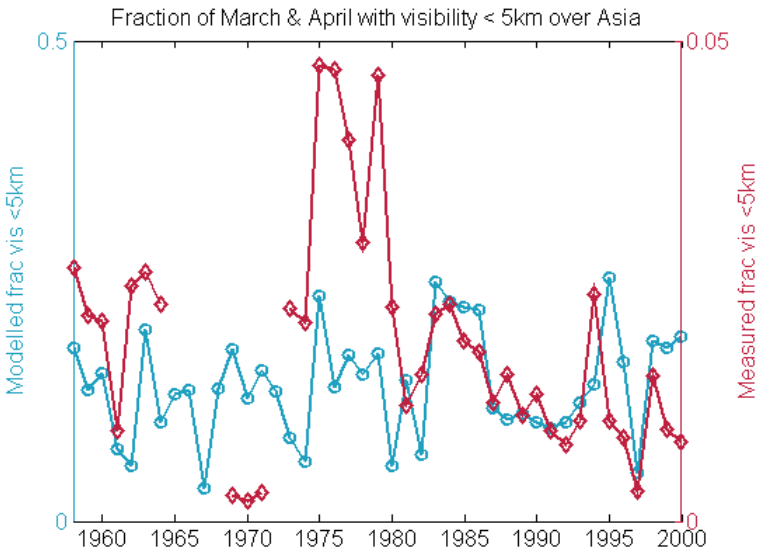

Figure 5-6 The fraction the month when the visibility is less than 5km, averaged for March and April. The measurement data is averaged for all sites in Northern China (30-50^{o}N and 90-130^{o}E). The simulated data is averaged for corresponding model grid points where the measurement data exists. Data from 17 measurement sites are used.

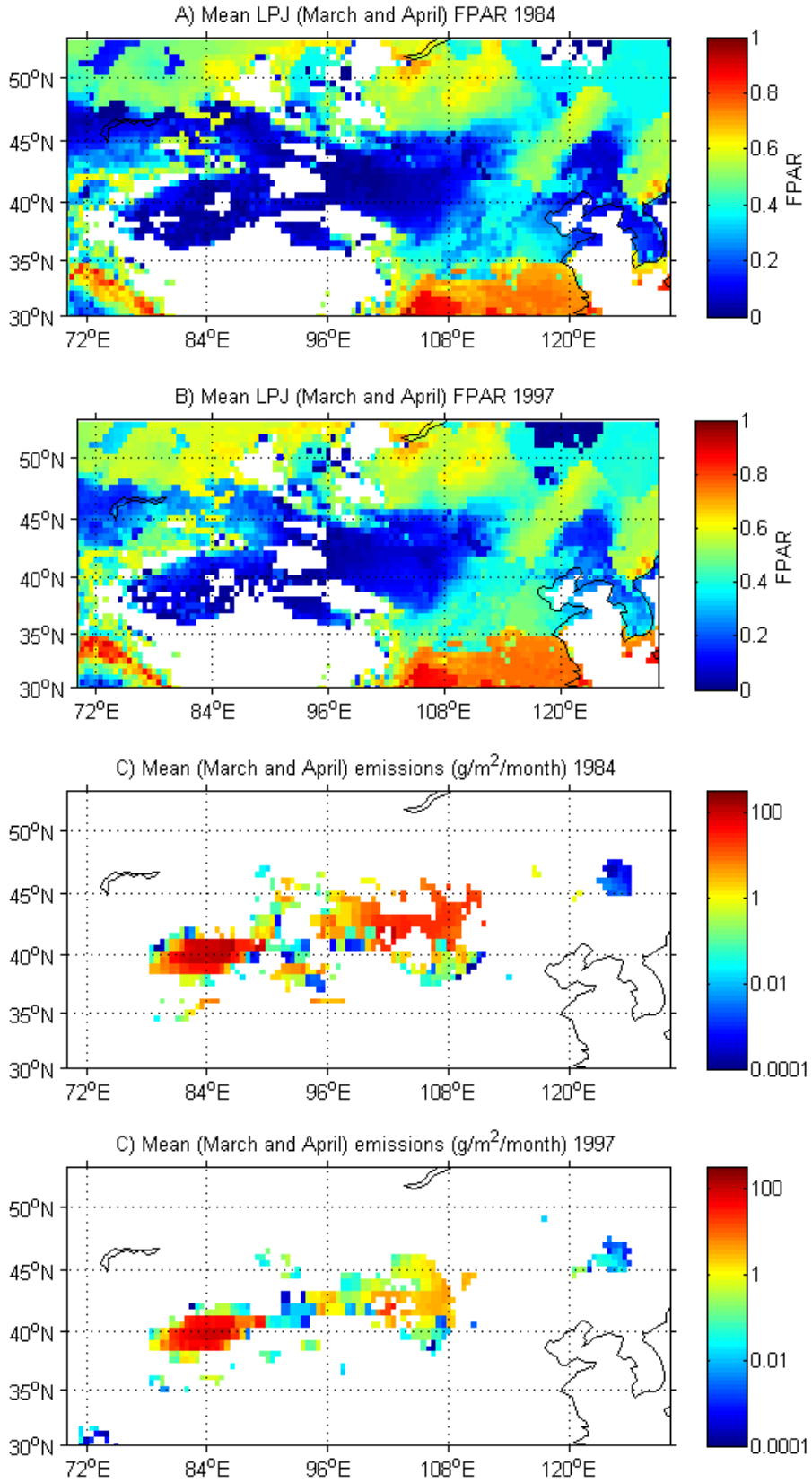

Figure 5-7 Monthly surface emissions and monthly FPAR averaged for March and April simulated by LPJ over North China.

5.4.1 Sensitivity studies

Six sets of sensitivity experiments are carried out to test whether the decline in springtime visibility in Asia is caused by changes in snow cover, soil moisture, surface wind speeds, vegetation cover, emissions or wet deposition. The sensitivity experiments are described in further detail below. The experiment described in 5.1 is used as the control experiment.

Vegetation cover

The surface emissions are calculated using the mean vegetation and mean FPAR over the period 1958-2000. The mean FPAR refers the mean climatology calculated from the mean of all the Januarys, Februarys etc. for each year. The mean vegetation cover is calculated by taking the mean of the annual growing degree days, tree height and foliage projective cover from 1958-2000. A biome map is produced using the mean annual growing degree days, tree height and foliage projective cover using the scheme developed Joos et al., (2004). By taking this approach, the vegetation cover does not vary from year to year but it does vary seasonally with the seasonal FPAR. All the other parameters in the model are allowed to vary from year to year.

Snow cover

It was seen in Chapter 4 that snow cover affected the seasonality in surface concentrations at sites down wind of the Asian source. Thus, snow cover may play a role in determining the inter-annual variability in Asia. The surface emissions are calculated using the monthly mean climatological values for snow cover over the period 1958-2000.

Soil moisture

In this experiment, the surface emissions are calculated using the monthly mean climatological values for soil moisture over the period 1958-2000.

Surface emissions

This experiment takes into account the combined effects of changes in vegetation cover, soil moisture, snow cover and wind speeds. The model is run using mean surface emissions calculated over the period 1958 to 2000. The mean surface emissions do not have any inter-annual variability but they do vary seasonally.

Wet deposition

Wet deposition in the model is represented by the process of sub cloud scavenging. The scheme uses ERA-40 6 hourly convective precipitation, large scale precipitation, low cloud and medium cloud amount to calculate the amount of dust removed by wet deposition. To test if the inter-annual variability is caused by changes in the wet deposition the model is run using the monthly mean climatological values for the large scale precipitation and convective precipitation, low cloud amount and medium cloud amounts. All the other parameters in the model are allowed to vary from year-to-year.

Surface wind speeds

The surface emissions are calculated by fixing the 10m ERA-40 6 hourly surface wind speeds to the year 1958. This experiment is different from the previous experiments because the wind speeds are fixed to one year rather than calculating a long term mean over the simulation period. Taking the long term mean would average out periods of high wind speeds. Because there is a cubic dependency between the wind speeds and the dust flux, periods of high wind speeds will have a large impact on dust emissions.

Figure 5-8 shows the measured and modelled fraction of the month when the visibility is below 5km, averaged for March-April, for each sensitivity experiment. The correlation coefficients between the simulated visibility and measurements are listed in
Table 5-2 for each sensitivity experiment. The sensitivity studies show that the inter-annual variability in visibility is controlled by surface winds speeds. This is reflected in the reduction in the correlation coefficient from 0.53 to -0.15 when the winds speeds are fixed to the year 1958. This result is consistent with the work of Wang et al., (2006) who found, on the basis of field measurements conducted between 1960 and 2003, that the inter-annual variability in dust storm frequency in northern China was related to local wind speed activity. The results contradict the hypothesis that changes in springtime vegetation cover has contributed to the variability in dust storms in Northern China.

Time period	*Control*	*Snow cover*	*Vegetation cover*	*Soil moisture*	*10m wind 1958*	*Emissions*	*Wet deposition*
1983-2000	0.53	-0.05	0.60	0.53	-0.15	-0.13	0.53

Table 5-2 The correlation coefficient between the measured and modelled fraction of the month (March and April averaged) when the visibility is less than 5km.

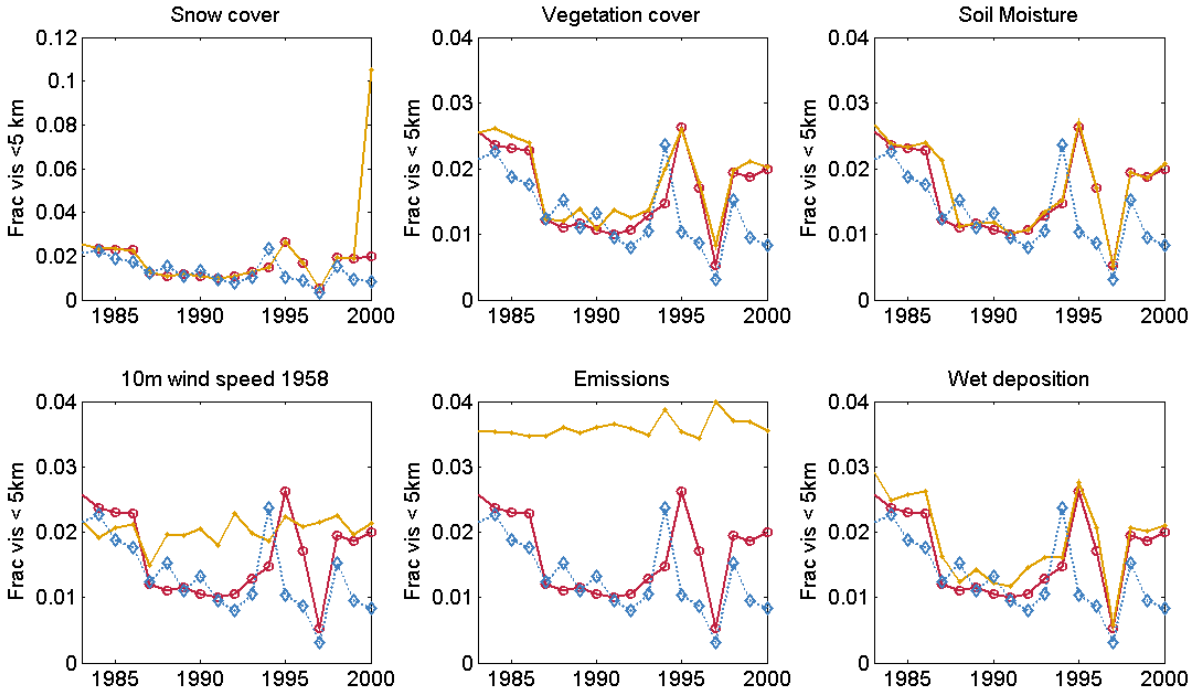

Figure 5-8 The fraction of the March and April averaged when the visibility is less than 5km. The control experiment is shown in red, the measurements in blue and the sensitivity experiment in orange. The modelled data over predicts the visibility by a factor of 10. Possible explanations for this are in discussed in section 5.4. The simulated data has been scaled by dividing by 10 for the purpose of presenting the data.

5.5 Discussion

In this chapter the LPJ-dust model was used to study two regions where vegetation cover is believed to control the extent of the source regions on decadal time scales. The regions studied were North Africa and northern China. Two hypotheses were tested.

The first hypothesis tested if the four fold increase in dust concentrations measured at Barbados during the 1980s relative to the 1960s may have been caused by an expansion of the Sahara by changes in vegetation cover or land use (Mahowald et al. 2002). The model was successful at predicting the annual mean surface concentrations at Barbados between 1965 and 1978 but underestimated the high dust concentrations during the 1980s relative to the 1960s. The simulated dust concentrations were 60% lower than the measurements in 1983.

The results showed that there was an expansion of the Sahara in 1984 relative to 1966 which resulted in a doubling of emissions from the Sahel, but that this was not enough to account for the high dust concentrations at measured at Barbados during the 1980s relative to the 1960s. There was no substantial improvement in the model's ability to capture the high dust concentrations at Barbados during the 1980s when preferential dust sources, in the form of dried out lake beds, are included in the model.

Increased desertification from land use may have commenced after 1978 which has lead to a degradation of the soil and an increase in emissions. Mineral dust from anthropgenic sources comes from agricultural practices such as harvesting, grazing or ploughing or from changes in water levels as occurred in the Caspian and Aral sea region (Prospero et al. 2002). It is difficult to assess the impact of land use changes on dust emissions. If the land is cultivated intensively and uses irrigation then there will be a reduction in the erodibility of the soil. In contrast, if land use practices degrade the vegetation then there will be an increase in soil erodibility. This is further complicated by the fact that natural and anthropogenic dust mixes, making it difficult to detect the relative abundance of each downwind of the source regions.

A study by Moulin and Chiapello (2006) showed by analysing TOMS AI data that the high concentrations at Barbados during the years 1983, 1987 and 1988 were caused by a 30-50% increase in dust emissions in the Sahel region centred on southern Mali caused by human induced desertification. They suggested that the desertification was caused by the doubling of the population in the Sahel over the last 40 years.

Indeed there are conflicting opinions over how much land use contributes to the total global dust loading. A study by Tegen and Fung (1995) incorporated disturbed sources caused by cultivation into a dust model. It was estimated that land use may contribute to 30-50% of the global dust loading. A subsequent modelling study by Tegen et al., (2004) estimated that the contribution from land use was less than 10%. This estimate was derived by calibrating a dust model to dust storm frequency observations in agricultural regions.

An analysis of remote sensing data over North Africa has suggested that the contribution from land use is not very large (Prospero et al., (2002). It was shown using TOMS AI that the major dust sources in North Africa are located in regions where with rainfall is less than 200-250mm per year. Agriculture and grazing takes place in these regions but is

localised and clustered around water sources. The majority of agriculture and grazing takes place south of the 200-250mm isohyets, which according to the TOMS data is actually a weak dust source.

The second hypothesis tested whether changes in vegetation cover have contributed to the variability in springtime visibility in Northern China. Very little change in vegetation cover was predicted by the model for the years 1984 when visibility measurements where high and 1997 when visibility measurements were low. The sensitivity studies carried out show that vegetation cover did not contribute to the inter-annual variability in the springtime visibility. This contradicts the study of Zou and Zhai (2004). The springtime visibility between 1983 and 2000 was found to be controlled by wind speeds. This is in agreement with Wang et al., (2006) who deduced from field measurements that the inter-annual variability in dust storm frequency in Northern China was related to local wind speeds.

The result is also agrees with studies that have related the inter-annual variability in dust storm activity in Asia to climatic indices that control the wind speeds. Zhao et al., (2004) showed that the decline in the dust storm frequency in the Midwest Inner Mongolia of China was related to the number of days with wind speeds > $17ms^{-1.}$ They related the inter-annual variability in dust storms to climatic indices which were representative of the large scale cold air activities.

A large amount of data has been generated by the sensitivity studies. Time has not permitted an extensive analysis of this data. Analysing this data in more detail would make it possible to understand the processes responsible for the inter-annual variability in the dust cycle. Although not presented here, a statistically significant correlation coefficient of 0.82 was found between the total column dust loading over North Africa and the North Atlantic in winter and the winter NAO index between 1957 and 1971. Remote sensing studies have found a correlation over North Africa and the North Atlantic and the NAO index (Moulin et al. 1997; Chiapello and Moulin 2002; Chiapello et al. 2005; Evan et al. 2006). The sensitivity studies could be used to investigate which meteorological conditions associated with the NAO control the total column dust loading. This would further our understanding of the processes which cause natural variability in the dust loading as opposed to the effects of human activity. It is important to understand the relative contribution of both of these factors in order to predict how the dust loading will change in the future.

6 Conclusions

6.1 Summary of findings

This section revisits the aims of the thesis set out in chapter 1 and discusses the extent to which the aims have been met.

The primary aim of this work has been to develop a dust cycle model that uses the LPJ dynamic global vegetation model to calculate dust source areas. This work was motivated by the fact that existing dust cycle models did not include dynamic vegetation. This limitation meant that it was not possible to study the natural variability in the extent of desert regions caused by the transient response of vegetation cover to the climate. The development of the LPJ-dust model has now made this possible.

In Chapter 2 the new dust model was described. Dust source areas were identified as sparsely vegetated, dry regions and were calculated using LPJ simulated vegetation cover, soil moisture and snow cover. A preliminary study was carried out to test if LPJ could accurately predict the seasonal variability in vegetation cover. The timing of the minimum FPAR predicted by LPJ was compared to FPAR derived from the SeaWiFS sensor. LPJ predicted the timing of the minimum vegetation cover reasonably well in the Sahel, Asia, South America, and in the interior of South Africa. In Australia LPJ predicted the timing of the minimum vegetation four months too early. This limited the ability of the model to predict the seasonality in surface emissions from Australia correctly.

A base line LPJ-dust simulation was carried out and the annual mean surface emissions were compared to other modelling studies (Werner et al. 2002; Luo et al. 2003; Zender et al. 2003a; Ginoux et al. 2004; Miller et al. 2004; Tanaka and Chiba 2006). The surface emissions predicted by the baseline simulation were found to lie within the range of estimates predicted by other models. However, estimates of the surface emissions from the other modelling studies varied by a factor of 2. The comparison also showed regional differences in the surface emissions predicted by the models.

The second aim of this thesis was to improve the performance of the LPJ-dust model by tuning the model. In chapter 3 the threshold limits for soil moisture, FPAR and snow cover and the threshold friction velocity used to calculate the surface emission were tuned

using Latin Hypercube Sampling (McKay et al. 1979). In addition to this, three sub cloud scavenging schemes were also tested.

The experiments were ranked using a skills score to determine the optimal match between the model output and multiple measurement datasets. The experiment with the highest skills score used threshold limits FPAR=0.37, soil moisture =7.79mm, snow depth =0.01m, with threshold friction velocities for each particle reduced by a factor of 0.55, combined with a size dependent removal scheme with rain droplet diameter 0.5mm.

The results showed changing the sub-cloud scavenging scheme had more of an impact on the model performance than changing the threshold parameters. The un-tuned model, which used the size independent sub cloud scavenging scheme, underestimated dust deposition to Greenland, the North Pacific and the North Atlantic, relative to other regions. This was improved by choosing the size dependent removal scheme with rain droplet diameter 0.5mm. Indeed, overall the best results were obtained for the size dependent removal scheme with rain droplet diameter 0.5mm. The worst results were found for the size independent sub cloud scavenging scheme.

Even after tuning the model, there still remained a large uncertainty in the estimates of the annual mean surface emissions. The estimates ranged from 1136 to 4654 $Mtyr^{-1}$ depending on the individual measurement dataset the model was compared to. The large uncertainty was caused by differences in datasets associated with different measurement techniques and the fact that the measurements were made over different time periods.

The third aim of this thesis was to evaluate how well the tuned LPJ-dust model reproduced seasonality in the dust cycle. In Chapter 4 the simulated total column dust loading was compared to TOMS aerosol index. The model was reasonably successful at predicting the seasonality in the total column dust loading over North Africa, Asia, South Africa, South America, and North America but not in Australia. In Australia the maximum surface emission occurred between August and December rather than as expected in DJF. The early onset of maximum emissions coincided with when LPJ incorrectly predicted the timing of the minimum vegetation cover.

A comparison between the simulated surface concentrations and measurements from the University of Miami aerosol network showed that the model did a reasonably good job at

predicting the magnitude of dust concentrations in the North Atlantic and at sites in the Pacific close to the Asian source. The model over predicted the surface concentrations at sites in the remote Pacific.

In all regions maximum emissions occurred when low precipitation combined with a high frequency of wind speed events greater than $2ms^{-1}$. In Patagonia, surface emissions were strongly anti-correlated with precipitation because wind speeds exceeded $2ms^{-1}$ continuously throughout the year. The seasonality in soil moisture over Patagonia affected the seasonality in the dust loading over the Southern Ocean. Vegetation cover was found to constrain dust emissions in North America, Central Asia, Eastern China and South Africa.

A comparison between the simulated surface concentrations and measurements from the University of Miami aerosol network showed that including the seasonality in FPAR improved estimates of the surface concentrations down wind of the Asian source region. Including seasonality in soil moisture improved estimates of the surface concentrations down wind of Asia, North African and Patagonia.

The fourth aim of this thesis was to use the LPJ-dust model to test whether the contraction and expansion of dust source regions explains observed trends in the atmospheric dust loading on decadal time scales. In Chapter 5 the LPJ-dust model was used to study two regions where vegetation cover is believed exert control over the extent of the source areas.

The first study tested if changes in vegetation cover in the Sahel could account for the four fold increase in dust concentrations measured at Barbados during the 1980s relative to the 1960s. The results showed that there was an expansion of the Sahara in 1984 relative to 1966 which resulted in a doubling of emissions from the Sahel. This was not enough to account for the high dust concentrations measured at Barbados during the 1980s relative to the 1960s. There was no substantial improvement in the model's ability to capture the high dust concentrations at Barbados during the 1980s when preferential dust sources, in the form of dried out lake beds, are included in the model.

The second study tested if changes in vegetation cover have contributed to the variability in springtime visibility in Northern China. Vegetation cover was not found to contribute to the variability in springtime visibility between 1983 and 2000. The variability was controlled by wind speeds. This contradicts the work of Zou and Zhai (2004) who showed

that vegetation cover in North China was anti-correlated with springtime dust storm frequencies.

6.2 Future Work

The use of a DGVM within the framework of a dust cycle model represents an advancement in the area of dust cycle modelling. However, the model developed in this thesis has limitations which could benefit from further work.

The results presented in chapter 4 showed that the LPJ-dust model was unable to simulate the seasonality in dust emissions from Australia because LPJ could not simulate the timing of minimum vegetation cover correctly. Future work could focus on improving the LPJ model. The current set of PFTs in LPJ may not be enough to represent all the vegetation types so these could be extended. In particular, LPJ does not include shrub PFTs which may be important in arid and semi-arid regions.

This development work would involve introducing new PFT into LPJ which have properties specific to shrubs. These properties would incorporate the fact that that new leaf growth occurs quickly after rainfall in shrubs (Mooney 1981). During periods of drought, the stomata reduce in size so that less water is lost by transpiration (Smith 1997). The rate of photosynthesis in shrubs remains high even during drought condition (Wilson 1998).

Shrub PFTs have already been introduced into the community Land Model–DGVM (CLM-DGVM) using theses types of PFT properties (Zeng et al. 2008). Including shrub PFTs into LPJ would provide a better prediction of vegetation cover in arid and semi-arid region. As a result this may improve the ability of the model to predict the seasonality in surface emissions from Australia.

Further LPJ development work could be carried out to improve the parameterisation of vegetation disturbance by fire. At present LPJ takes a very simplistic approach to fire. Fire is assumed to occur when sufficient fuel in the form of dry material is available. Ignition sources are assumed to be available whenever fire is possible. In reality ignition sources are not always available and are often sporadic. Ignition sources can occur from lighting strikes or by humans.

The version of LPJ used in this thesis does not contain vegetation disturbance by agriculture or land management. There is a version of LPJ currently available that includes managed lands and irrigation (Bondeau et al. 2007). This version uses a land use data set to identify different Crop Functional Types. Theses Crop Functional Types work in much the same way as PFT already in LPJ. An experiment could be carried out in which the managed land version of LPJ is used to calculate dust source areas. It would be interesting to investigate whether this improves estimates of surface concentrations at Barbados particularly during the 1980s.

Another area for future development is to include a better way of treating the surface roughness in the LPJ-dust model. The roughness length is used to modify the vertical wind profile and is related to the presence of vegetation cover or other non erodible obstacles on the surface. Because of the cubic relationship between the wind speed and the dust flux, the way in which the roughness length is treated may have a large impact on the surface emissions. The LPJ-dust model uses a fixed surface roughness of 0.001m which is typical of level desert (Seinfeld 1998). A remote sensing derived dataset such as that from the ESR backscattering radiometer could be used (Prigent et al. 2005). Alternatively, the roughness length could be parameterised as a function of the leaf area index and the stand height of the vegetation cover simulated by LPJ using an empirical relationship such as that by Lindroth (1993).

A further way to improve the LPJ-dust model is to include a parameterisation for sub-grid scale gustiness. One possible way to do this is to apply a probability distribution function to the wind speed data. A Weibull probability density function was used by Grini et al. (2005). Cakmur et al., (2006) parameterised sub-grid scale gustiness by constructing a probability distribution of wind speed within each grid box that depends upon the speed explicitly calculated by a GCM and the magnitude of fluctuations about this speed. Both these studies found an improvement in the estimates of the surface emission when gustiness was included.

Another improvement to the LPJ-dust model would be to include preferential dust source regions. It was found that representing preferential dust sources as paleo lake beds in the same way as Tegen et al., (2002) did very little to improve estimates of surface concentrations at Barbados. However, there are other ways to parameterise preferential source regions that could be used. Three different approaches to parameterisation were

tested by Zender et al., (2003b). The first approach was to relate the erodibility of the surface to topographic lows using a digital elevations map. The second way as to make the erodibility proportional to the number of grid cells upstream that flow into a grid box. The third way was to make the erodibility proportional to the surface run off where the surface run off was obtained from the NCAR Land Surface Model (Bonan 1996). This would account for dust regions that become more active after temporary hydrological activity or inundation. This is typical of what happen in clay pans such as in North Lake Eyre in Australia (McTainsh 1999). It was found all three parameterisations produced better agreement with station and satellite data, but the second scheme produced the best results. The three parameterisations could be tested in the LPJ-dust model as they only require a digital elevation map and surface run off data. The surface run off data is already simulated in LPJ. Experiments could be run to investigate if any of these parameterisations improve estimates of the surface emissions.

An additional area of further development could focus on improving the experimental design of the LPJ-dust model. Currently LPJ and the surface emission scheme is run on a 0.5 x 0.5 degree spatial resolution. The surface emissions are interpolated onto a T42 resolution for input into TOMCAT. This could be modified so that LPJ and the emission scheme are run on a T42 spatial resolution. If this does not affect the performance of the model, then running LPJ and the surface emission scheme on a T42 resolution would decrease the simulation time and remove the need to interpolate the emissions.

Future dust modelling studies would benefit from the availability of more measurement data. In particular there is a scarcity of global data that can be used to validate model estimates of dust sources. Remote sensing data such as TOMS AI has a temporal resolution of one day which means that dust will have been transported from the source region making it difficult to identify the origin. One solution is to take advantage of new remote sensing data that has a high temporal resolution. Schepanski et al., (2009) analysed 15 minute Meteosat Second Generation (MSG) Spinning Enhanced Visible and Infrared Imager (SEVIRI) infrared dust index images to identify dust source areas over North Africa on a 1^{o} x 1^{o} grid. This type of data could be used to identify the spatial distribution of dust emissions.

Furthermore, there is lack of long term measurements that span decades. This type of data is very valuable for understanding decadal scale changes in the dust loading. Although the

Barbados dust record has been useful to validate inter-annual variability in North African dust emissions, it is only representative of one point location. Visibility data has been used in the absence of other long term measurements to validate the LPJ-dust model in Northern China. This is type of data is semi-quantitative because it depends on the observer's ability to distinguish a large black object from the horizon.

The LPJ-dust model does not use any remote sensing input data; therefore, future work could also include the application of the LPJ-dust model to the past or future climate. It would be interesting to test if the model could reproduce the 2-25 increase in dust deposition rates at high latitudes that are observed in ice core records at the LGM (Lambert et al. 2008). The performance of the LPJ-dust model could be compared to other dust simulations for the LGM (Mahowald et al. 1999; Werner et al. 2002; Mahowald 2006).

The LPJ-dust model could be used to estimate the future atmospheric dust loading in a climate with elevated CO_2. Modelling studies have shown that if vegetation cover is allowed to respond to elevated CO_2 then dust emissions will decrease in the future (Mahowald and Luo 2003; Mahowald 2006; Mahowald 2007). Conditions of elevated CO_2 increases plant water use efficiently which enhances the ability of vegetation to survive under arid conditions. These studies have all used the BIOME4 model. Using the LPJ-dust model would make it possible to predict the year to year variability in dust emissions in response to changes in the future climate which was not possible using BIOME4.

This thesis has described the development and application of a new dust cycle model. There are many limitations to the new model and the potential for further model development. One of the major challenges faced is to incorporate anthropogenic dust sources into dust cycle models. Currently the IPCC estimates that dust direct radiative forcing ranges from -0.56 to $+0.1 Wms^{-2}$ (Forster 2007). This estimate assumes an anthropogenic contribution of 0% to 20%. The results of this work suggest that the anthropogenic contribution may be as high as 60%.

Appendix

Modifications made to TOMCAT source code to store the convection/diffusion matrix in memory.

```
*B,SLIMCAT.16
c     *** the convection matrix was written to fort.19 every 6 hours and
c     *** read back in every 1 hour. To improve the simulation time store
c     *** the variable in memory
c     *** These are the changes needed
c     ***common block to share CONVC between CONVMA and CONSOM
      REAL CONVC(LON,LAT,NIV,NIV)
      COMMON /CONVCC/ CONVC
*D,CONSOM.30
      REAL CONVC(LON,LAT,NIV,NIV)
      COMMON /CONVCC/ CONVC
*D,CONSOM.34
c     *** REMOVE REWIND CONV
*D,CONSOM.39
c     *** REMOVE READ CONVC
*D,CONSOM.56,59
      ZRXZM(I,L)=CONVC(I,J,L,L)*SXZ(I,J,L,JV)
      ZRYZM(I,L)=CONVC(I,J,L,L)*SYZ(I,J,L,JV)
      ZRZZM(I,L)=CONVC(I,J,L,L)*SZZ(I,J,L,JV)
      ZRZM (I,L)=CONVC(I,J,L,L)*SZ (I,J,L,JV)
*D,CONSOM.66,71
      ZRM  (I,L)=ZRM  (I,L)+CONVC(I,J,L,K)*S0 (I,J,K,JV)
      ZRXM (I,L)=ZRXM (I,L)+CONVC(I,J,L,K)*SX (I,J,K,JV)
      ZRYM (I,L)=ZRYM (I,L)+CONVC(I,J,L,K)*SY (I,J,K,JV)
      ZRXXM(I,L)=ZRXXM(I,L)+CONVC(I,J,L,K)*SXX(I,J,K,JV)
      ZRXYM(I,L)=ZRXYM(I,L)+CONVC(I,J,L,K)*SXY(I,J,K,JV)
      ZRYYM(I,L)=ZRYYM(I,L)+CONVC(I,J,L,K)*SYY(I,J,K,JV)
*D,CONSOM.105
      ZTOTM(I,L)=ZTOTM(I,L)+CONVC(I,J,L,K)*SM(I,J,K)
*D,DIFCON.39
C  common block to share CONVC between CONVMA and CONSOM
      REAL CONVC(LON,LAT,NIV,NIV)
      COMMON /CONVCC/ CONVC
*D,DIFCON.315
      CONVC(I,J,L,K)=G(L,K)
*D,DIFCON.321
c     *** REMOVE WRITE CONVC
```

		Tuneable parameters				Tuning Factor			
Expt ID	Removal Scheme	FPAR	Soil Moist	Snow	TFVSF	DIRTMAP	Ginoux	Miami	NRMSE
23	**Slinn droplet=0.5mm**	**0.37**	**7.79**	**0.10**	**0.55**	**2.70**	**4.10**	**1.00**	**1.20**
31	Slinn droplet=0.5mm	0.28	11.68	0.07	0.58	2.50	4.00	0.90	1.26
36	Slinn droplet=0.5mm	0.49	10.53	0.00	0.68	4.30	5.80	1.70	1.28
42	Slinn droplet=0.5mm	0.27	12.41	0.09	0.64	3.50	5.10	1.30	1.28
33	Slinn droplet=0.5mm	0.33	9.49	0.08	0.90	18.60	18.70	10.10	1.28
41	Slinn droplet=0.5mm	0.43	8.65	0.03	0.82	11.40	12.50	5.70	1.28
27	Slinn droplet=0.5mm	0.46	15.75	0.06	0.41	1.10	1.90	0.30	1.29
24	Slinn droplet=0.5mm	0.23	11.09	0.05	0.80	8.70	11.70	4.10	1.30
25	Slinn droplet=0.5mm	0.32	13.56	0.07	0.93	20.80	20.10	10.40	1.33
35	Slinn droplet=0.5mm	0.24	16.86	0.04	0.60	2.50	3.80	0.80	1.36
38	Slinn droplet=0.5mm	0.40	14.93	0.04	0.78	6.80	8.30	2.70	1.36
39	Slinn droplet=0.5mm	0.41	17.04	0.08	0.96	24.60	20.90	11.00	1.40
28	Slinn droplet=0.5mm	0.36	18.47	0.05	0.71	4.30	5.30	1.50	1.41
29	Slinn droplet=0.5mm	0.30	18.82	0.02	0.99	33.30	26.20	14.50	1.42
26	Slinn droplet=0.5mm	0.21	21.50	0.02	0.46	1.40	2.10	0.30	1.43
37	Slinn droplet=0.5mm	0.35	19.92	0.01	0.66	3.10	4.00	0.90	1.44
22	Slinn droplet=0.5mm	0.50	20.00	0.01	0.66	3.10	3.90	0.90	1.44
32	Slinn droplet=0.5mm	0.47	24.18	0.06	0.51	1.50	2.10	0.30	1.49
40	Slinn droplet=0.5mm	0.44	21.24	0.09	0.87	11.50	11.30	3.80	1.50
30	Slinn droplet=0.5mm	0.39	22.99	0.01	0.46	1.20	1.80	0.30	1.50
34	Slinn droplet=0.5mm	0.25	23.88	0.03	0.73	4.90	6.10	1.30	1.53
55	Slinn droplet=2mm	0.25	23.88	0.03	0.73	3.90	6.10	0.20	1.60
56	Slinn droplet=2mm	0.24	16.86	0.04	0.60	1.80	3.70	0.10	1.60
49	Slinn droplet=2mm	0.36	18.47	0.05	0.71	3.30	5.20	0.20	1.63
50	Slinn droplet=2mm	0.30	18.82	0.02	0.99	29.50	26.00	1.90	1.65
45	Slinn droplet=2mm	0.23	11.09	0.05	0.80	6.50	11.60	0.60	1.66
43	Slinn droplet=2mm	0.50	20.00	0.01	0.66	2.40	3.80	0.10	1.66
61	Slinn droplet=2mm	0.44	21.24	0.09	0.87	9.70	11.20	0.50	1.66
59	Slinn droplet=2mm	0.40	14.93	0.04	0.78	5.30	8.20	0.30	1.67
52	Slinn droplet=2mm	0.28	11.68	0.07	0.58	1.70	4.00	0.10	1.67
58	Slinn droplet=2mm	0.35	19.92	0.01	0.66	2.40	4.00	0.10	1.68
46	Slinn droplet=2mm	0.32	13.56	0.07	0.93	17.50	19.90	1.20	1.68
63	Slinn droplet=2mm	0.27	12.41	0.09	0.64	2.40	5.10	0.20	1.68
60	Slinn droplet=2mm	0.41	17.04	0.08	0.96	21.40	20.80	1.20	1.69
2	Brandt fixed	0.37	7.79	0.10	0.55	1.50	4.00	0.60	1.69
54	Slinn droplet=2mm	0.33	9.49	0.08	0.90	14.50	18.50	1.20	1.71
57	Slinn droplet=2mm	0.49	10.53	0.00	0.68	2.90	5.70	0.20	1.71
62	Slinn droplet=2mm	0.43	8.65	0.03	0.82	8.40	12.40	0.70	1.73
44	Slinn droplet=2mm	0.37	7.79	0.10	0.55	1.60	4.00	0.10	1.73
15	Brandt fixed	0.49	10.53	0.00	0.68	2.90	5.70	0.90	1.73
10	Brandt fixed	0.28	11.68	0.07	0.58	1.70	4.00	0.50	1.74
21	Brandt fixed	0.27	12.41	0.09	0.64	2.30	5.10	0.60	1.74
20	Brandt fixed	0.43	8.65	0.03	0.82	8.30	12.40	3.30	1.75
12	Brandt fixed	0.33	9.49	0.08	0.90	14.30	18.60	5.90	1.76
14	Brandt fixed	0.24	16.86	0.04	0.60	1.70	3.70	0.30	1.76
3	Brandt fixed	0.23	11.09	0.05	0.80	6.40	11.60	2.20	1.77
1	**Brandt fixed**	**0.50**	**20.00**	**0.01**	**0.66**	**2.30**	**3.80**	**0.40**	**1.77**
16	Brandt fixed	0.35	19.92	0.01	0.66	2.30	4.00	0.40	1.77
17	Brandt fixed	0.40	14.93	0.04	0.78	5.20	8.20	1.30	1.77
6	Brandt fixed	0.46	15.75	0.06	0.41	0.70	1.80	0.10	1.78
7	Brandt fixed	0.36	18.47	0.05	0.71	3.30	5.30	0.70	1.78
4	Brandt fixed	0.32	13.56	0.07	0.93	17.10	20.00	5.50	1.78
18	Brandt fixed	0.41	17.04	0.08	0.96	21.00	20.90	5.80	1.79
8	Brandt fixed	0.30	18.82	0.02	0.99	28.90	26.10	8.00	1.79
19	Brandt fixed	0.44	21.24	0.09	0.87	9.50	11.30	2.00	1.80

9	Brandt fixed	0.39	22.99	0.01	0.46	0.90	1.80	0.10	1.80
13	Brandt fixed	0.25	23.88	0.03	0.73	3.80	6.10	0.60	1.80
5	Brandt fixed	0.21	21.50	0.02	0.46	0.90	2.10	0.10	1.81
11	Brandt fixed	0.47	24.18	0.06	0.51	1.10	2.10	0.10	1.83
47	Slinn droplet=2mm	0.21	21.50	0.02	0.46	0.90	2.10	0.10	2.16
53	Slinn droplet=2mm	0.47	24.18	0.06	0.51	1.10	2.10	0.10	2.30
51	Slinn droplet=2mm	0.39	22.99	0.01	0.46	0.90	1.80	0.10	2.76
48	Slinn droplet=2mm	0.46	15.75	0.06	0.41	0.70	1.80	0.10	3.27

Table A. Tuning experiments ranked according to their total normalised root mean square error. The global tuning factors for each target dataset are listed. The best experiment is highlighted in blue and the un-tuned experiment in red.

Bibliography

Andersen, K. K., A. Armengaud, et al. (1998). "Atmospheric dust under glacial and interglacial conditions." Geophysical Research Letters **25**(13): 2281-2284.

Andersen, K. K. and C. Genthon (1996). "Modeling the present and last glacial maximum transportation of dust to the arctic with an extended source scheme." Impact of Desert Dust across the Mediterranean **11**: 123-132.

Annan, J. D., D. J. Lunt, et al. (2005). "Parameter estimation in an atmospheric GCM using the Ensemble Kalman Filter." Nonlinear Processes in Geophysics **12**(3): 363-371.

Bagnold, R. A. (1941). The physics of blown sand and desert dunes New York, Methuen.

Bonan, G. B. (1996). A land surface model (LSM version 1.0) for ecological, hydrological, and atmospheric studies: Technical description and user's guide. Boulder, Colo, NCAR,Natl. Cent. for Atmos. Res.

Bondeau, A., P. C. Smith, et al. (2007). "Modelling the role of agriculture for the 20th century global terrestrial carbon balance." Global Change Biology **13**(3): 679-706.

Boyd, P. W., A. J. Watson, et al. (2000). "A mesoscale phytoplankton bloom in the polar Southern Ocean stimulated by iron fertilization." Nature **407**(6805): 695-702.

Brandt, J., J. H. Christensen, et al. (2002). "Modelling transport and deposition of caesium and iodine from the Chernobyl accident using the DREAM model." Atmospheric Chemistry and Physics **2**: 397-417.

Braswell, B. H., D. S. Schimel, et al. (1997). "The response of global terrestrial ecosystems to interannual temperature variability." Science **278**(5339): 870-872.

Brovkin, V., A. Ganopolski, et al. (1997). "A continuous climate-vegetation classification for use in climate-biosphere studies." Ecological Modelling **101**(2-3): 251-261.

Buat-Menard, D. P. (1986). "Precipitation scavenging of aerosol particles over remote marine regions." Nature **321**: 508-510.

Buesseler, K. O., J. E. Andrews, et al. (2004). "The Effects of Iron Fertilization on Carbon Sequestration in the Southern Ocean." Science **304**(5669): 414-417.

Cakmur, R. V., R. L. Miller, et al. (2006). "Constraining the magnitude of the global dust cycle by minimizing the difference between a model and observations." Journal of Geophysical Research-Atmospheres **111**(D6).

Chiapello, I. and C. Moulin (2002). "TOMS and METEOSAT satellite records of the variability of Saharan dust transport over the Atlantic during the last two decades (1979-1997)." Geophysical Research Letters **29**(8).

Chiapello, I., C. Moulin, et al. (2005). "Understanding the long-term variability of African dust transport across the Atlantic as recorded in both Barbados surface concentrations and large-scale Total Ozone Mapping Spectrometer (TOMS) optical thickness." Journal of Geophysical Research-Atmospheres **110**(D18).

Coale, K. H., K. S. Johnson, et al. (2004). "Southern ocean iron enrichment experiment: Carbon cycling in high- and low-Si waters." Science **304**(5669): 408-414.

Coe, M. T. (1998). "A linked global model of terrestrial hydrologic processes: Simulation of modern rivers, lakes and wetlands. ." Journal of Geophysical Research **103**: 8885-8899.

Coe, M. T. and J. A. Foley (2001). "Human and natural impacts on the water resources of the Lake Chad basin." Journal of Geophysical Research-Atmospheres **106**(D4): 3349-3356.

Cox, P. (2001). Description of the 'TRIFFID' Dynamic Global Vegetation model. Technical Notes. **The Hadley Centre Met Office**.

Dayan, U., B. Ziv, et al. (2008). "Suspended dust over southeastern Mediterranean and its relation to atmospheric circulations." International Journal of Climatology **28**(7): 915-924.

Derbyshire, E., Meng, X.M., Dijkstra, T.A. (2000). Landslides in the Thick Loess Terrain of Northwest China. Chichester and New York, Wiley

Dubovik, O. and M. D. King (2000). "A flexible inversion algorithm for retrieval of aerosol optical properties from Sun and sky radiance measurements." Journal of Geophysical Research-Atmospheres **105**(D16): 20673-20696.

Evan, A. T., A. K. Heidinger, et al. (2006). "Analysis of winter dust activity off the coast of West Africa using a new 24-year over-water advanced very high resolution radiometer satellite dust climatology." Journal of Geophysical Research-Atmospheres **111**(D12).

Fecan, F., B. Marticorena, et al. (1999). "Parametrization of the increase of the aeolian erosion threshold wind friction velocity due to soil moisture for arid and semi-arid areas." Annales Geophysicae-Atmospheres Hydrospheres and Space Sciences **17**(1): 149-157.

Foley, J. A., I. C. Prentice, et al. (1996). "An Integrated Biosphere Model of Land Surface Processes, Terrestrial Carbon Balance, and Vegetation Dynamics." Global Biogeochem. Cycles **10**.

Forster, P., V. Ramaswamy, P. Artaxo, T. Berntsen, R. Betts, D.W. Fahey, J. Haywood, J. Lean, D.C. Lowe, G. Myhre, J. Nganga, R. Prinn,G. Raga, M. Schulz and R. Van Dorland (2007). Changes in Atmospheric Constituents and in Radiative Forcing. In: Climate Change 2007:The Physical Science Basis. Cambridge and New York, NY, USA, Cambridge University Press.

Friend, A. D., A. K. Stevens, et al. (1997). "A process-based, terrestrial biosphere model of ecosystem dynamics (Hybrid v3.0)." Ecological Modelling **95**(2-3): 249-287.

Gaiero, D. M., J. L. Probst, et al. (2003). "Iron and other transition metals in Patagonian riverborne and windborne materials: geochemical control and transport to the southern South Atlantic Ocean." Geochimica et Cosmochimica Acta **67**(19): 3603-3623.

Genthon, C. (1992). "Simulations of Desert Dust and Sea-Salt Aerosols in Antarctica with a General-Circulation Model of the Atmosphere." Tellus Series B-Chemical and Physical Meteorology **44**(4): 371-389.

Gillette, D. A. (1977). "Fine Particulate-Emissions Due to Wind Erosion." Transactions of the Asae **20**(5): 890-897.

Gillette, D. A. and R. Passi (1988). "Modeling Dust Emission Caused by Wind Erosion." Journal of Geophysical Research-Atmospheres **93**(D11): 14233-14242.

Ginoux, P., M. Chin, et al. (2001). "Sources and distributions of dust aerosols simulated with the GOCART model." Journal of Geophysical Research-Atmospheres **106**(D17): 20255-20273.

Ginoux, P., J. M. Prospero, et al. (2004). "Long-term simulation of global dust distribution with the GOCART model: correlation with North Atlantic Oscillation." Environmental Modelling & Software **19**(2): 113-128.

Goudie, A. S. and N. J. Middleton (1992). "The Changing Frequency of Dust Storms through Time." Climatic Change **20**(3): 197-225.

Goudie, N. M. a. A. (2006). Desert dust in the global system
Springer; illustrated edition edition.

Grini, A., G. Myhre, et al. (2005). "Model simulations of dust sources and transport in the global atmosphere: Effects of soil erodibility and wind speed variability." Journal of Geophysical Research **110**(D02205): 999999.

Grove, A. T. (1996). African river discharges and lake levels in the twentith century Newark, N. J. , Gordon and Breach.
Guo, G. and G. Xie (2008). "Technical note: Dust storms in China decreased during the last 50 years." International Journal of Remote Sensing **29**(6): 1619-1620.
Han, Y., X. Dai, et al. (2008). "Dust aerosols: A possible accelerant for an increasingly arid climate in North China." Journal of Arid Environments **72**(8): 1476-1489.
Hao, W. M. and M. H. Liu (1994). "Spatial and Temporal Distribution of Tropical Biomass Burning." Global Biogeochemical Cycles **8**(4): 495-503.
Hara, Y., I. Uno, et al. (2006). "Long-term variation of Asian dust and related climate factors." Atmospheric Environment **40**(35): 6730-6740.
Haxeltine, A. and I. C. Prentice (1996). "BIOME3: An equilibrium terrestrial biosphere model based on ecophysiological constraints, resource availability, and competition among plant functional types." Global Biogeochemical Cycles **10**(4): 693-709.
Haxeltine, A. and I. C. Prentice (1996). "A general model for the light-use efficiency of primary production." Functional Ecology **10**(5): 551-561.
Haywood, J., P. Francis, et al. (2003). "Radiative properties and direct radiative effect of Saharan dust measured by the C-130 aircraft during SHADE: 1. Solar spectrum." Journal of Geophysical Research-Atmospheres **108**(D18).
Herman, J. R., P. K. Bhartia, et al. (1997). "Global distribution of UV-absorbing aerosols from Nimbus 7/TOMS data." Journal of Geophysical Research-Atmospheres **102**(D14): 16911-16922.
Herut, B., M. D. Krom, et al. (1999). "Atmospheric input of nitrogen and phosphorus to the Southeast Mediterranean: Sources, fluxes, and possible impact." Limnology and Oceanography **44**(7): 1683-1692.
Hurrell, J. W. (1995). "Decadal Trends in the North-Atlantic Oscillation - Regional Temperatures and Precipitation." Science **269**(5224): 676-679.
Iversen, J. D., J. B. Pollack, et al. (1976). "Saltation Threshold on Mars - Effect of Interparticle Force, Surface-Roughness, and Low Atmospheric Density." Icarus **29**(3): 381-393.
Iversen, J. D. and B. R. White (1982). "Saltation Threshold on Earth, Mars and Venus." Sedimentology **29**(1): 111-119.
James, P. A. A. a. M. E. (1995). The NOAA/NASA Pathfinder AVHRR Land Data Set User's Manual Greenbelt, MD, Goddard Distributed Active Archive Center, NASA, Goddard Space Flight Center.
Jickells, T. D., Z. S. An, et al. (2005). "Global Iron Connections Between Desert Dust, Ocean Biogeochemistry, and Climate." Science **308**(5718): 67-71.
Joos, F., S. Gerber, et al. (2004). "Transient simulations of Holocene atmospheric carbon dioxide and terrestrial carbon since the Last Glacial Maximum." Global Biogeochemical Cycles **18**(2).
Joussaume, S. (1990). "Three-Dimensional Simulations of the Atmospheric Cycle of Desert Dust Particles Using a General Circulation Model " Journal of Geophysical Research **95**: 1909-1941.
Kaufman, Y. J., I. Koren, et al. (2005). "Dust transport and deposition observed from the Terra-Moderate Resolution Imaging Spectroradiometer (MODIS) spacecraft over the Atlantic ocean." Journal of Geophysical Research-Atmospheres **110**(D10).
Kim, J. (2008). "Transport routes and source regions of Asian dust observed in Korea during the past 40 years (1965-2004)." Atmospheric Environment **42**(19): 4778-4789.
Knorr, W. and M. Heimann (1995). "Impact of drought stress and other factors on seasonal land biosphere CO2 exchange studied through an atmospheric tracer transport model." Tellus B **47**(4): 471-489.

Kohfeld, K. E. and S. P. Harrison (2001). "DIRTMAP: The geological record of dust." Earth Science Review **54**: 81-114.
Koren, I., Y. J. Kaufman, et al. (2006). "The Bodele depression: a single spot in the Sahara that provides most of the mineral dust to the Amazon forest." Environmental Research Letters **1**(1).
Krinner, G., N. Viovy, et al. (2005). "A dynamic global vegetation model for studies of the coupled atmosphere-biosphere system." Global Biogeochemical Cycles **19**(1).
Lambert, F., B. Delmonte, et al. (2008). "Dust-climate couplings over the past 800,000 years from the EPICA Dome C ice core." Nature **452**(7187): 616-619.
Liang, X. (1996). "Description of a nine-level grid point atmospheric general circulation model." Advances in Atmospheric Sciences **13**(3).
Littmann, T. (1991). "Dust Storm Frequency in Asia - Climatic Control and Variability." International Journal of Climatology **11**(4): 393-412.
Lu, J. T., X. K. Zou, et al. (2003). "Analyses of the causes for frequent dust weather that occurred in China during the last three years." Clim. Environ. Res **8**(1): 107-113.
Lunt, D. J. and P. J. Valdes (2002). "The modern dust cycle: Comparison of model results with observations and study of sensitivities." Journal of Geophysical Research-Atmospheres **107**(D23).
Luo, C., N. M. Mahowald, et al. (2003). "Sensitivity study of meteorological parameters on mineral aerosol mobilization, transport, and distribution." Journal of Geophysical Research-Atmospheres **108**(D15).
Mahowald, N., K. Kohfeld, et al. (1999). "Dust sources and deposition during the last glacial maximum and current climate: A comparison of model results with paleodata from ice cores and marine sediments." Journal of Geophysical Research-Atmospheres **104**(D13): 15895-15916.
Mahowald, N., K. Kohfeld, et al. (1999). "Dust sources and deposition during the last glacial maximum and current climate: A comparison of model results with paleodata from ice cores and marine sediments." Journal of Geophysical Research **104**(D13): 15,895-15,916.
Mahowald, N., C. Luo, et al. (2003). "Interannual variability in atmospheric mineral aerosols from a 22-year model simulation and observational data." Journal of Geophysical Research-Atmospheres **108**(D12).
Mahowald, N. M. (2006). "Change in atmospheric mineral aerosols in response to climate: Last glacial period, preindustrial, modern, and doubled carbon dioxide climates." Journal of geophysical research **111**(D10): D10202.
Mahowald, N. M. (2007). "Anthropocene changes in desert area: Sensitivity to climate model predictions." Geophysical Research Letters **34**(18).
Mahowald, N. M. (2007). "Anthropocene changes in desert area: Sensitivity to climate model predictions." Geophysical Research Letters **34**.
Mahowald, N. M., J. A. Ballantine, et al. (2007). "Global trends in visibility: implications for dust sources." Atmospheric Chemistry and Physics **7**(12): 3309-3339.
Mahowald, N. M. and C. Luo (2003). "A less dusty future?" Geophysical Research Letters **30**(17).
Mahowald, N. M., C. S. Zender, et al. (2002). "Understanding the 30-year Barbados desert dust record." Journal of Geophysical Research-Atmospheres **107**(D21).
Marticorena, B. and G. Bergametti (1995). "Modeling the Atmospheric Dust Cycle .1. Design of a Soil-Derived Dust Emission Scheme." Journal of Geophysical Research-Atmospheres **100**(D8): 16415-16430.
Marticorena, B., G. Bergametti, et al. (1997). "Modeling the atmospheric dust cycle .2. Simulation of Saharan dust sources." Journal of Geophysical Research-Atmospheres **102**(D4): 4387-4404.

Martin, J. H. (1990). "Glacial-interglacial CO2 change: The iron hypothesis." Paleoceanography **5**: 1-13.
Matthews, E. (1983). "New high-resulation data sets for clmate studies." Journal of Applied Meteorlogy **22**: 474-487.
McKay, M. D., R. J. Beckman, et al. (1979). "A Comparison of Three Methods for Selecting Values of Input Variables in the Analysis of Output from a Computer Code." Technometrics **21**(2): 239-245.
McTainsh, G. H. and J. R. Pitblado (1987). "Dust Storms and Related Phenomena Measured from Meteorological Records in Australia." Earth Surface Processes and Landforms **12**(4): 415-424.
McTainsh, G. H. M., J.F. Leys and W.G. Nickling, (1999). "Wind erodibility of arid lands in the channel country of western Queensland, Australia,." **Zeitschrift fur Geomorphologie N.F, Supplementband**(116): 113–130.
Menendez, I., J. L. Diaz-Hernandez, et al. (2007). "Airborne dust accumulation and soil development in the North-East sector of Gran Canaria (Canary Islands, Spain)." Journal of Arid Environments **71**(1): 57-81.
Meskhidze, N., W. L. Chameides, et al. (2005). "Dust and pollution: A recipe for enhanced ocean fertilization?" Journal of Geophysical Research-Atmospheres **110**(D3).
Meskhidze, N., A. Nenes, et al. (2007). "Atlantic Southern Ocean productivity: Fertilization from above or below?" Global Biogeochemical Cycles **21**(2).
Middleton, N. J. (1986). "A Geography of Dust Storms in Southwest Asia." Journal of Climatology **6**(2): 183-196.
Miller, R. L., I. Tegen, et al. (2004). "Surface radiative forcing by soil dust aerosols and the hydrologic cycle." Journal of Geophysical Research-Atmospheres **109**(D4).
Mooney, H. A. (1981). Primary production in Mediterranean-climate regions, in Mediterranean-Type Shrublands. Amsterdam, Elsevier Sci.
Moulin, C., C. E. Lambert, et al. (1997). "Control of atmospheric export of dust from North Africa by the North Atlantic oscillation." Nature **387**(6634): 691-694.
N'tchayi Mbourou, J. J. B. a. S. E. N., T (1997). "he diurnal and seasonal cycles of wind-borne dust over Africa north of the equator." Journal of Applied Meteorology **36**(7): 868-882.
Nicholson, S. E. (1993). "An Overview of African Rainfall Fluctuations of the Last Decade." Journal of Climate **6**(7): 1463-1466.
Orgill, M. M. and G. A. Sehmel (1976). "Frequency and diurnal variation of dust storms in the contiguous U.S.A." Atmospheric Environment (1967) **10**(10): 813-825.
Patterson, E. M. and D. A. Gillette (1977). "Measurements of visibility vs mass-concentration for airborne soil particles." Atmospheric Environment (1967) **11**(2): 193-196.
Petoukhov, V., A. Ganopolski, et al. (2000). "CLIMBER-2: a climate system model of intermediate complexity. Part I: model description and performance for present climate." Climate Dynamics **16**(1): 1-17.
Price, A. R., G. Xue, et al. (2007). "Optimization of integrated Earth System Model components using Grid-enabled data management and computation." Concurrency and Computation-Practice & Experience **19**(2): 153-165.
Prigent, C., I. Tegen, et al. (2005). "Estimation of the aerodynamic roughness length in arid and semi-arid regions over the globe with the ERS scatterometer." Journal of Geophysical Research-Atmospheres **110**(D9).
Prospero, J. M., P. Ginoux, et al. (2002). "Environmental characterization of global sources of atmospheric soil dust identified with the Nimbus 7 Total Ozone Mapping Spectrometer (TOMS) absorbing aerosol product." Reviews of Geophysics **40**(1).
Prospero, J. M. and P. J. Lamb (2003). "African Droughts and Dust Transport to the Caribbean: Climate Change Implications." Science **302**(5647): 1024-1027.

Prospero, J. M. and R. T. Nees (1986). "Impact of the North African drought and El Nino on mineral dust in the Barbados trade winds." Nature **320**(6064): 735-738.
Pruppacher, H. R., P. Hobbs and A. Deepak (1981). Microstructure of Atmospheric Clouds and Precipitation,
in Clouds: Their Formation, Optical Properties and Effects.
Pye, K. (1987). Aeolian Dust and Dust Deposits. . London, Academic Press Inc. .
Qian, W. H., L. S. Quan, et al. (2002). "Variations of the dust storm in China and its climatic control." Journal of Climate **15**(10): 1216-1229.
Redelsperger, J. L., F. Guichard, et al. (2000). "A parameterization of mesoscale enhancement of surface fluxes for large-scale models (vol 13, pg 402, 2000)." Journal of Climate **13**(13): 2404-2404.
Seinfeld, S. N. P. a. J. H. (1998). Atmospheric Chemistry and Physics, from air polution to climate change. New York, Wiley.
Shao, Y. and M. R. Raupach (1993). "Effect of Saltation Bombardment on the Entrainment of Dust by Wind." Journal of Geophysical Research-Atmospheres **98**(D7): 12719-12726.
Sitch, S., B. Smith, et al. (2003). "Evaluation of ecosystem dynamics, plant geography and terrestrial carbon cycling in the LPJ dynamic global vegetation model." Global Change Biology **9**: 161-185.
Slinn, W. G. N. (1983). Precipitation scavenging. In: Atmospheric Sciences and Power Production-1979
Washington, DC, U.S. Department of Energy**:** Chapter 11.
Smith, S. D., R. K. Monson, and J. E. Anderson (1997). Physiological Ecology of North American Desert Plants,. Berlin, Springer.
Soderberg, K. and J. S. Compton (2007). "Dust as a nutrient source for fynbos ecosystems, South Africa." Ecosystems **10**(4): 550-561.
Stockwell, D. Z. and M. P. Chipperfield (1999). "A tropospheric chemical-transport model: Development and validation of the model transport schemes." Quarterly Journal of the Royal Meteorological Society **125**(557): 1747-1783.
Swap, R., M. Garstang, et al. (1992). "Saharan Dust in the Amazon Basin." Tellus Series B-Chemical and Physical Meteorology **44**(2): 133-149.
Tanaka, T. Y. and M. Chiba (2006). "A numerical study of the contributions of dust source regions to the global dust budget." Global and Planetary Change **52**(1-4): 88-104.
Tegen, I. and I. Fung (1994). "Modeling of Mineral Dust in the Atmosphere - Sources, Transport, and Optical-Thickness." Journal of Geophysical Research-Atmospheres **99**(D11): 22897-22914.
Tegen, I. and I. Fung (1995). "Contribution to the Atmospheric Mineral Aerosol Load from Land-Surface Modification." Journal of Geophysical Research-Atmospheres **100**(D9): 18707-18726.
Tegen, I., S. P. Harrison, et al. (2002). "Impact of vegetation and preferential source areas on global dust aerosol: Results from a model study." Journal of Geophysical Research-Atmospheres **107**(D21).
Tegen, I. and R. Miller (1998). "A general circulation model study on the interannual variability of soil dust aerosol." Journal of Geophysical Research-Atmospheres **103**(D20): 25975-25995.
Toon, O. B. (2003). "Atmospheric science: African dust in Florida clouds." Nature **424**(6949): 623-624.
Trenberth, K. E. and J. G. Olson (1988). "An Evaluation and Intercomparison of Global Analyses from the National-Meteorological-Center and the European-Centre-for-Medium-Range-Weather-Forecasts." Bulletin of the American Meteorological Society **69**(9): 1047-1057.

Tsuda, A., S. Takeda, et al. (2003). "A Mesoscale Iron Enrichment in the Western Subarctic Pacific Induces a Large Centric Diatom Bloom." Science **300**(5621): 958-961.
Tucker, C. J., H. E. Dregne, et al. (1991). "Expansion and Contraction of the Sahara Desert from 1980 to 1990." Science **253**(5017): 299-301.
Tucker, C. J. and S. E. Nicholson (1999). "Variations in the size of the Sahara Desert from 1980 to 1997." Ambio **28**(7): 587-591.
Twomey, S. (1974). "Pollution and Planetary Albedo." Atmospheric Environment **8**(12): 1251-1256.
Wang, W. (2006). "Numerical simulation and synoptic analysis of dust emission and transport in East Asia." Global and planetary change **52**(1-4): 57-70.
Wang, X. M., Z. B. Dong, et al. (2004). "Modern dust storms in China: an overview." Journal of Arid Environments **58**(4): 559-574.
Wang, X. M., Z. J. Zhou, et al. (2006). "Control of dust emissions by geomorphic conditions, wind environments and land use in northern China: An examination based on dust storm frequency from 1960 to 2003." Geomorphology **81**(3-4): 292-308.
Werner, M., I. Tegen, et al. (2002). "Seasonal and interannual variability of the mineral dust cycle under present and glacial climate conditions." Journal of Geophysical Research-Atmospheres **107**(D24).
Wilson, S. D. (1998). Competition between grasses and woody plants. New York, Cambridge Univ. Press.
Woodruff, W. S. C. a. N. P. (1957). "Sedimentary characteristics of dust storms—II. Visibility and dust concentration,." Atmospheric Journal of Science **255**: 104-114.
Woodward, F. I., M.R. Lomas and R.A. Betts (1998). "Vegetation-climate feedbacks in a greenhouse world." Phil. Trans. R. Soc. Lond. Ser. B. Biol. Sci **353**: 29-38.
Yue, X., H. J. Wang, et al. (2009). "Simulation of dust aerosol radiative feedback using the Global Transport Model of Dust: 1. Dust cycle and validation." Journal of Geophysical Research-Atmospheres **114**.
Zender, C. S., H. Bian, et al. (2003a). "Mineral Dust Entrainment and Deposition (DEAD) model: Description and 1990s dust climatology." Journal of Geophysical Research **108**(D14): 4416.
Zender, C. S., D. Newman, et al. (2003b). "Spatial heterogeneity in aeolian erodibility: Uniform, topographic, geomorphic, and hydrologic hypotheses." Journal of Geophysical Research-Atmospheres **108**(D17).
Zeng, X., X. Zeng, et al. (2008). "Growing temperate shrubs over arid and semiarid regions in the Community Land Modelâ€“Dynamic Global Vegetation Model." Global Biogeochem. Cycles **22**.
Zhao, C. S. (2004). "Relationship between climatic factors and dust storm frequency in Inner Mongolia of China." Geophysical research letters **31**(1): L01103.
Zobler, L. (1986). A world soil file for global climate modeling. Tech. Rep. NASA. Washington D.C., NASA**:** 32.
Zou, X. K. and P. M. Zhai (2004). "Relationship between vegetation coverage and spring dust storms over northern China." J. Geophys. Res. **109**.